2021

# Development of Nano-engineered Perovskite-based Thermoelectric Material for Waste Heat Recovery

Al Jumlat Ahmed
*University of Wollongong*

UNIVERSITY OF WOLLONGONG AUSTRALIA

# Development of Nano-engineered Perovskite-based Thermoelectric Material for Waste Heat Recovery

Al Jumlat Ahmed

Supervisors:

Distinguished Professor Xiaolin Wang

Professor Yusuke Yamauchi

Dr MD Shahriar A Hossain

This thesis is presented as part of the requirement for the conferral of the degree:

Doctor of Philosophy

University of Wollongong

Institute for Superconducting and Electronic Materials (ISEM)

February 2021

# Abstract

The enormous amount of waste heat from different sources for instance: exhaust system of automobiles, industrial boilers and chimneys, thermal power plants and household cooking stove, can be directly converted into useful electrical energy by thermoelectric generator (TEG). Hence, thermoelectric (TE) has a huge potential to be a simple and environment-friendly technology for direct conversion of waste heat into usable electricity. However, the energy conversion efficiency and lifetime of thermoelectric devices are not adequate for commercial usages. Energy scientists around the globe are working on different thermoelectric materials and device configurations to overcome these hurdles.

Conventional thermoelectric materials such as $Bi_2Te_3$, PbTe, and $Cu_2Se$ exhibit high thermoelectric performance, however these materials have some shortcomings like poor durability, low operating temperature, limited availability, and high toxicity. On the other hand, metal oxide based thermoelectric materials are highly durable at high temperatures, non-toxic, low-cost, and have minimal environmental impact. However, the performance of metal oxide based thermoelectric materials are still inferior compared to the conventional thermoelectric materials due to their high lattice thermal conductivity.

$SrTiO_3$ and $BaTiO_3$ are intrinsically insulator, however their electrical conductivity can be easily improved by doping. In this study, electron doping in these materials was optimized by adding La in different atomic percentage and they were become *n*-type semiconducting material. Nanoscale pores were introduced into the bulk samples for further improvement of thermoelectric performance of $Sr_{1-x}La_xTiO_3$ and $Ba_{1-x}La_xTiO_3$. Powder samples with nanoscale pores were synthesized using the polymeric micelles self-assembly method. The commercially

available Pluronic F127 surfactant was used as soft template for nano scale pores formation. Then the powder samples were rapidly solidified using the spark plasma sintering (SPS) technique to prepare bulk samples with nanostructured pores. The sintering conditions such as sintering temperature, pressure, holding time, heating and cooling rate were optimized to fabricate highly dense nano crystalline bulk samples.

The X-ray diffraction (XRD) peaks shifting and reduction in lattice parameter confirmed that A site of $ABO_3$ crystal system of $SrTiO_3$ and $BaTiO_3$ were substituted by La atoms. Atomic resolution scanning transmission electron microscopy (STEM) images and energy dispersive X-ray spectrometry (EDS) results also showed that La was doped successfully into the lattice. The electrical conductivity of metal oxide materials was improved due to La doping and their showed *n*-type semiconducting behaviour.

The Brunauer–Emmett–Teller (BET) analysis, scanning electron microscopy images and transmission electron microscopy (TEM) images revealed that the samples synthesized using the surfactant F127 have nanostructured pores. There was a large reduction in the lattice thermal conductivity in the F127-treated samples arises primarily from the nanoscale pores distribution which introduces anisotropic phonon scattering within the unique nanoarchitecture. It was also observed that the nanoscale pores in the samples significantly improved the Seebeck coefficient (thermopower). The change in phonon charge-carrier interaction and charge-carrier mobility may be responsible for improvement in the thermopower due to nano pores. Therefore, there was remarkable enhancement in the power factor and the figure of merit ($zT$) of La doped $SrTiO_3$ and $BaTiO_3$ samples with nanoscale pores.

# Acknowledgments

Being a believer in creator, before everything I would like to express my sincere gratitude to the almighty, Allah. I am grateful for enlighten me with knowledge and for giving me strength to complete my PhD journey.

I would like to express my sincere gratitude to my respected supervisors, Distinguished Professor Xiaolin Wang, Professor Yusuke Yamauchi and Dr MD Shahriar Hossain for their valuable suggestions, continuous support, and guidance during my doctoral study herein the Institute for Superconducting and Electronic Materials (ISEM) at the University of Wollongong (UOW), Australia.

My PhD study is funded by the prestigious Endeavour Leadership Program of Australian Government. My sincere thanks to the Department of Education and Training, Australian Government for providing me such an opportunity.

I am thankful to all my colleagues and to the staff of ISEM. I would like to mention some names: Dr David L. Cortie, Dr Frank Fei, Dr Sheik Mohammad Kazi Nazrul Islam, Mr. Guangsai Yang and Mr. Yaser Rahman for their special assistance. I also acknowledge contribution of Dr David R. G. Mitchell, Mr. Tony Romeo, and Mr. Qiang Zhu from the UOW Electron Microscopy Centre. I would like to extend my acknowledgement to the Graduate Research School, Thesis Examination committee and to the respected thesis examiners.

Finally, and above all, I cannot thank my family enough for their sacrifice and continuous support for bringing me to this level. My special thanks to my lovely wife, Dr Smita Yusuf Nishe and to my little princess, Junairah Ahmed for being companions on this journey.

I would like to dedicate my thesis to my loving parents, MD Jamshed Ali, and Mrs. Rokeya Begum for their unconditional and endless support and encouragement.

# Certification

*I, Al Jumlat Ahmed, declare that this thesis submitted in fulfilment of the requirements for the conferral of the degree Doctor of Philosophy, from the University of Wollongong, is wholly my own work unless otherwise referenced or acknowledged. This document has not been submitted for qualifications at any other academic institution.*

_____

***Al Jumlat Ahmed***

*February 2021*

# List of Names or Abbreviations

| | |
|---|---|
| BET | Brunauer-Emmett_Teller |
| BJH | Barret-Joyner_Halenda |
| CMC | Critical micelle concentration |
| CMT | Critical micelle temperature |
| DSC | Differential scanning calorimetry |
| EDS | Energy dispersive spectroscopy |
| EPSRC | Engineering and physical sciences research council |
| FAST | Field-assisted sintering technique |
| EESEM | Field emission scanning electron microscopy |
| LFA | Laser flash analysis |
| MFP | Mean free path |
| PGEC | Phonon-glass electron-crystal |
| RTG | Radioisotope thermoelectric generator |
| SEM | Scanning electron microscope |
| SDD | Silicon drift detector |
| SPS | Spark plasma sintering |
| STEM | Scanning transmission electron microscope |

| | |
|---|---|
| TMF | Thermoelectromotive force |
| TE | Thermoelectric |
| TEG | Thermoelectric generator |
| TEM | Transmission electron microscope |
| XRD | X-ray Diffraction |
| XPS | X-ray photoelectron spectroscopy |

# List of Publications

**Journal Articles**

1. **Al Jumlat Ahmed**, Frank Yun, David Cortie, Yaser Rehman, Sheik Md Kazi Nazrul Islam, Abdulhakim Bake, Konstantin Konstantinov, Md. Shahriar A. Hossain*, Yusuke Yamauchi and Xiaolin Wang*; "Significant Reduction in Thermal Conductivity and Improved Thermopower of Electron-Doped $Ba_{1-x}La_xTiO_3$ with Nanostructured Rectangular Pores"; Advanced Electronic Materials, 15 March 2021, https://doi.org/10.1002/aelm.202001044

2. **Al Jumlat Ahmed**, Md. Shahriar A. Hossain*, Sheik Md Kazi Nazrul Islam, Frank Yun, Guangsai Yang, Ridwone Hossain, Aslam Khan, Jongbeom Na, Miharu Eguchi, Yusuke Yamauchi, and Xiaolin Wang*; "Significant Improvement in Electrical Conductivity and Figure of Merit of Nanoarchitectured Porous $SrTiO_3$ by La Doping Optimization"; ACS Applied Materials & Interfaces, 2020 12 (25), 28057-28064, https://doi.org/10.1021/acsami.0c01869

3. **Al Jumlat Ahmed**, Sheik Md. Kazi Nazrul Islam, Ridwone Hossain, Jeonghun Kim, Minjun Kim, Motasim Billah, Md. Shahriar A. Hossain*, Yusuke Yamauchi and Xiaolin Wang*; "Enhancement of thermoelectric properties of La-doped $SrTiO_3$ bulk by introducing nanoscale porosity"; Royal Society Open Science 2019 6 (10), 190870R, http://dx.doi.org/10.1098/rsos.190870

**Poster Presentation**

1. **Al Jumlat Ahmed**, Sheikh Md Kazi Nazrul Islam, Ridwone Hossain, MD Shahriar A. Hossain, Yusuke Yamauchi, Xiaolin Wang; "Optimization of La-doping for Improvement of Thermoelectric Performance of Mesoporous $SrTiO_3$"; International Symposium on Future Material, Institute for Superconducting and Electronic Materials (ISEM), University of Wollongong, NSW, Australia; 2019/2/1.

2. **Al Jumlat Ahmed**, Md Shahriar A. Hossain, Yusuke Yamauchi, Xiaolin Wang; "Tuning the Thermal Conductivity of Strontium titanate by Introducing Mesoporosity"; 11th Asia-Australia Conference on Composite Materials (ACCM 11), Cairns, QLD, Australia; 2018/7/1.

# Table of Contents

# List of Figures

# List of Tables

# 1. Introduction

## 1.1Brief Introduction

The thermal energy which is being wasted enormously from different sources can be directly converted into valuable electrical energy using thermoelectric (TE) device [1-4]. Thermoelectric generator (TEG) is one of the potential renewable energy sources. Theoretical calculation shows that more than 60 percent of energy produced worldwide has been wasting in the form of heat continuously. As shown in Fig. 1.1, the waste heat from different sources for instance: exhaust system of vehicle, industrial boilers and chimneys, thermal power plant and even waste heat from the cooking stove can be directly converted into useful electrical energy by thermoelectric generator [1-2, 5]. Therefore, integration of thermoelectric generator with an energy source would improve the overall energy efficiency and sustainability [6]. However, the energy conversion efficiency and lifetime of thermoelectric device are not enough for widely usage. Energy scientists around the globe are working on different thermoelectric materials and device configurations to overcome these hurdles.

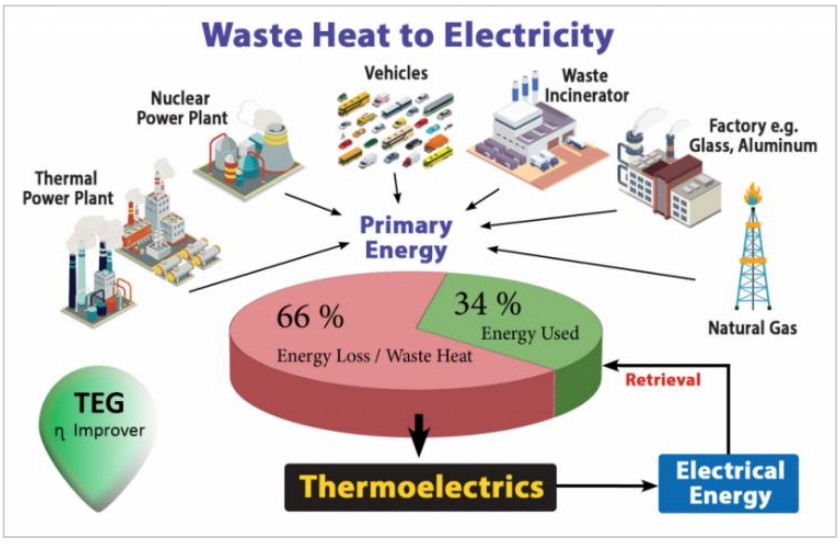


Fig. 1.1 Different sources of waste heat recovery by using thermoelectric[7]

According to the thermoelectric roadmap prepared by the Engineering and Physical Sciences Research Council (EPSRC) Thermoelectric Network UK, the thermoelectric has the capability to integrate with all sort of vehicle from the internal combustion engine, hybrid engine and full electric vehicle[8]. The thermoelectric generator has been integrated with the exhaust system of BMW 530i concept car to improve the fuel efficiency[9]. The yellow box in the Fig 1.2(a) is the TE generator integrated with the radiator of the car. The radioisotope thermoelectric generator (RTG) is used in spaceship to generate electricity from heat of radioactive decomposition as shown in Fig 1.2(b)[6]. The RTG is also used as autonomous power supply for remote infrastructure like in weather station, lighthouse, etc. The TE generator can be integrated with cook stove to use the exhaust heat to generate electricity (Fig 1.2(c)) which could be a sustainable energy technology for developing countries. The TE generator can be also integrated with wearable device to generate electricity from body heat as shown in Fig 1.2(d).


Fig. 1.2 (a) The TE generator is integrated with exhaust system of BMW 530i concept car, (b) The RTG to supply power to the spaceship, (c) The cook stove manufactured by the Biolite company uses the TE technology and (d) The Matrix PowerWatch uses body heat to charge[9]

## 1.2 Research Focus

Conventional Thermoelectric materials for example $Bi_2Te_3$, SnTe, PbTe and $Cu_2Se$ exhibit high thermoelectric performance, but these materials have some limitations such as poor lifetime at high temperature in air, limited sources, and high toxicity. On the other hand, metal oxide based TE materials have high lifetime at high temperature, low-cost, non-toxic and have minimal impact on environment[10]. Some *p*-type metal oxide-based TE materials such as $NaCo_2O_4$, layer-structured cobalt oxide, and BiSeCuO exhibit excellent TE properties. The highest value of figure of merit reaches unity ($zT$ = 1.4 ) for $Bi_{0.875}Ba_{0.125}CuSeO$ [11]. As compared to the *p*-type oxides, *n*-type oxide materials have lower thermoelectric performance. To fabricate a TE module based on oxide materials, the $zT$ of *n*-type oxides should be improved to the level of *p*-type materials.

Strontium titanate (denoted as $SrTiO_3$) is a well-known *n*-type thermoelectric material with the cubic perovskite $ABO_3$ crystal structure having the lattice parameter of 0.3905 nm. The melting temperature of $SrTiO_3$ is 2080$^o$C which gives it chemical as well as thermal stability at high temperature. The lattice thermal conductivity of $SrTiO_3$ is high, 12 W/mK at room temperature which is the main challenge to become a usable thermoelectric material[12]. $SrTiO_3$ with appropriate stoichiometry is an insulator having a band gap of 3.2 eV. However, the electrical conductivity can be changed from insulating to metallic by substitutional doping of $SrTiO_3$ with $La^{3+}$ or $Nb^{5+}$.

$BaTiO_3$ is relatively less popular as a thermoelectric material. However, $BaTiO_3$ has similar cubic perovskite structure like $SrTiO_3$ above its Curie temperature, intrinsically low thermal conductivity and it is stable at high temperature because of high melting point (1650$^o$C).

Therefore, electron-doped $BaTiO_3$ could also be a promising n-type metal oxide thermoelectric material.

## 1.3 Summery of Thesis

The background and research focus of the thesis has been discussed in the introduction chapter. The next chapter is literature review which starts with basic principles of thermoelectric, fundamentals and equations of thermoelectric, different types of thermoelectric materials and their advantages and disadvantages. The main emphasis of the chapter is the detail discussion on latest research on thermoelectric properties of metal perovskite-based materials, $SrTiO_3$ and $BaTiO_3$.

The following experiment chapter has two major sections. The first section discusses the fabrication process of bulk thermoelectric material with nano scale pores by the chemical process named polymer micelle self-assemble, followed by the rapid solidification method called spark plasma sintering (SPS). The optimization of conditions for the SPS process are also discussed in this section. The general discussion on different material characterization techniques like XRD, SEM, EDS, BET, TEM and XPS and thermoelectric properties like electrical conductivity, Seebeck coefficient, thermal diffusivity, specific heat measurements are presented in the second section.

There are three main chapters in the thesis and brief idea of these chapters are available in the following sections. The thesis is concluded with general discussion and findings from the experiments in the chapter 7.

In the chapter 4, The effect of nano scale pores on thermoelectric properties was inspected. For do so, different amounts of surfactant F127 were used as soft template in the samples using the method called polymeric micelle self-assembly. It introduced nanoscale pores into bulk samples of La-doped $SrTiO_3$. It was observed that due to nano pores within the samples, there is a significant improvement of the Seebeck coefficient and remarkable reduction in the thermal conductivity. It was suspected that the improvement in Seebeck coefficient and reduction is thermal conductivity are due to charge carrier and phonon scattering by nano pores, respectively. Therefore, there was an overall enhancement in the power factor (*PF*) as well as the dimensionless figure of merit (*zT*) over a wide range of temperature. The sample, $Sr_{0.8}L_{0.2}TiO_3$ with 600 mg of F127 surfactant denoted as SLTO 600F127 showed the maximum power factor of 1.14 $mWm^{-1}K^{-2}$ at 647 K which is 35% higher than the bare sample without nano pores (SLTO 0F127), and the same sample (SLTO 600F127) showed the maximum value of z*T* is 0.32 at 968 K with an average enhancement of 62% in *zT* in comparison to the bare sample (SLTO 0F127).

In chapter 5, the further improvement of thermoelectric properties of bulk $SrTiO_3$ were achieved by introducing dual mechanism of nano-scale porosity and optimizing carrier concentration by La doping. The X-ray diffraction (XRD), atomic resolution scanning transmission electron microscopy (STEM) imaging and energy dispersive X-ray spectrometry (EDS) results showed that La was doped successfully into the lattice. The SEM images confirmed that all the samples have nearly similar nano-scale pores. The significant enhancement of electrical conductivity over the broad temperature range was observed through optimization of La doping. Additionally, the samples have very low thermal conductivity, which is speculated due to the nano-scale porosity of the samples. Due to this dual mechanism of doping optimization and

nano-scale porosity, there is a remarkable improvement in power factor, 1mW/m$^2$K over wide range of temperature from 650 K to 800 K and figure of merit, *zT* of 0.26 at 850 K of the sample, 22 at% La doped $SrTiO_3$.

In chapter 6, the electrical conductivity of $BaTiO_3$ samples was improved by La doing to yield a n-type $Ba_{1-x}La_xTiO_3$ semiconducting material. To improve the thermoelectric properties further, nanostructured pores were introduced into the bulk $Ba_{1-x}La_xTiO_3$ using F127 surfactant micelles for a chemical templating process, followed by spark plasma sintering. The Brunauer–Emmett–Teller (BET) analysis and transmission electron microscopy (TEM) images revealed that the sample synthesized using the surfactant F127 has nanostructured pores of around 4 nm within a highly crystalline structure. X-ray powder diffraction (XRD) analysis confirmed that all the La doped samples have the cubic $BaTiO_3$ perovskite phase. Scanning electron microscopy (SEM) images showed that all the samples have similar grain boundaries and uniform La doping, which suggests that the large reduction in the lattice thermal conductivity in the F127-treated sample arises primarily from the pore distribution which introduces anisotropic phonon scattering within the unique nanoarchitecture. The thermal conductivity of the sample is less than 2 $W{\cdot}K^{-1}m^{-1}$ at room temperature, and it reduces gradually to 1.5 $W{\cdot}K^{-1}m^{-1}$ at 950K. The sample with 20 at% La doping and nano scale pores also shows a thermopower (Seebeck coefficient) that is doubled compared to the related sample without porosity. Together with the lattice thermal conductivity, this enables a significant improvement in the figure of merit, *zT*.

It can be concluded that the perovskite based thermoelectric materials $SrTiO_3$ and $BaTiO_3$ became *n*-type semiconducting material because of La doping and the electrical conductivity improved significantly due to optimization of La doping. More importantly, the improvement

of Seebeck coefficient and remarkable reduction of lattice thermal conductivity of these materials were evidenced by inclusion of nano scale pores into the bulk samples. As a result, there is an overall enrichment in the figure of merit.

# 2. Literature Review

## 2.1 Basic Principles of Thermoelectric

Before going into details of thermoelectric material and device, it is essential to discuss on relevant basic principles and to express sincere respect and gratitude to the founders of basic science.

### 2.1.1 Seebeck Effect

In 1821-3, Thomas Johann Seebeck found that a circuit made from two dissimilar metals, with junctions at different temperatures would deflect a compass magnet. Later, Seebeck realized that the temperature difference produces an electric potential (voltage) which can drive an electric current in a close circuit. Today, this is known as the Seebeck effect[13]. The produced voltage is proportional to the temperature difference between the two junctions. The proportional constant ($S$) is known as the Seebeck coefficient and its unit is μV/K.

$$s = \frac{V}{\Delta T} \qquad (2.1)$$

Where, $V$ is the Seebeck voltage and $\Delta T$ is the temperature difference between the junctions.

### 2.1.2 Peltier Effect

In 1834, Jean Charles Athanase Peltier found that an electrical current would produce heating or cooling at the junction of two dissimilar metals[13]. In 1838, Lenz showed that depending on the direction of current flow, heat can be either generated or removed from a junction of two

dissimilar metals. The heat generated or removed at the junction is proportional to the electrical current. The proportional constant is known as the Peltier coefficient (π),

$$\pi = \frac{Q}{I} \qquad (2.2)$$

Where, $Q$ is the heat generated or removed at the junction and $I$ is electrical current.

### 2.1.3 Thomson Effect

Twenty years later, William Thomson (later Lord Kelvin) described interrelationship between the Seebeck and Peltier effects through thermodynamics which is known as the Kelvin relations[13]. The Peltier coefficient is simply the Seebeck coefficient times with absolute temperature. This relationship led Thomson to predict a third thermoelectric effect, now known as the Thomson effect. In the Thomson effect, heat is absorbed or produced when current flows in a material with a temperature gradient. The heat is proportional to both the electric current and the temperature gradient. The proportionality constant is known as the Thomson coefficient ($\mu_T$).

$$\mu_T = \frac{Q}{I.\Delta T} \qquad (2.3)$$

Where, $Q$ is the heat absorbed or produced, $I$ is the current and temperature gradient is presented by $\Delta T$.

The relation between the Seebeck and Peltier coefficient is as follow,

$$\pi = S.T \qquad (2.4)$$

Where, $\pi$ represents the Peltier coefficient, $S$ is the Seebeck coefficient and $T$ is the absolute temperature.

## 2.2 Thermoelectric Device

A temperature gradient across a semiconductor can generate an electrical voltage (thermoelectromotive force, TMF) of several hundreds of μV/K. Since *n* and *p* type semiconductors generate the voltage of opposite signs, connecting an *n* and *p* type semiconductor in series doubles the voltage. An n and p type semiconductors are connected in series as shown in Fig. 2.1 is the unit component of a thermoelectric device which directly converts heat into electricity[10].

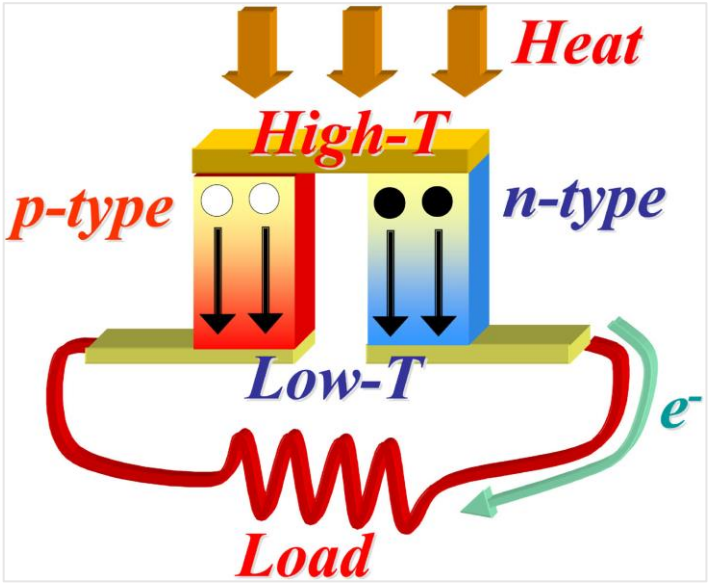


Fig. 2.1 Schematic of a thermoelectric unit couple[10]

## 2.3 Efficiency of Thermoelectric Device

The performance of thermoelectric (TE) device depends on the temperature gradient (ΔT) and dimensionless figure of merit of thermoelectric material. For power generation application, the efficiency of the device is defined by combination of the Carnot efficient ($\Delta T/T_{hot}$) and the figure of merit (*zT*) as shown in the following equation (2.1) [14-15].

$$\eta = \frac{\Delta T}{T_{hot}} \times \frac{\sqrt{1 + zT_{avg}} - 1}{\sqrt{1 + zT_{avg}} + \frac{T_{cold}}{T_{hot}}} \qquad (2.5)$$

Where, $T_{hot}$ and $T_{cold}$ are the temperature of the hot and cold ends of the thermoelectric device respectively. ΔT is the temperature different between the hot and cold ends. $T_{avg}$ is the average temperature of the device. The equation indicates that a large average *zT* value over a wide temperature range is required to increase the efficiency of thermoelectric device. Since a thermoelectric device operates between two temperatures: $T_{hot}$ (the heat source) and $T_{cold}$ (the heat rejection temperature) like other heat engines, efficiency of thermoelectric device is limited to perhaps one sixth of the maximum possible Carnot efficiency[9].

## 2.4 Figure of Merit of Thermoelectric Material

Performance of thermoelectric material is evaluated by dimensionless figure of merit,

$$zT = \frac{S^2 \sigma T}{k} \qquad (2.6)$$

Where, *S, σ, T* and *k* are the Seebeck coefficient (μV/K), the electrical conductivity (S/m), the absolute temperature (K) and the thermal conductivity (W/mK) respectively. And the term $S^2\sigma$ is called the power factor or thermopower of thermoelectric material. For power generation application by TE, a material with high value of power factor is even more important than having a high efficiency, since most waste heat sources are free [16].

Theoretical study shows that thermoelectric material requires *zT* value more than 1 for practical applications[1]. To realize high *zT* value, the thermoelectric material requires large Seebeck

coefficient to get high thermal voltage, high electrical conductivity for minimizing internal resistance and joule heating, and low thermal conductivity to maintain temperature difference between ends of the material[1, 17].

Scientists are working for decades to improve figure of merit of thermoelectric materials. In Fig. 2.2, the timeline of z*T* improvement of different promising TE materials shows that the state-of-the-art TE materials have maximum *zT* value in between of 1 to 2.5 even though, it is highly challenging to improve *zT* because of adverse interdependency of transport parameters: Seebeck coefficient (*S*), electrical conductivity ($\sigma$) and thermal conductivity ($\kappa$).

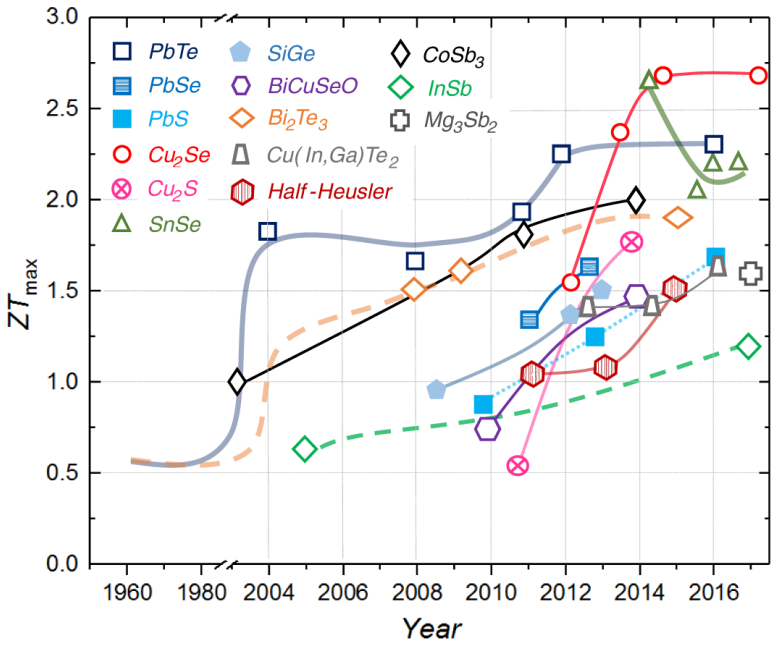


Fig. 2.2 Timeline of maximum ZT value for most promising thermoelectric materials[6]

The power generation efficiency of TE material is directly related to *zT* value and operating temperature. The efficiency of TE material with respect to *zT* value and source temperature is presented in Fig. 2.3. The comparison with conventional energy conversion systems in term of

efficiency is also presented in the figure. The figure shows a TE material with *zT* value of 0.5 has around 10% power generation efficiency if source temperature is 1000K.

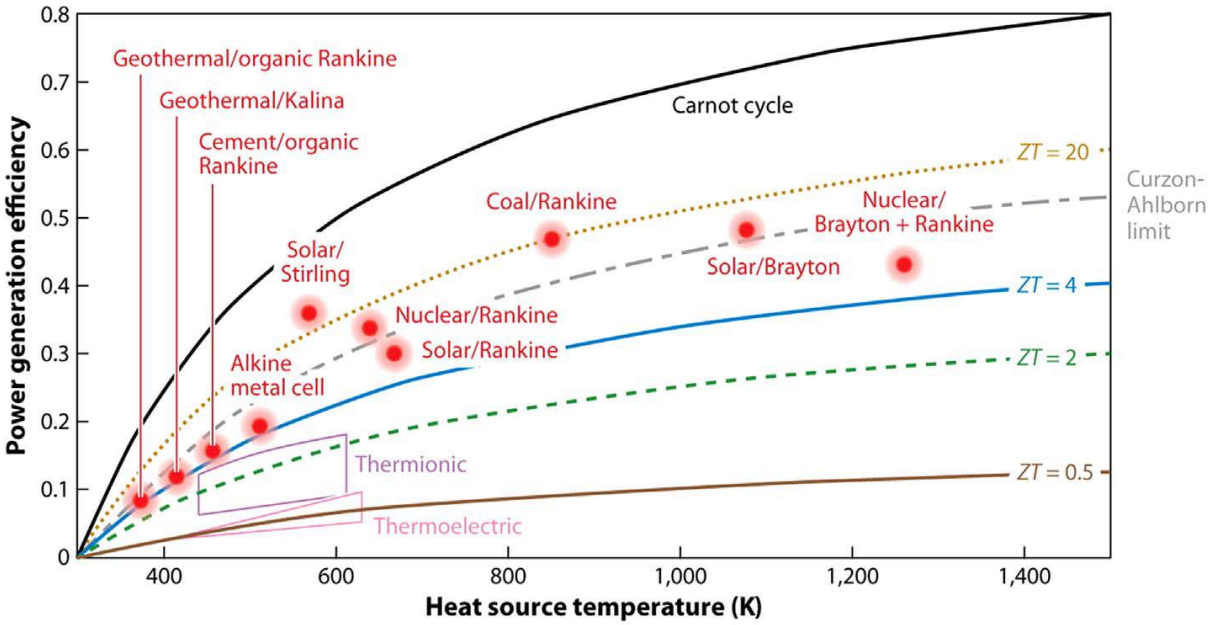


Fig. 2.3 Power generation efficiency of TE materials with respect to different ZT values and heat source temperature[6]

## 2.5 Seebeck Coefficient

Seebeck coefficient is an intrinsic material property, which represents the energy difference between the averaged charge carrier energy versus the Fermi energy. It can be expressed as follow[16],

$$S = \left(\frac{k_B}{-\mathrm{q}}\right)\left(\frac{E_c - E_F}{k_B T} + \frac{\Delta_n}{k_B T}\right) \qquad (2.7)$$

Where $E_F$ is Fermi energy level and $k_B$ is the Boltzmann constant. For semiconductors, the Seebeck value can be negative (electron conduction) or positive (hole conduction). For Large Seebeck coefficient, there should be a single type of carrier in the material. Mixed n-type and

p-type charge carrier will cancel out the induced Seebeck voltages. For doped semiconductors, the relationship of the Seebeck coefficient with carrier concentration can be expressed as follow [18]

$$S = \frac{8\pi^2 k_B^2}{3eh^2}\, m^* T \left(\frac{\pi}{3n}\right)^{2/3} \qquad (2.8)$$

Where, $k_B$ is the Boltzmann constant (1.38 x $10^{-23}$ $m^2$ Kg $s^{-2}$ $K^{-1}$), e is the electron charge (1.60 x $10^{-19}$ c), $h$ is the Planck constant (6.63 x $10^{-34}$ $m^2$ Kg $s^{-1}$), $m^*$is effective mass of the carrier, $T$ is the Absolute temperature and $n$ is the carrier concentration.

## 2.6 Electrical Conductivity

The electrical conductivity is directly proportional to the carrier concentration and the carrier mobility.

$$\sigma = n\, e\, \mu \qquad (2.9)$$

Where, $n$ is the carrier concentration, e is the charge of electron and $\mu$ is the carrier mobility. The carrier mobility is related to grain size and potential barrier height and It can be expressed as follow [19],

$$\mu = L\, e \left(\frac{1}{2\pi m^* k_B T}\right)^{\frac{1}{2}} \exp\left(\frac{eV_b}{k_B T}\right) \qquad (2.10)$$

Where, L is the grain size and $V_b$ is the potential barrier height.

## 2.7 Thermal Conductivity

The thermal conductivity of a material is a multiplication of the thermal diffusivity, the specific heat and the density of the material[12].

$$k = \alpha \, C_p \, \rho \qquad (2.11)$$

Where, $\alpha, C_p, \rho$ are the thermal diffusivity, the specific heat at constant pressure and the density of the material, respectively. The thermal diffusivity ($m^2 s^{-1}$) measures the rate of transfer of heat from the hot side to the cold side of a material. And the specific heat ($J kg^{-1}K^{-1}$) is the required amount of heat to raise temperature of 1 kg of mass by 1k. The thermal conductivity $k$ has two components, $k_{el}$ is the thermal conductivity from movement of the electrons and the holes, and $k_{ph}$ is the contribution from the movement of phonons through the lattice[15].

$$k = k_{ph} + k_{el} \qquad (2.12)$$

According to the Wiedemann-Franz law, the $K_{el}$ is proportional to electrical conductivity and temperature,

$$K_{el} = LT\sigma \qquad (2.13)$$

Where, $L$ is the Lorenz number and it is common practice to treat L as a universal factor with value of $2.44 \times 10^{-8} \, w \, \Omega \, K^{-2}$ for degenerate semiconductor[15]. However, there is a significant deviation in Lorenz number for non-degenerate semiconductors where L converges to $1.5 \times 10^{-8} \, w \, \Omega \, K^{-2}$ [20].

Since electronic thermal conductivity $k_{el}$ is related to electrical conductivity and high electrical conductivity is prerequisite for thermoelectric material. The lattice thermal conductivity $k_{ph}$

has to be reduced to lower the overall thermal conductivity. The lattice thermal conductivity can be expressed by,

$$K_{ph} = \frac{1}{3} C_v V l \qquad (2.14)$$

Where, the heat capacity ($C_v$) and the phonon velocity ($V$) are constant, so the lattice thermal conductivity mainly depends on the phonon mean free path (MFP) ($l$).

## 2.8 Phonon Scattering Mechanisms

There are two types of phonons, one is acoustic phonons and another one is optical phonons. However, acoustic phonons carry most of the heat in a material and they have a spectrum of wavelengths including short, medium, and long wavelength phonons. The defects in the material scatter phonons effectively when their size is close to wavelength of phonons. The short wavelength phonons are scattered by the point defects in the crystal structure. Nano scale precipitates like nano pores or nano size inclusions in the material scatter phonons of medium wavelength. The long wavelength phonons are scattered by the grain boundaries. Therefore, all length-scale structures like point defects, nano-scale precipitates and grain boundaries are necessary to be included in the thermoelectric material to scatter board spectrum of heat carrying phonons as shown in following figure[5].

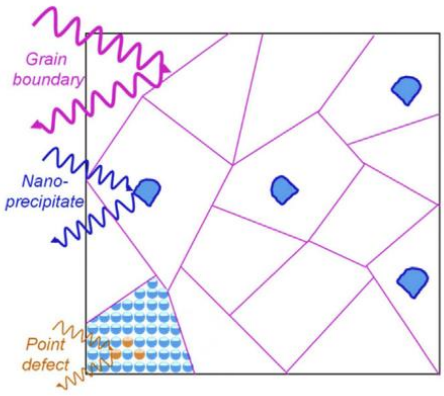


Fig. 2.4 All length-scale structures like point defects, nano-scale precipitates and grain boundaries to scatter short, medium and long wavelength phonons respectively[5].

One of the most important approaches for improving the figure of merit is to use the Phonon-Glass Electron-Crystal (PGEC) approach. PGEC is a concept where the material should have a lower thermal conductivity like the amorphous materials such as glass, while good electronic properties like the semiconductor crystals.

## 2.9 Effect of Carrier Concentration on Thermoelectric Properties

From equation 2.4 and 2.5, the Seebeck coefficient has inverse relation with carrier concentration, but the electrical conductivity is directly proportional to carrier concentration. The dependency of the parameters on carrier concentration is shown in Fig. 2.5. The optimum doping level is in degenerate semiconductor region. According to earlier studies, the power factor has maximum value at a carrier concentration in the order of $10^{19}$ $cm^{-3}$ for generally all type of materials[10].

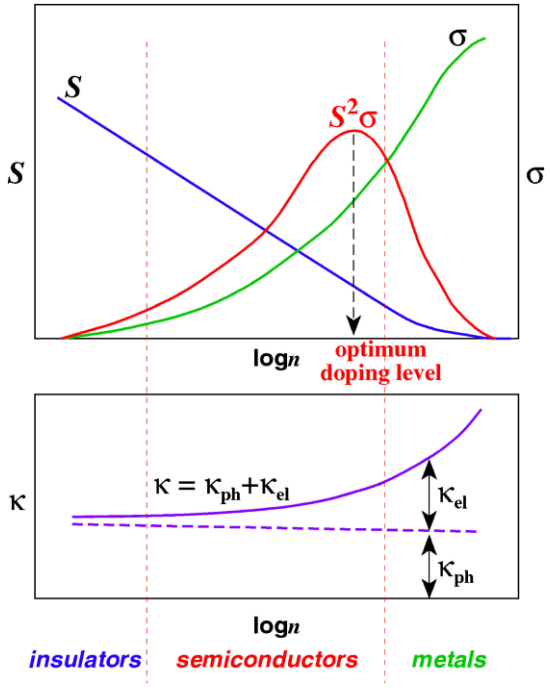


Fig. 2.5 The dependency of the Seebeck coefficient, the electrical conductivity and the thermal conductivity on the carrier concentration[10]

## 2.10 Thermoelectric Materials

Different metal compounds like Skutterudites, metal-chalcogenide compounds, silicide compounds are common thermoelectric materials. However, transition metal oxides are also gaining interest as thermoelectric material because of their chemical stability and environmental compatibility. Detail discussion on different thermoelectric materials and their advantages and disadvantages are discussed in the following sub sections. Typical sources of waste heat and operation temperature of different thermoelectric materials are shown in Fig. 2.6[10].

### 2.10.1 Metal Chalcogenide

Metal chalcogenide compounds such as metal telluride ($Bi_2Te_3$, PbTe, $Sb_2Te_3$) and metal selenide ($Cu_2Se$, SnSe, $Sb_2Se_3$) are conventional thermoelectric materials. These materials

show high electrical conductivity because of small energy bandgap of around 1 eV. They also have heavy atoms, so low atomic vibration and low lattice or phonon thermal conductivity. $Bi_2Te_3$ is commercially available thermoelectric material suitable for ambient temperature applications. However, the conventional thermoelectric materials have some shortcomings: poor durability at high temperature in air, low abundance, high cost and toxic.

### 2.10.2 Skutterudite and Clathrate

Metal-arsenide and metal-antimonide compound materials are known as Skutterudite such as $CoSb_3$, $CoAs_3$, GaAs. These compound materials can have rattler atoms inside the hollow crystal structure which vibrates at a frequency different from crystal lattice frequency. Due to the disharmony in vibration frequencies, the phonon thermal conductivity reduces by scattering. Clathrate compounds for example $Ba_8Ga_{16}Ge_{30}$, $Si_2Ge$ also have cage type structure and rattler atom inside the crystal structure vibrates at different frequency of the crystal which helps to reduce the thermal conductivity.

### 2.10.3 Silicide

Silicide compounds like $MgSi_2$ and $MnSi_2$ have the Seebeck coefficient and the electric conductivity comparable to commercially available $Bi_2Te_3$ but the thermal conductivity is hundred times larger than of $Bi_2Te_3$.

### 2.10.4 Transition Metal Oxide

Transition metal oxide based thermoelectric materials are highly robust at high operating temperature in air, non-toxic, low cost and minimal in environment impact. Some transition metal oxide materials like $NaCo_2O_4$, layer-structured CoO and BiSeCuO exhibit excellent

thermoelectric properties as a p-type semiconducting material. The highest figure of merit reaches unity ($zT$ = 1.4 ) for $Bi_{0.875}Ba_{0.125}CuSeO$ [11]. However, oxide materials are inferior in thermoelectric performances as a n-type semiconducting material. To fabricate TE module, the figure of merit of n-type oxide materials should be improved at least to the level of p-type oxide materials.

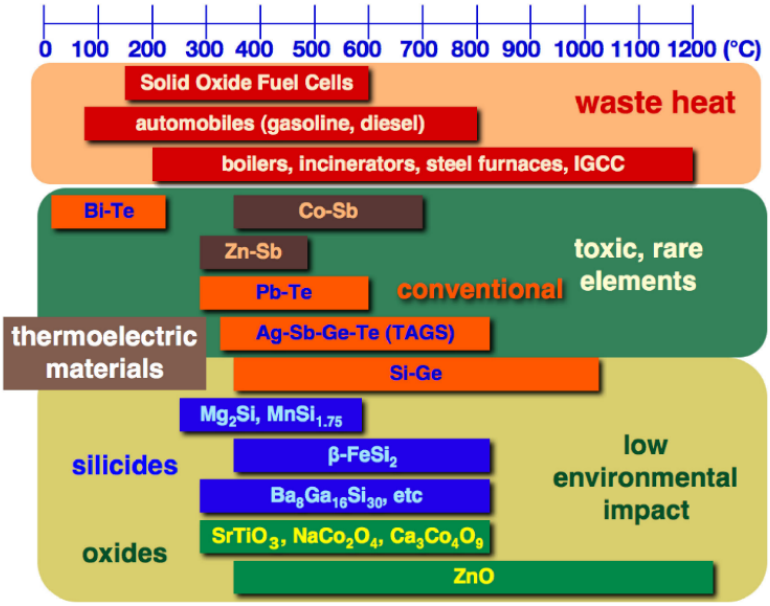


Fig. 2.6 Different sources of waste hear recovery and operation temperature of different thermoelectric materials[10]

So far in this chapter, general discussion on basic principles of thermoelectric, different physical properties of thermoelectric material and different types of thermoelectric material have been done in the previous sections. In the following sections of this chapter, the detail discussion and summery of previous works on $SrTiO_3$ and $BaTiO_3$ are going to be emphasized. Since subsequent experimental chapters are focused on thermoelectric properties of $SrTiO_3$ and $BaTiO_3$.

## 2.11 Strontium Titanate ($SrTiO_3$)

Strontium titanate ($SrTiO_3$) is a well-known metal oxide material with cubic perovskite ($ABO_3$) crystal structure having lattice parameter of 0.3905 nm. The melting temperature is 2080ºC which makes it stable at high temperature. Stoichiometric $SrTiO_3$ is an insulator with energy bandgap of 3.2 eV. However, its electrical conductivity can be changed from insulator to metallic by substitutional doping. For example, doping with $La^{3+}$ or $Nb^{5+}$ on A and B sites of $ABO_3$ crystal structure, respectively. The atomic density of $SrTiO_3$ is 5.12 g $cm^{-3}$.

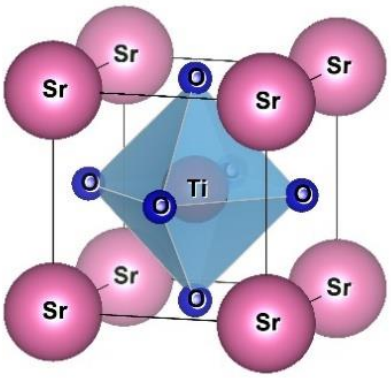


Fig. 2.7 Atomic structure of SrTiO3 at room temperature

The mathematical modelling of La-doped $SrTiO_3$ with respect to carrier concentration and temperature predicts that the figure of merit *zT* value can reach 0.7 at 1400 K [21]. Another study shows that the thermal conductivity can be reduced by nanoscale porosity in the material but high density sample is required for maintaining higher electrical conductivity[22]. Further discussion on different mechanisms applied to improve thermoelectric properties of $SrTiO_3$ is presented as follow.

Commonly applied mechanisms such as carrier concentration optimization, band gap engineering, create defect in crystal structure, optimizing sintering conditions and nano size metal inclusion were applied to enhance figure of merit of $SrTiO_3$.

The highest *zT* value of 0.41 at 973K was reported for La doped $SrTiO_3$ ($Sr_{1-3x/2}La_xTiO_{3-\delta}$ with $0.125< x <0.175$) [23-24]. It was achieved by creating defective in perovskite lattices containing of A- and O- site vacancies with mixed valent $Ti^{3+}$ and $Ti^{4+}$ on the B-site. In another study, La doped $SrTIO_3$ is prepared by combustion synthesis followed by spark plasma sintering at 1573 K for different holding time. The sample $Sr_{0.92}La_{0.08}TiO_3$ sintered at 1573 K for 5min showed *zT* value of 0.37 at 1045 K [25].

Nanostructured bulk La-doped $SrTIO_3$ materials were produced by spark plasma sintering of chemically synthesized colloidal nanocrystals. The nanostructured bulk of the 9 at% La-doped $SrTIO_3$ exhibited a maximum *zT* of 0.37 at 973K[26]. In a similar study, the thermoelectric properties of $Sr_{1-x}La_xTiO_3$ nanoparticles fabricated by the hydrothermal method followed by cold pressure were investigated [27]. The bulk sample prepared by nanoparticle has numerous interfaces which strongly suppresses the phonon thermal conductivity and the *zT* value was 0.12 at 300 K. In another study, $Sr_{1-x}La_xTiO_3$ ($x$=0, 0.02, 0.05, 0.08) nanoparticles were directly prepared by mechanical alloying followed by carbon burial sintering to produce bulk samples. The *zT* changed with increase of La content and the maximum *zT* value was 0.06 at 300K for $x$=0.02 and 0.20 at 1000K for $x$=0.08 [28].

It was reported that addition of nano-sized Ag metal particles in $Sr_{0.9}La_{0.1}TiO_3$ causes an increase in carrier concentration and acts as electrical connections between the grains. It improved the electrical conductivity and reduced the thermal conductivity. The maximum *zT* value of 0.30 at 883K was obtained from the sample with 20 wt% of nano-sized Ag [29].

Investigation on effect of mesoporous structure on the TE properties of La-doped $SrTiO_3$ films showed that the mesoporous structure decreased the thermal conductivity and increased the Seebeck coefficient by increasing phonon and carrier scattering. The increase of electrical resistivity was smaller than the improvement in the Seebeck voltage and thermal conductivity. The incorporation of Brij-S10 surfactant into La-doped $SrTiO_3$ films increased the figure of merit and maximum value was approximately 0.025 at 473K was obtained from the sample which has surfactant Brij-S10 in molar ratio of 0.1 [30]. The TE properties of mesoporous $STiO_3$ films with Brij-S10 surfactant were further improved by substituting Ti with V-group elements like Nb and Ta. The improvement in TE properties was due to increase in effective mass by enlarging bond length of Nb (or Ta) – O. The value of figure of merit *zT* was reported close to 0.04 at room temperature [31].

N. Wang et al. improved the thermoelectric performance of Nb-doped $SrTiO_3$ ($SrNb_{0.15}Ti_{0.85}O_3$), by nano-inclusion of yttria stabilized zirconiz (YSZ) with low thermal conductivity and the *zT* value enhanced up to 0.21 at 900 K [32]. In another study, The Nb doped $SrTiO_3$ with A-site vacancies was prepared by high energy ball milling followed by carbon burial sintering. The maximum value of *zT* was 0.21 at 1100 K for 10 at% Nb doped sample which is sintered at 1773 K [33].

J. Wang et al. reported record high *zT* value more than 0.6 at 1100K for 10 mol% La and 10 mol% Nb co-doped $SrTiO_3$ bulk sample with nano-scale modulation doping and controlled microstructure[34]. E. Li et al. obtained *zT* value of 0.33 at 900 K in surface modified Nb-doped $SrTiO_3$ which had nanosized titania in between of strontium titanate grains made by liquid phase deposition approach [35].

J. Liu et al. found that the ionic radius of doping elements have an important role on thermoelectric properties of $SrTiO_3$ [36]. $SrTiO_3$ ceramics doped with large sized rare earth ions like La, Nb and Sm showed large power factor, on the other hand the ceramics doped with small ions like Gd, Dy, Er and Y showed low thermal conductivity. $SrTiO_3$ ceramic mainly doped with large ions of La and simultaneously, slightly co-doped with small ions of Y ($Sr_{0.8}La_{0.18}Y_{0.02}TiO_3$) exhibited *zT* value of 0.31 at 1023K which is 19% higher than the *zT* value of single doped $Sr_{0.8}La_{0.2}TiO_3$ [36].

Inclusion of Cu or Fe with co-doping $Sr_{0.8}La_{0.067}Ti_{0.8}Nb_{0.2}O_{3-\delta}$ increased the *zT* from 0.25 at 1000K for the control sample to *zT* of 0.36 at 900K for the Cu containing sample and to 0.38 at 1000K for the Fe containing sample. The metal inclusion improved the *zT* value by increasing carrier concentration and carrier mobility which leaded to a reduction in electrical resistivity by a factor of 5 and increase in powder factor by 75%[37].

In case of La and Dy co-doping into Sr-deficient $SrTiO_3$ ceramics, the grain size reduced remarkably with increasing Dy content. This leaded to increase in the electrical conductivity with a slight increase in the Seebeck coefficient and clear decrease in the thermal conductivity. The highest value of *zT* for La and Dy co-doped Sr-deficient SrTiO3 ceramics was reported 0.29 at 773K[38]. In another case of La and Dy co-doping into Sr- deficient $SrTiO_3$ ceramics, the electrical conductivity increased, and the thermal conductivity decreased with increase in vacancies of Sr and O. The highest value of *zT* was reported 0.19 at 773K for the sample $La_{0.1}Dy_{0.1}Sr_{0.75}TiO_3$ [39].

Composite of pure $SrTiO_3$ and La and Nb co-doped $SrTiO_3$ with molar ratio of 1:1 was prepared by the hydrothermal method followed by high-efficiency carbon buried sintering method. The composite had low thermal conductivity and high Seebeck coefficient. The highest *zT* value of

0.35 at 1000 K is achieved from the composite of $SrTiO_3$ with 10 mol% La and 20 mol% Nb co-doped $SrTiO_3$[40].

La and Nb co-doped $SrTiO_3$ ceramics were synthesized under various reducing atmospheres. The presence of $Ti^{3+}$ in heavily reduced specimens increased the electrical conductivity. The maximum $zT$ value of 0.221 at 473 K was obtained from the sample with 5 mol% La and 5 mol% Nb[41]. In another study, a phonon scattering model was proposed to explain that the thermal conductivity of $SrTiO_3$ can be reduced by annealing treatment[12]. The addition of $TiB_2$ powder with Y-doped SrTiO3 was not only effective for increase in the electrical conductivity but also for rapid densification during sintering[42].

Role of various structural defects in electrical and thermal transport was studied in $Sr_{1\pm y}Ti_{0.9}Nb_{0.1}O_{3\pm\delta}$ as a model system [43]. A-site cation vacancies provides a combined effect of charge transport in the perovskite lattice and suppressing the thermal conductivity mostly due to simultaneous generation of oxygen vacancies. Oxygen defects generate electrons as carriers in the sample. Increase in the sintering temperature leads to an increase in the oxygen defect content and thereby resulting in higher electrical conductivity[44]. $SrTiO_3$ is required to sinter in reducing conditions to be became blue or black in colour and electrically semiconducting or metallic[24].

As it is mentioned before that the thermal conductivity can be reduced by introducing nanoscale porosity in the material but high density of sample is required for maintaining higher electrical conductivity[22]. The mean free path of phonon is in the order of $10^{-8}$ which is close to nanometre. So, it is possible to scatter the phonon with some nano pattern without hampering the electron flow. During bulk thermoelectric materials preparation, the main challenge is to make fully dense pellet and keeping the nanostructure. Nanostructured bulk thermoelectric La-doped

$SrTiO_3$ materials were produced by SPS of chemically synthesized colloidal nanocrystals. The nanoscale interfaces were available even after the sintering process. The nanostructured bulk of the La-doped $SrTiO_3$ exhibited high *zT* value of ~ 0.37 at 973 K at 9 at % La doping[26].

It was shown that embedding nanoparticles of soft magnetic materials like Fe, Ni, Co in a TE material like $Ba_{0.3}In_{0.3}Co_4Sb_{12}$ gives dual control of phonon and electron transport properties [45]. The superparamagnetic behaviour of nanomagnetic material leads to three kinds of thermoelectromagnetic effect: charge transfer from the magnetic inclusions to the main material, multiple scattering because of both the magnetic fluctuations and the nanostructure. These effects effectively manipulate electron and phonon transport at nano meter scale and thereby improve the TE performance.

## 2.12 Barium Titanate ($BaTiO_3$)

Barium titanate ($BaTiO_3$) is a very well-studied material and is very popular as a lead-free ferroelectric (piezoelectric) material[46]. The crystal structure of $BaTiO_3$ changes with temperature. Above the Curie temperature (120$^o$C), it has a cubic crystal structure. Below the Curie temperature and within ambient temperature (120 to 5$^o$ C), one of the axes (c axis) stretches, while the other two axes shrink, as the crystal structure becomes tetragonal. Between 5$^o$C to -90$^o$C, it has an orthorhombic structure and below -90$^o$C, it has the rhombohedral structure.

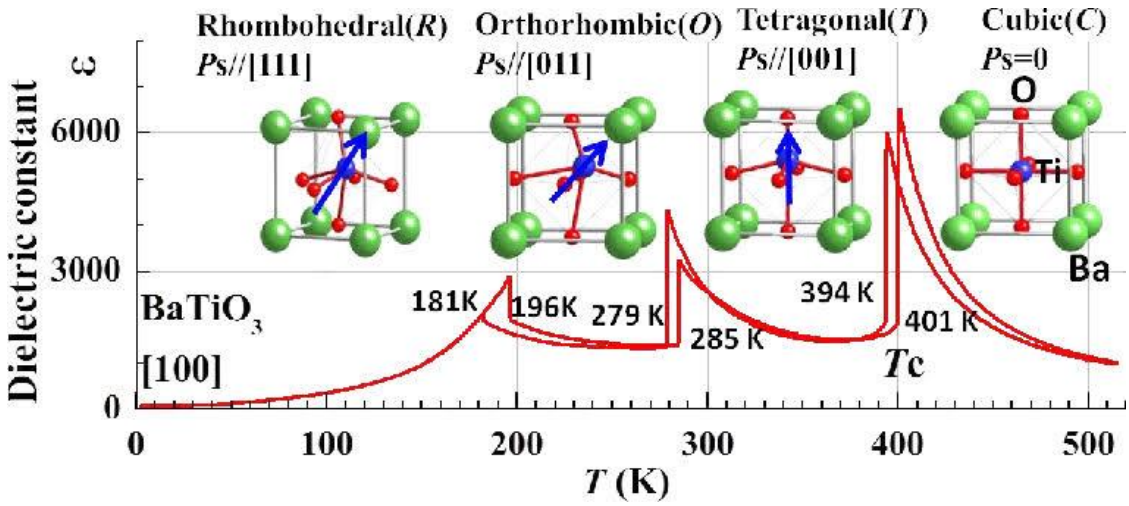


Fig. 2.8 Phase transition of $BaTiO_3$ with temperature[47]

Above the Curie temperature, $BaTiO_3$ does not show any piezoelectric effect due to its cubic perovskite structure. However, it has a similar cubic perovskite structure like $SrTiO_3$ above the Curie temperature, but its thermoelectric properties are not well studied [48-49]. A previous theoretical study compares the thermoelectric properties of $SrTiO_3$ and $BaTiO_3$. The study describes that due to the high lattice constant (4.060 Å) of $BaTiO_3$ compare to $SrTiO_3$ (3.928 Å), the $BaTiO_3$ has low electrical conductivity but high Seebeck coefficient in terms of carrier concentration [48]. The thermal conductivity at room temperature of $BaTiO_3$ is also low (6 $w \cdot K^{-1}m^{-1}$) compared to $SrTiO_3$ (12 $w \cdot K^{-1}m^{-1}$). These points indicate that the $BaTiO_3$ could be a potential thermoelectric material.

Some experimental studies were done on the thermoelectric properties of $BaTiO_3$. Thermoelectric properties of Fe doped $BaTiO_3$ were investigated at high temperature. The XRD result showed the crystal structure of Fe doped $BaTiO_3$ have mixtures of tetragonal and cubic perovskite $BaTiO_3$ phases. The study showed, electrical conductivity increases with temperature and Fe concentration because of the substitution of $Ti^{4+}$ with $Fe^{3+}$ which increases

the oxygen vacancy. The power factor also increases with temperature and Fe concentration. The mixed structure of crystal phases has good potential for enhancing the thermoelectric properties[50].

In another study, Barium titanate and graphene oxide composites were prepared by spark plasma sintering technique with wt% of graphene oxide up to 4%. The maximum *zT* value of 0.008 at 550K was achieved from the sample with 1.7% of graphene oxide [51]. It was also reported that the Eu substitution in reduced $Ba_{1-x}Eu_xTiO_{3-\delta}$ slightly decreases the Seebeck coefficient and enhances the thermal conductivity. But it improves the electrical conductivity significantly by reducing the bandgap. The sample $Ba_{1-x}Eu_xTiO_{3-\delta}$, $x$= 0.9 showed a *zT* of 0.25 at 1100K [52]. The thermoelectric properties of La doped $SrTiO_3$-$BaTiO_3$ solid solution were studied for different levels of Sr substitution. It demonstrated, the electrical conductivity increases, but the Seebeck coefficient decreases with increasing Sr concentration, which is related to the lattice parameter. The result also indicated that shorter Ti-Ti distance is desirable for improvement in the power factor. However, the thermal conductivity increases with Sr concentration which disagrees with the point defect scattering theory[53].

Conducting polyaniline (PANI) and $BaTiO_3$ nanoparticles composite films were prepared and investigated for thermoelectric properties[54]. The outcome of the study was, the composite film behaves like a *p*-type thermoelectric material and the electrical conductivity improves compared to pure $BaTiO_3$, but the Seebeck coefficient recedes. Therefore, there was no significant improvement in the power factor of conducting polyaniline and $BaTiO_3$ nanoparticles composite film. In another study, Lead magnesium-niobate $Pb(Mg_{1/3}Nb_{2/3})O_3$ (PMN) was incorporated in different contents to pure $BaTiO_3$ to improve its thermoelectric efficient by increasing the degree of A and B site disordering by $Pb^{2+}$ and (Mg, Nb $)^{4+}$ ions. It showed that by increasing the contents of PMN, the electrical conductivity increases and the

thermal conductivity decreases. Therefore, there was an overall improvement in the thermoelectric performance of PNM incorporated $BaTiO_3$[55].

Complex double perovskites $Ba_xSr_{1-x}TiFeO_6$ with $0.0 \leq x \geq 0.25$ showed *p*-type thermoelectric behaviour and the sample with $x= 0.25$ showed very high thermo-power of 800 µV/K at 1123K [56]. On the other hand, Niobium doped barium titanate ($BaNb_xTi_{1-x}O_3$) exhibited *n*-type thermoelectric behaviour whose electrical conductivity was directly proportional to the temperature [57]. Yttrium doped *n*-type $BaTiO_3$ showed thermo-power of - 550 µV/K at 350K [58].

# 3. Experiment

There are different synthesis techniques were used to prepare bulk oxide thermoelectric materials. It was reported that the high performance $SrTiO_3$ with La-Nb co-doping, was prepared by a combination of hydrothermal method and high-efficiency sintering. Nano-scale co-doping is successfully modulated by hydrothermal method, and nano-inclusions precipitate during sintering process, to form complex microstructures[34]. The Nb-doped $SrTiO_3$ ceramics doped with the surface modification of nanosized titania was prepared via liquid phase deposition approach and subsequent sintered in an Ar atmosphere[35]. In another study, high density $Sr_{0.8}La_{0.067}Ti_{0.8}Nb_{0.2}O_{3-\delta}$ ceramics containing of Cu or Fe were prepared by the mixed oxide route and sintered under reducing conditions at 1700 K[37]. $Sr_{1-x}La_xTiO_3$ (x=0, 0.02, 0.05, 0.08) nanoparticles were directly prepared by mechanical alloying, followed by carbon burial sintering to produce the bulk thermoelectric sample. The purpose is to obtain pure phase and fine microstructures[28]. Sr-deficient $SrTiO_3$ with La and Dy co-doped powders were synthesized via the sol-gel method, followed by sintering at 1550$^oC$ under a reducing atmosphere[38-39]. A rapid synthesis process at a low temperature of thermoelectric Y-doped $SrTiO_3$ was tried by using the polymerized complex process and the spark plasma sintering method with addition of $TiB_2$ powder[42]. Based on the summary of different fabrication methods, I decided to prepare powder samples with nano porosity using chemical process called polymeric micelle self -assembly method, followed by quick densification method called spark plasma sintering (SPS) at reducing atmosphere to prepare bulk thermoelectric samples with nano scale pores and nano-crystallinity.

## 3.1 Sample Preparation

There are two main steps of nano structured bulk sample preparation. At first, powder samples with nano porosity preparation using chemical process called polymeric micelle assemble method. Secondly, bulk samples preparation from the powder using the Spark plasma sintering (SPS) technique. Both the steps are discussed in detail in the following subsections.

### 3.1.1 Powder Preparation by Polymeric Micelle Assembly Method

Electron doped metal oxide ($SrTiO_3$ and $BaTiO_3$) powder with nano scale porosity have been prepared by polymeric micelle assembly method. The commercially available poly (ethylene oxide)-*block*-poly(propylene oxide)-*block*-poly(ethylene oxide) symmetry triblock copolymer commonly known as Pluronic F127 ($PEO_{100}PPO_{65}PEO_{100}$) has been used as template to form nano scale pores into the material[59].

The hydrophilic group PEO of Pluronic F127 is known to form the crown-ethers structure and the PPO is the hydrophobic group. At a concentration higher than the critical micelle concentration (CMC), the block copolymers start to aggregate for forming micelles [60]. The shape of the micelles depends on length of PO and EO group, concentration of block copolymer and temperature. The micelle has hydrophobic core created by PPO chains and hydrophilic shell created by PEO chains. The temperature at which the micelles are formed is called critical micelle temperature (CMT) and most of the Pluronic copolymers, the CMT is range between 25$^o$C to 40$^o$C [60].

Similar technique is presented in the following figure where polystyrene-*block*-poly(vinylpyridine)-*block*-poly (ethylene oxide) (in short PS-*b*-PVP-*b*-PEO) asymmetry block

copolymer were used as template to synthesis mesoporous $TiO_2/SiO_2$ hybrid film by polymeric micelle assembly method[61-62].

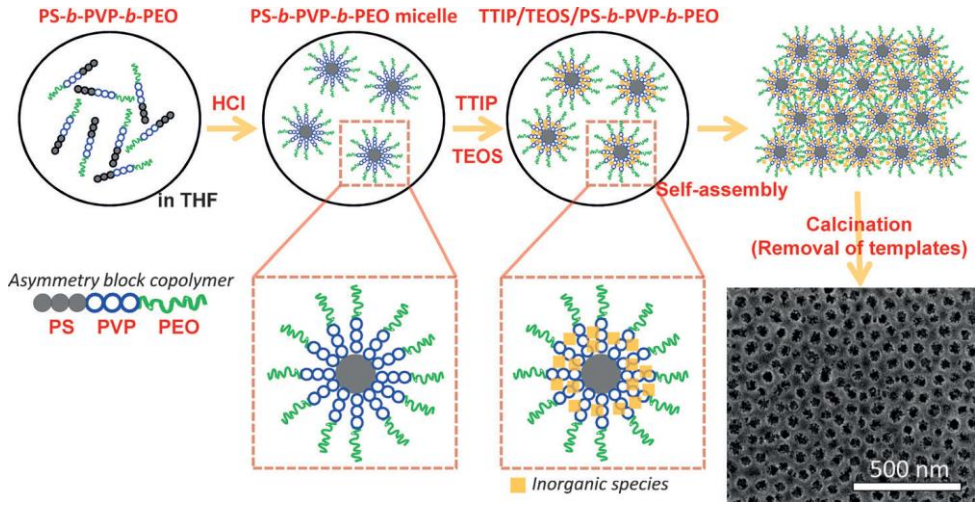


Fig. 3.1 Mesoporous TiO2/SiO2 hybrid film by polymeric micelle assembly method[62]

### 3.1.2 Bulk Sample Preparation using Spark Plasma Sintering

The spark plasma sintering (SPS) is also known as field-assisted sintering technique (FAST)[63]. It is a low voltage, pulsed high DC current and pressure assisted sintering and synthesis technique. In this technique, pulsed high DC current directly passes through the graphite die as well as the powder within the die. In case of conducting powder sample, the resulting heat is generated internally this is known as joule heating. A very fast heating and cooling rate and very short sintering time in SPS, lead to a rapid densification of powder and prevent grain growth and nano structure.

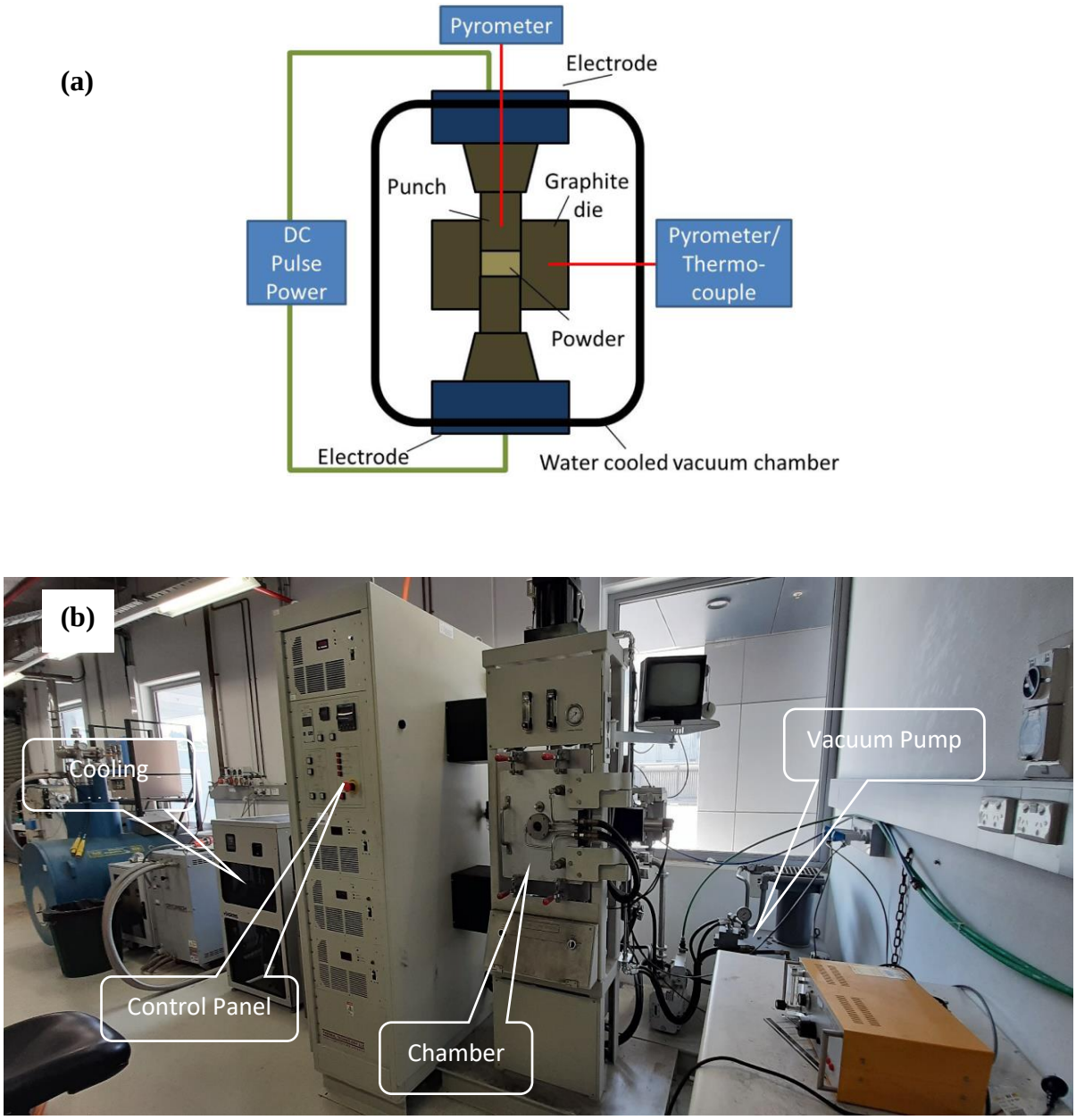


Fig. 3.2 (a) Working schematic of spark plasma sintering machine, (b) Main parts of Spark Plasma Sintering (SPS) machine.

### 3.1.3 Study on Spark Plasma Sintering (SPS) Conditions

Conditions for spark plasma sintering (SPS) like sintering temperature, pressure, holding time and heating and cooling rate for spark plasma sintering of metal oxide thermoelectric materials were reported in different literatures. Sintering conditions for preparing bulk sample of $SrTiO_3$

are summarized in the Table 3.1 with some additional information. Proper sintering conditions for SPS can improve efficiency of thermoelectric material. Bulk material with nanostructure sintered in SPS can reduce the thermal conductivity of the material dramatically while maintaining the electrical transport properties[63]. Sol-gel process followed by SPS significantly decreased the thermal conductivity of $SrTiO_3$ based ceramics. The lowest value of thermal conductivity was reported 1.19 $Wm^{-1}K^{-1}$ of the sample sintered at 1203K in SPS [64].

Table 3.1 Conditions for spark plasma sintering of pure and doped $SrTiO_3$ samples

| **Doping** | **Temp (ºC)** | **Pressure (MPa)** | **Holding time (min)** | **Heating and cooling rate (º C/ min)** | **Comment** | **Ref** |
|---|---|---|---|---|---|---|
| $SrTiO_3$ | 875 | 200 | 5 | | grain size = 80 nm | 65 |
| | 900 | | 3 | | grain size < 100 nm | |
| | 950 | | 0 | | grain size < 100 nm | |
| $SrTi_{0.8}Nb_{0.2}O_3$ | 1300 | 50 | 1 | | $zT$ = 0.2 | 17 |
| $La_{0.08}Sr_{0.92}TiO_3$ | 930 | 40 | 5 | 100k/min up to 100 k below from the peak point and then 50K/min up to the peak point | κ = 1.19 $Wm^{-1}k^{-1}$ at 773 K<br>Grain size 300 to 400 nm<br>Relative density 77.8% | 64 |
| | 1000 | | | | Grain size 300 to 400 nm<br>Relative density 82.3%<br>$zT$=0.0013 | |
| | 1100 | | | | S = 196 $mVK^{-1}$ at 679 K<br>Grain size ~3 micron<br>Relative density 87.6%<br>$zT$=0.08 | |
| | 1200 | | | | Grainsize ~3 micron<br>Relative density 91.6% | |

| | | | | | | |
|---|---|---|---|---|---|---|
| | | | | | ZT=0.08 | |
| $Sr_{1-x}Gd_xTiO_3$<br><br>X = 0 to 0.12 | 1375 | 40 | 5 | 100 K/min in Ar flow | ZT = 0.37 at 1106K where,<br><br>x=0.1 | [66] |
| $Sr_{1-x}La_xTiO_3$,<br><br>x = 0:08 | 1240-<br><br>1390 | 34 | 15 | 30 K/min in vacuum | Relative density 96.27 – 97.55 %<br><br>$zT$ = 0.16 at 1005K | [44] |
| $Sr_{0.92}La_{0.08}TiO_3$ | 1573 | 34 | 30 | in vacuum | $zT$ = 0.22 at 800 K | [67] |

### 3.1.4 Spark Plasma Sintering Conditions Optimization

The calcinated nano scale porous powder has been packed into a graphite die (12mm and 20mm diameter) with protecting graphite foil for spark plasma sintering. The sintering process has been carried out under vacuum condition ($10^{-3}$ bar). Different parameters of SPS like sintering temperature, pressure and sintering time have been optimized to prepare bulk sample with high density.

At first, the samples have been heated at 1173K under a uniaxial pressure of 40 MPa for different sintering time. The temperature and pressure have been increased with a rate of 25K per min and 10 MPa per minute, respectively. The relative density of samples is listed in Table 3.2. The density of samples increases with sintering time, however further improvement is needed for thermoelectric application.

Table 3.2 Relative density of bulk samples sintered with different sintering time

| **Sintering Time (min)** | **Thickness (mm)** | **Weight (g)** | **Density (g/cm$^3$)** | **Relative Density (%)** |
|---|---|---|---|---|
| 5 | 0.8 | 0.258 | 2.85 | 55.66 |
| 8 | 0.75 | 0.277 | 3.27 | 63.87 |
| 15 | 0.6 | 0.240 | 3.54 | 69 |
| 30 | 0.65 | 0.290 | 3.94 | 76.95 |

Secondly, the sintering time and pressure have been increased up to 1423 K and 60 MPa, respectively. The holding time has been kept fixed to 15 min, since short sintering time is better to prevent grain growth and to retain nanostructure. The relative density of ~ 90 % has been achieved at 1423K with 60MPa pressure and 15 min holding or sintering time. Temperature and pressure profile during spark plasma sintering process along with other parameters like punch position, vacuum level of the chamber, Applied DC current and voltage are shown in Fig 3.3.

Table 3.3 Relative density of bulk samples sintered at different temperatures and pressures

| **Spark Plasma Sintering Conditions** | | | **Density ($g/cm^3$)** | **Relative density (%)** |
|---|---|---|---|---|
| **Temperature (K)** | **Pressure (MPa)** | **Holding time (min)** | | |
| 1173 | 40 | 15 | 3.54 | 69 |
| | 50 | | 3.94 | 76.9 |
| 1273 | 50 | | 4.22 | 82.4 |
| 1323 | | | 4.44 | 86.7 |
| 1323 | 60 | | 4.57 | 89.2 |
| 1423 | | | 4.60 | 89.8 |

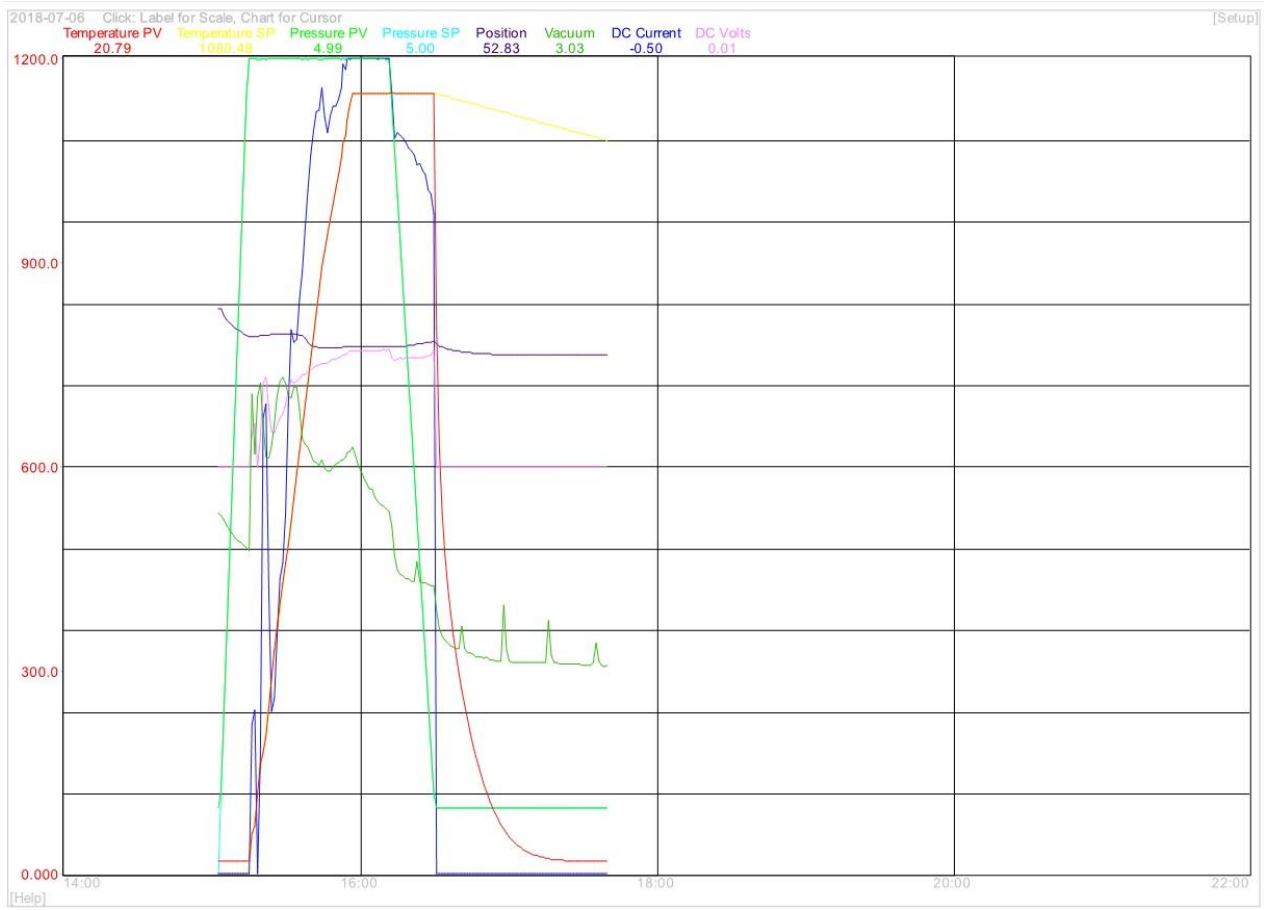


Fig. 3.3 Temperature and pressure profile during the spark plasma sintering process of samples along with other parameters like punch position, vacuum level of the chamber, Applied DC current and voltage.

### 3.1.5 Sample Polishing and Cutting

The bulk sample is polished by the Struers Rotopol grinder to remove the graphite foil stick on the surface of the sample. And then the bulk sample is cut into rectangular and circular shape by using the Struers Accutom-50 for measurement.

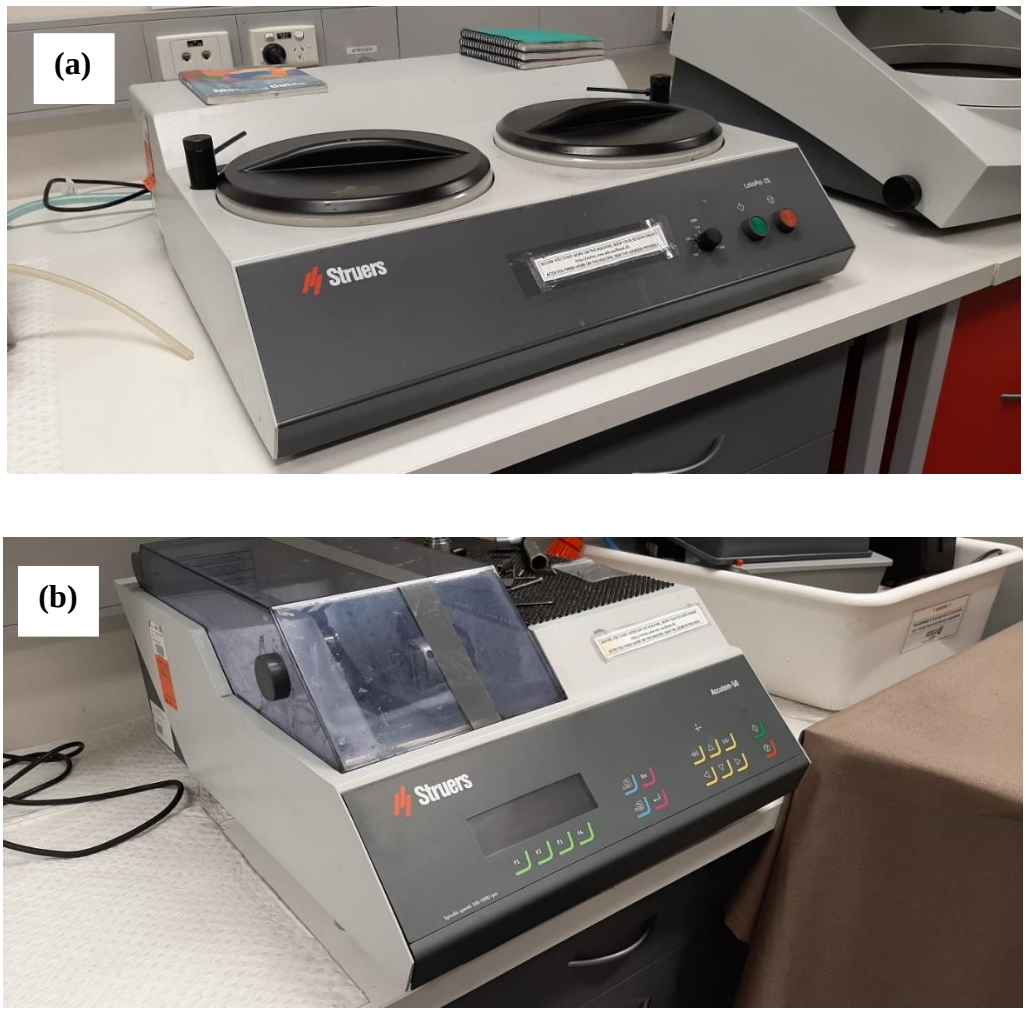


Fig. 3.4 (a) The sample polishing machine (Rotolop by Struers), (b) The cutting instrument (Accutom 50 by Struers)

## 3.2 Sample Characterization

### 3.2.1 X-ray Diffraction (XRD) Analysis

Crystallography phase of material, presence of secondary phase, crystallinity, peak shifting and change in lattice parameter due to substitutional doping has been examined by X-ray powder diffraction (XRD) analysis. The X-ray diffraction analysis is based on the Bragg's law,

$$n\lambda = 2\,d\sin\theta \qquad (3.1)$$

Where, $\lambda$ is the wavelength of incident x-ray, $\theta$ is the diffraction angle, and d is the spacing between layers of atoms. The room temperature powder XRD patterns were determined by the X-ray diffractometry (Cu Kα, GBC MMA, $\lambda$ = 1.5418 Å). XRD patterns were measured with a step size of 0.02° and speed of 2° per min from $10^o$ to $80^o$.

The crystallite size of samples was also calculated from the XRD data using the Scherrer's formula,

$$D_p = K\lambda/(B\ cos\theta)$$

Where, $D_p$ is the average crystallite size (nm), $K$ is Scherrer constant, $\lambda$ is the x-ray wavelength, $B$ is the FWHM (Full Width at Half Maximum) of XRD peak and $\theta$ is the XRD peak position, one half of $2\theta$.

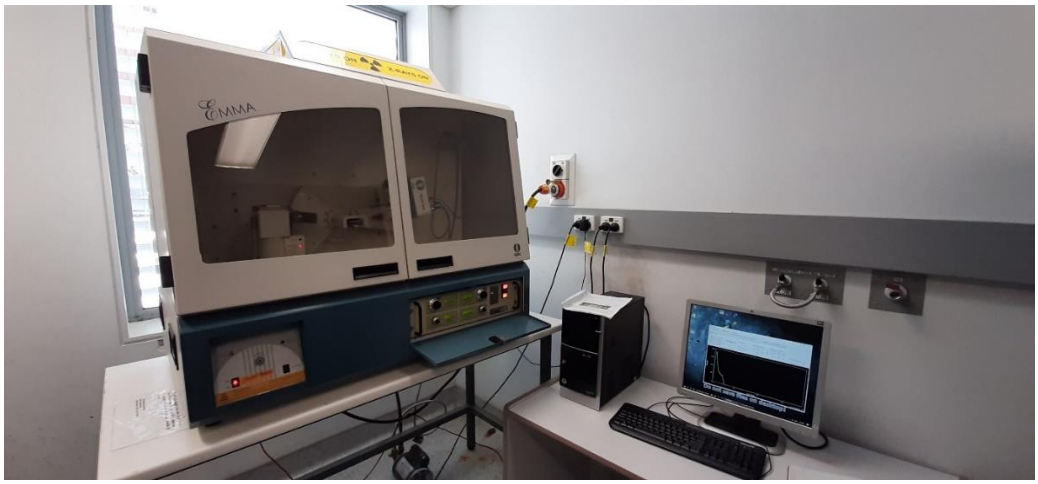


Fig. 3.5 X-ray powder diffraction (XRD) analysis instrument

### 3.2.2 Scanning Electron Microscopy (SEM) Analysis

The surface morphology, grain sizes, nanostructure and element analysis were done by the field emission scanning electron microscopy (FESEM) instrument manufactured by the JEOL (JEOL JSM 7500FA). The maximum magnification capacity of the machine is 1,000,000X with resolution down to 1nm. The freshly fractured samples were mounted on the sample holder using conducting carbon tape and samples were coated with platinum (15 nm) to improve the electrical conductivity. The excitation voltage, current, probe current and working distance between electron gun and sample were adjusted accordingly to capture secondary electron (SE) scanning electron microscopy (SEM) image. The secondary electron images were useful to understand surface topography of samples. The elemental composition and distribution in the samples was also done by the energy dispersive spectroscopy (EDS) analysis using the same instrument.

Fig. 3.6 Field emission scanning electron microscope (FESEM) by JEOL (JEOL JSM 7500FA)

### 3.2.3 Transmission Electron Microscopy (TEM) Analysis

In transmission electron microscope (TEM), a high energy beam of electrons is transmitted through the ultrathin (less then 100nm) specimen to from atomic resolution image.

The JEOL JEM-ARM200F is a 200kV probe corrected scanning transmission electron microscope (STEM). It has resolution of <0.08nm and <0.14 nm at 200kV and 80kV, respectively. Its silicon drift detector (SDD) has been used for element mapping at atomic level to confirm the substitutional doping in crystal structure.

The JEOL JEM2011 is a 200kV conventional Lanthanum Hexaboride (LaB6) cathode TEM with resolution of 0.16 nm. It has been used to observe the crystal fringes, grain boundaries, and nanoscale pores within crystal structure.

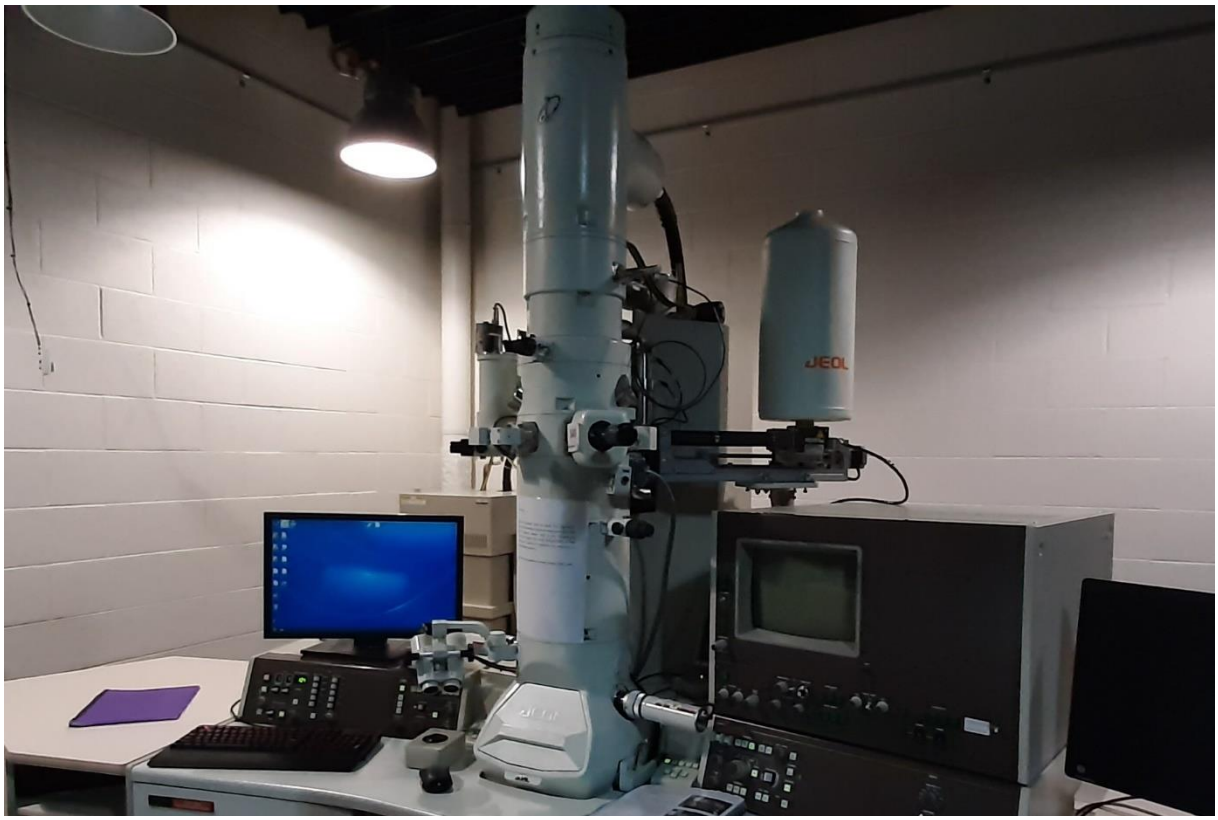


Fig. 3.7 Transmission electron microscopy (TEM) by JEOL (JEM-ARM200F)

### 3.2.4 X-ray Photoelectron Spectroscopy (XPS) Analysis

In X-ray photoelectron spectroscopy (XPS) analysis, surface of the specimen is irradiated with X-ray beam and kinetic energy of electrons that are escaped from the surface (1-10 nm) is measured simultaneously. A photoelectron spectrum is plotted by counting number of escaped electrons over a range of kinetic energies. The intensities and corresponding energies of peaks appeared in the spectrum identify and quantify surface elements. The XPS can also measure the elemental composition, chemical state and electronic state of the elements which are present in the material.

### 3.2.5 Brunauer-Emmett-Teller (BET) and Barrett-Joyner-Halenda (BJH) Analysis

Brunauer-Emmett_Teller (BET) analysis is used to measure the surface area of nanomaterials. The specific surface area ($m^2/g$) of nanoscale porous materials have been evaluated by measuring the isotherm absorption and desorption of nitrogen gas plotted against relative pressure. The measured specific surface area helps to identify the presence of porosity in the material[68]. Barret-Joyner_Halenda (BJH) analysis is used to estimate the pore size distribution in the materials using isotherm absorption-desorption of nitrogen gas.

The average pore size distribution can be identified depending on type of absorption-desorption isotherm. The type I isotherms have microporous structure which means average pore diameter is less than 2nm. Materials with macro porous structure are type II isotherms with average pore diameter greater than 50 nm. The average pore diameter between 2-50 nm indicates mesoporous structure which is type IV isotherm.

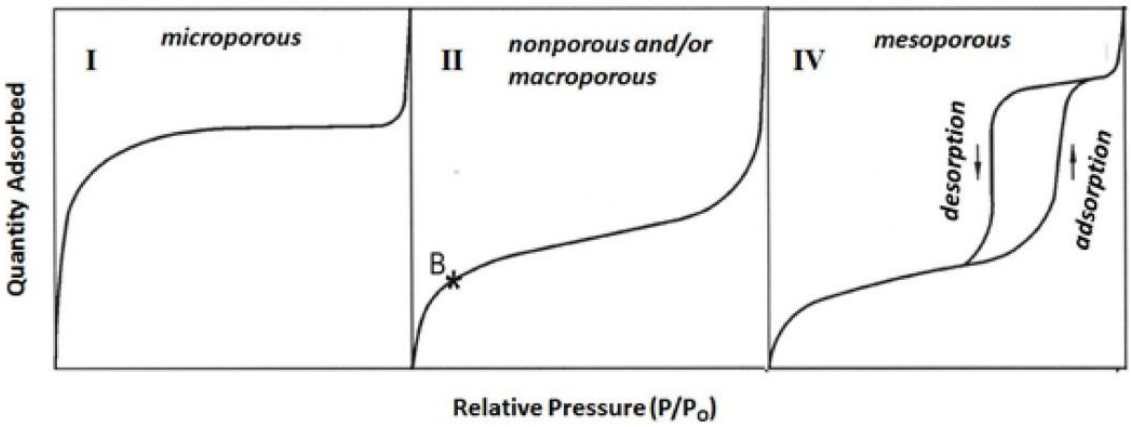


Fig. 3.8 Determination of the average porosity size, and pore structures depending on adsorption-desorption isotherm type[69]

3.2.6 Electrical Conductivity and Seebeck Coefficient Measurement

The electrical conductivity and Seebeck coefficient are measured using the Ozawa 2001i instrument and the power factor is calculated from the measured values. The four prove resistance measurement technique is used to measure the electrical conductivity of samples with temperature. The Seebeck coefficient is measured from the slope of the voltage across the sample with respect to the temperature different between tow ends of the sample.

Fig. 3.9 The electrical conductivity, Seebeck coefficient and Power factor measurement instrument ( Ozawa 2001i )

### 3.2.7 Specific Heat Capacity Measurement

The specific heat of the samples has been measured using the differential scanning calorimetry (DSC) technique. The instrument is manufactured by the Netzsch and model number is DSC 204 F1. In this technique, the difference in the heat required to increase the temperature of a sample and reference sample is measured as a function of temperature. The reference sample should have a well-defined specific heat over the range of temperature to be measured.


Fig. 3.10 Differential scanning calorimetry (DSC) instrument

### 3.2.8 Thermal Diffusivity Measurement

The thermal diffusivity is the measurement of rate of transfer of heat of a material from hot to cold end. The laser flash method is used to measure the thermal diffusivity of materials. In this method, a laser source heats one side of a plane-parallel sample and time required to temperature rise on opposite side of the sample is measured. The higher thermal diffusivity of the material, the faster the temperature rise on the opposite side.

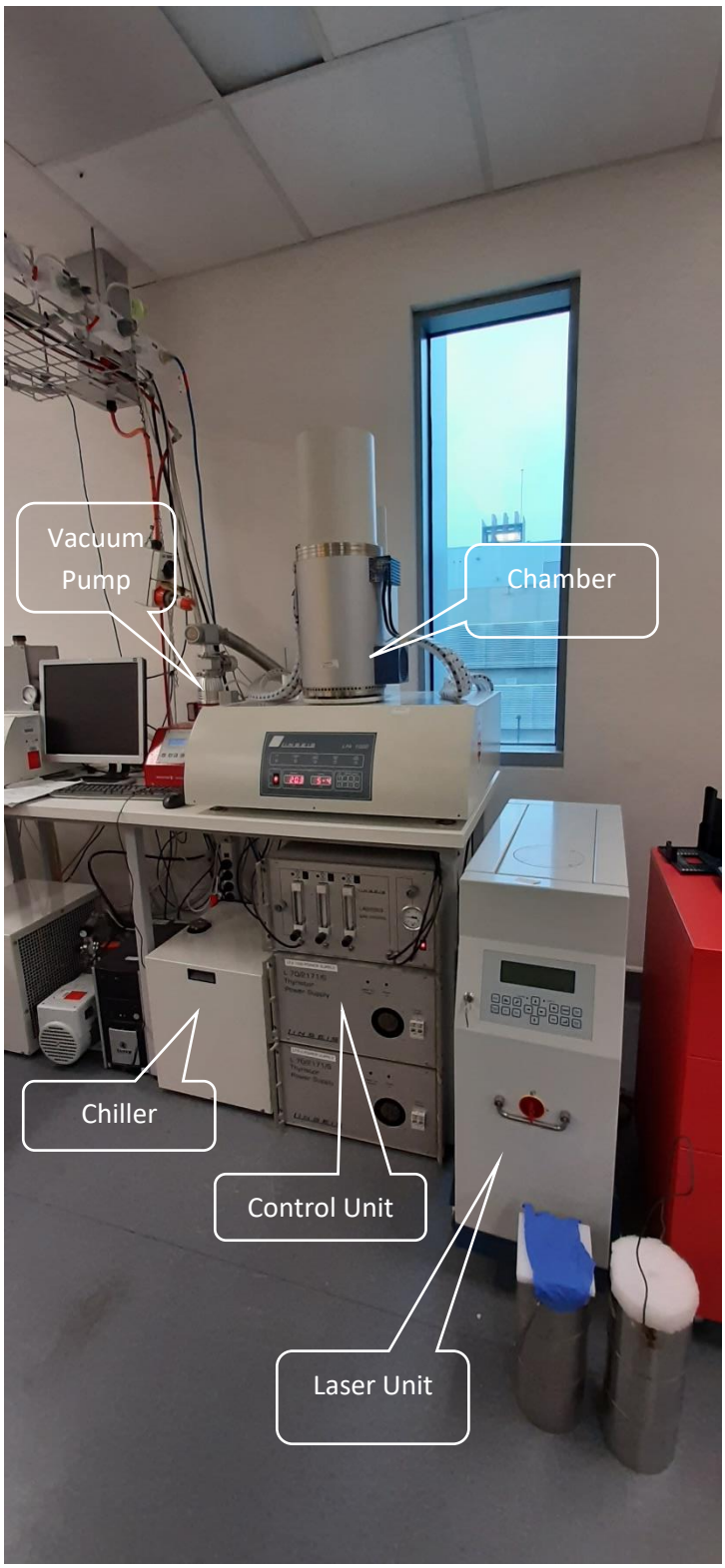


Fig. 3.11 Main components of Laser flash analysis (LFA) instrument

## 3.3 Density Functional Theory (DFT) Calculation

The theoretical analysis of electron band structure and density of state (DOS) of undoped and different atomic percentage of La doped $SrTiO_3$ and $BaTiO_3$ systems were done by the density functional theory (DFT) calculation. The calculation shows how the band structure and density of state of electron change with electron doping into $SrTiO_3$ and $BaTiO_3$ system.

First principle calculations were performed using density functional theory[70-71] (DFT) implemented by the CASTEP package[72]. The exchange correlation function used to describe the exchange-correlation interaction was the General Gradient Approximation (GGA) with the Perdew–Burke–Ernzerhof (PBE)[73]. Structures were optimized using the Broyden–Fletcher–Goldfarb–Shanno algorithm BGFS[74] with a 4×4×4 K-point set and cutoff energy of 630 eV. The atomic positions and cell vectors are relaxed until the energy, maximum force and maximum displacement were less than $5.0 \times 10^{-6}$eV/atom, 0.01eV/Å, and $5.0 \times 10^{-4}$ , respectively.

# 4. Enhancement of Thermoelectric Properties of La-doped $SrTiO_3$ Bulk by Introducing Nanoscale Porosity

## 4.1 Introduction

More than 60 percent of total energy produced worldwide is being wasted as heat. This leftover heat can be utilized for producing necessary electrical energy by thermoelectric (TE) materials [1-2, 4-5]. The full potential of TE materials can be utilized by using them with other energy conversion technologies [6]. Thermoelectric performance of a material is assessed by the dimensionless figure of merit, $zT = \frac{S^2\sigma T}{\kappa}$, where, *S, σ, T*, and *κ* are the thermopower (Seebeck coefficient, μV/K), the electrical conductivity (S/m), the absolute temperature (K), and the thermal conductivity (W/mK), respectively [14-15, 18, 75]. The term $S^2\sigma$ is called the PF of the Thermoelectric material as well. For power generation application, it is even more important for a thermoelectric material to have improved power factor than to have a high efficiency, since most ubiquitous heat sources are free [16].

The relationship of the Seebeck coefficient to carrier concentration for doped semiconductor can be expressed as $S = \frac{8\pi^2 k_B^2}{3eh^2}\, m^* T \left(\frac{\pi}{3n}\right)^{2/3}$, where, $k_B$ stands for Boltzmann constant, *e* for electron charge, $h$ refers to Planck's constant, $m^*$ accounts to effective mass of the carrier, $T$ is the absolute temperature, and $n$ the carrier concentration [18]. The electrical conductivity varies proportionally with carrier concentration and carrier mobility, $\sigma = n\, e\, \mu$, where $\mu$ is the carrier mobility. The over-all thermal conductivity of a material is the product of the thermal diffusivity, the heat capacity, and the material density, $\kappa = \alpha\, C_p\, \rho$, Where, $\alpha, C_p$, and $\rho$ are the thermal diffusivity, the heat capacity at constant pressure, and the material density, respectively

[12]. Thermal conductivity $\kappa$ has two components: $\kappa_{el}$ is the thermal conductivity from movement of the electrons and the holes, and $\kappa_{ph}$ is the contribution from the movement of phonons through the lattice, $\kappa = \kappa_{ph} + \kappa_{el}$ [15]. From Wiedemann-Franz law, it is perceivable that an increase in $\kappa_{el}$ with increasing electrical conductivity, $\sigma$, and temperature, $T$. $\kappa_{el} = LT\sigma$, where $L$ denotes the Lorenz number. Normally, $L$ is treated as a universal factor with the value of $2.44 \times 10^{-8}\ \mathrm{W\Omega/K^2}$ for a degenerate semiconductor [15]. However, there is a significant deviation in the Lorenz number of non-degenerate semiconductors, where $L$ converges to $1.5 \times 10^{-8}\ \mathrm{W\Omega/K^2}$ [20]. Since the electronic thermal conductivity $\kappa_{el}$ is related to the electrical conductivity and high electrical conductivity is a prerequisite for a TE material, the lattice thermal conductivity $\kappa_{ph}$ has to be reduced to lower the overall thermal conductivity.

The $\kappa_{ph}$ can be characterized by, $\kappa_{ph} = \frac{1}{3} C_v V l$, where the heat capacity ($C_v$) and the phonon velocity ($V$) are constant, so the $\kappa_{ph}$ mainly relies on the phonon mean free path (MFP) ($l$) [5]. It was reported that nanoscopic pores in silicon thin film can suppress the lattice thermal conductivity to the amorphous limit[76]. A modelling study on nano-porous SiGe suggested that enhancement of the Seebeck coefficient by scattering only low-energy electrons and decrease in the lattice thermal conductivity can take place because of nanoscale porosity in the material, but high sample density is essential to prevent deterioration in the electrical conductivity[22]. The effects of mesoporous structure on the TE properties of doped $SrTiO_3$ thin film were investigated. The mesoporous structure suppresses the thermal conductivity and improves the Seebeck coefficient because of phonon and carrier scattering. The incorporation of Brij-S10 surfactant into doped $SrTiO_3$ film increased the $zT$ value [30-31].

Conventional Thermoelectric materials for example $Bi_2Te_3$, PbTe and $Cu_2Se$ exhibit high thermoelectric performance, but these materials have some limitations such as poor lifetime at high temperature in air, limited sources, and high toxicity. On the other hand, metal oxide based TE materials have high lifetime at high temperature, low-cost, non-toxic and have minimal impact on environment[10]. Some *p*-type metal oxide-based TE materials such as $NaCo_2O_4$, layer-structured cobalt oxide, and BiSeCuO exhibit excellent TE properties. The highest value of figure of merit reaches unity ($zT$ = 1.4 ) for $Bi_{0.875}Ba_{0.125}CuSeO$ [11]. As compared to the *p*-type oxides, *n*-type oxide materials have lower thermoelectric performance. To fabricate a TE module based on oxide materials, the $zT$ of *n*-type oxides should be improved to the level of *p*-type materials.

Strontium titanate (denoted as $SrTiO_3$) is a well-known *n*-type thermoelectric material with the cubic perovskite $ABO_3$ crystal structure having the lattice parameter of 0.3905 nm. The melting temperature of $SrTiO_3$ is 2080$^oC$ which gives it chemical as well as thermal stability at high temperature. The lattice thermal conductivity of $SrTiO_3$ is high, 12 W/mK at room temperature[12]. $SrTiO_3$ with appropriate stoichiometry is an insulator having a band gap of 3.2 eV. However, the electrical conductivity can be changed from insulating to metallic by substitutional doping of $SrTiO_3$ with $La^{3+}$ or $Nb^{5+}$.

Several methods are available to tune material properties such as chemical doping, pressure, solid state reaction and so on. However, chemical doping seems to be an effective approach to improve the material performance without physical damage of the material [75, 77-80].It was reported that high $zT$ has been achieved for La-doped $SrTiO_3$ by creating a defective perovskite lattice containing A- and O- site vacancies with mixed valence $Ti^{3+}$ and $Ti^{4+}$ on the B-sites [23-

[24]. The effects of spark plasma sintering (SPS) time on thermoelectric properties of Lanthanum doped $SrTiO_3$ was also reported[25]. In another report, La-doped $SrTIO_3$ bulk with nanostructured was synthesised by SPS from chemically synthesized colloidal nanocrystals[26]. It was reported that the addition of nanosized Ag metal particles in $Sr_{0.9}La_{0.1}TiO_3$ causes an increase in the carrier concentration and that the electrical connection is built into Ag particle between the grains. They improve the electrical conductivity and reduce the thermal conductivity[29]. The thermoelectric properties of $Sr_{1-x}La_xTiO_3$ nanoparticle compacts which was fabricated by the hydrothermal process followed by cold pressure were investigated [27]. The morphology of the nanoparticle compacts had abundant interfaces, which effectively reduced phonon's mean free path.

So far, the effect of nanoscale porosity on the TE properties of La-doped $SrTiO_3$ bulks has not been published. Here, it is reported for the first time that nanoscale porosity in a La-doped $SrTiO_3$ bulk sample has a significant impact on its thermoelectric properties. The nanoscale porosity supresses the thermal conductivity and significantly enhances the Seebeck coefficient by the phonon and carrier scattering, respectively. Therefore, there is an overall improvement in the power factor and the $zT$ of La-doped $SrTiO_3$.

## 4.2 Experiment

### 4.2.1 Synthesis of La-doped $SrTiO_3$ Powders with Nanoscale Porosity

First, strontium acetate (0.26 g) and lanthanum acetate hydrate (0.11 g for 20 at% La doping) were dissolved into acetic acid solution (3.0 mL) at 323 K with stirring. After the solution was cooled down to room temperature, titanium butoxide (0.61 g) was further added to it. The commercially available poly (ethylene oxide)-*b*-poly (propylene oxide)-*b*-poly (ethylene oxide) type triblock copolymer, Pluronic F127 ($PEO_{106}PPO_{70}PEO_{106}$), was used as the soft-template. Pluronic F127 in different amounts (200, and 600 mg) was dissolved in ethanol solution (3.0 g) in another beaker. The above two solutions were mixed to prepare the precursor solutions. Then, the precursor solutions were transferred onto filter paper. Finally, the filter papers were calcined for 10 min at 873K to remove the templates (Fig. 4.1).

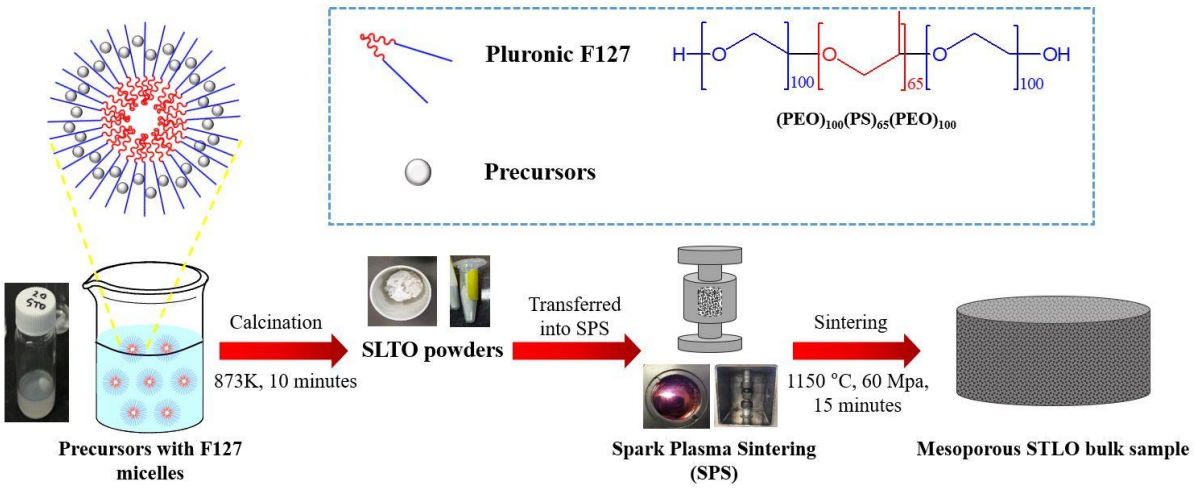


Fig. 4.1 Schematic illustration of fabrication processes of the La-doped SrTiO3 bulk sample with nanoscale porosity using F127 surfactant.

### 4.2.2 Preparation of La-doped $SrTIO_3$ Bulk

In the second stage of fabrication (Fig. 4.1), highly dense bulk samples of 20 mm diameter and around 1.5 mm thick were prepared from the La-doped $SrTiO_3$ calcinated powders by spark plasma sintering (Thermal Technology SPS model $10^{-4}$) for 15 min at 1423 K with 60 MPa pressure in vacuum. Using a cutting machine (Struers Accutom-50), the bulk samples were shaped into rectangular bars and round disks for transport properties measurement. La-doped $SrTIO_3$ samples with different amounts of F127 surfactant were denoted by the amount of surfactant, such as SLTO-*x*F127 ($x$ = 0, 200, and 600).

### 4.2.3 Sample Characterization

The room temperature powder XRD patterns were determined by the X-ray diffractometry (Cu Kα, GBC MMA, $\lambda$ = 1.5418 Å). XRD patterns were measured with a step size of 0.02° and speed of 2° per min from $10^o$ to $80^o$. The morphologies and nanostructures of the powder and bulk samples were studied using field emission scanning electron microscopy (FE-SEM, JEOL 7500). The surface area and porosity of powder samples were inspected by Brunauer-Emmett-Teller (BET) and Barrett-Joyner-Halenda (BJH) analysis of nitrogen absorption-desorption data collected on a Tristar 3020 system (Micrometrics Instrument Corporation) after degassing at $150^oC$ overnight. The $S$ and the $\sigma$ were measured from room temperature to 968 K under vacuum using the instrument, Ozawa RZ2001i. The thermal diffusivity was measured under vacuum conditions using the instrument, LINSEIS LFA 1000, and the specific heat was measured under argon atmosphere by the instrument, DSC-204F1 Phoenix. The weight and dimensions of a rectangular sample were used to determine the sample density. The results of the samples are confirmed by repeating all the measurements for several times.

4.3 Result and discussion

The XRD patterns of La-doped $SrTiO_3$ calcined powders with different amounts of F127 surfactant are shown with respect to undoped $SrTiO_3$ in Fig. 4.2. The XRD patterns match with Joint Committee on Powder Diffraction Standards (JCPDS) card number 00-001-1018, which confirms that the main phase is strontium titanium oxide ($SrTiO_3$). There are some impurity phases such as $TiO_2$ and $SrTi_{12}O_{19}$ [81] with peaks in the $2\theta$ range of $25^o - 35^o$ in the XRD patterns.

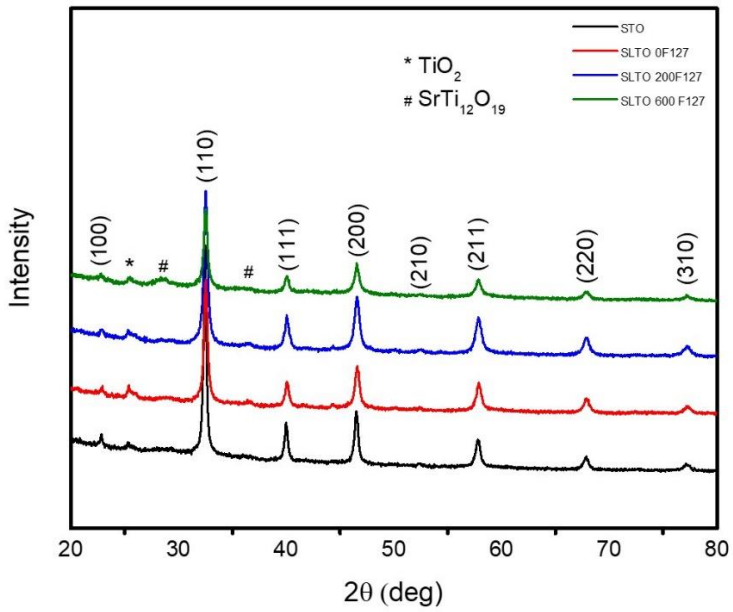


Fig. 4.2 XRD patterns of La-doped SrTiO3 calcinated powders with different amounts of F127 surfactant with reference to undoped SrTiO3.

Fig. 4.3 (a and b) shows the nitrogen absorption/desorption isotherms and pore size distributions of La-doped $SrTiO_3$ calcinated powder with different amounts of F127 surfactant. It is clear from the figures that absorption/desorption of nitrogen gas and pore volume increase with the amount of F127 surfactant, which indicates that the number of pores increases in the sample with the amount of surfactant. The average pore size is 8 to 9 nm in both the samples, which is

in the range of mesoscale (2 to 50 nm) porosity (Table 4.1), since the diameter of a pore depends on the size of the micelle formed by the surfactant. The specific surface area and pore volume also increase with the amount of surfactant, which is also an indication that the pore number increases with the amount of surfactant (Table 4.1).

Table 4.1 Specific surface area, pore volume, and average pore width of samples with different amounts of F127 surfactant

| **Sample** | **Specific Surface Area ($m^2/g$)** | **Pore Volume ($cm^3/g$)** | **Average Pore Size (nm)** |
|---|---|---|---|
| SLTO 200F127 | 31.35 | 0.143 | 8.75 |
| SLTO 600F127 | 56.81 | 0.231 | 8.41 |

SEM images of the La-doped $SrTiO_3$ calcinated powders with different amounts of F127 surfactant also reveal that the number of pores increases with an increasing amount of F127 Surfactant. The SLTO 0F127 sample (Fig. 4.3 (c)) has no porosity because it has zero amount of surfactant. There are a few mesoscale pores in the SLTO 200F127 powder (Fig. 4.3(d)). The SLTO 600F127 powder has more mesopores compared to the other samples (Fig. 4.3(e)). The SEM images also show that some pores have become agglomerated, which is because of the high calcination temperature[46].

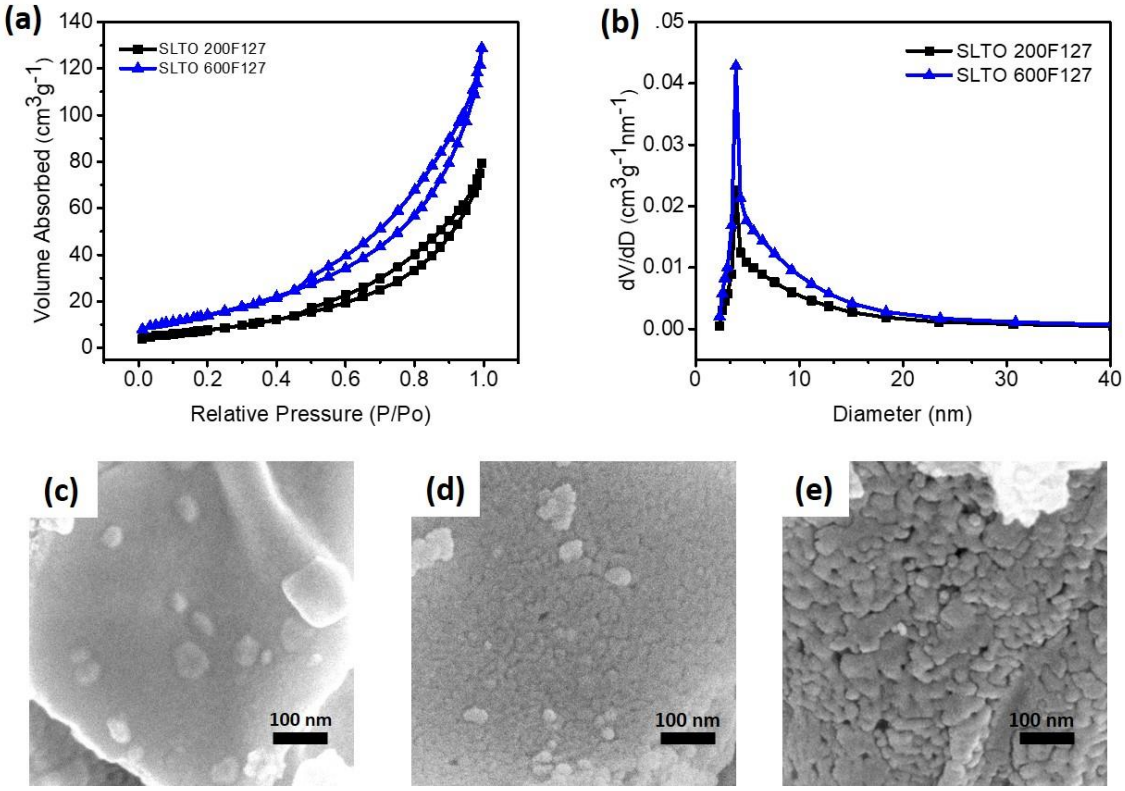


Fig. 4.3 (a) Nitrogen absorption/desorption isotherms, and (b) pore size distributions of La-doped SrTiO3 calcinated powders with different amounts of F127 surfactant. SEM images of La-doped SrTiO3 calcinated powders with different amounts of F127 surfactant (c) SLTO 0F127, (d) SLTO 200F127 and (e) SLTO 600F127

Fig. 4.4 (a) shows the cubic perovskite crystal structure of $SrTiO_3$ and Fig. 4.4 (b) shows the powder XRD patterns of the La-doped $SrTiO_3$ bulks with different amounts of F127 in comparison with undoped $SrTiO_3$. There is no impurity phase that is detectable in the XRD patterns. The enlarged (200) and (211) diffraction peaks (Fig. 4.4 (c and d)) are clearly shifted to a higher angle. This indicates that $Sr^{2+}$ ions has been successfully replaced by $La^{3+}$ ions on A sites in the crystal lattice of $SrTiO_3$ and it is because of the La ion has a fixed 3+ valence and La ion has smaller ionic radius of 1.36 Å than that of $Sr^{2+}$ (1.44 Å) [82]. In Fig. 4.4 (c and d), the peaks are $K\alpha_1$ and $K\alpha_2$ doublets rather than separate peaks[83]. The extracted lattice parameters from the XRD patterns also show that the shrinkage in lattice is happened by the La

doping. The shrinkage in lattice from 0.3901 nm for undoped $SrTiO_3$ to 0.389 for 20 at% La doping. The lattice parameter of samples is given in Table 4.2.

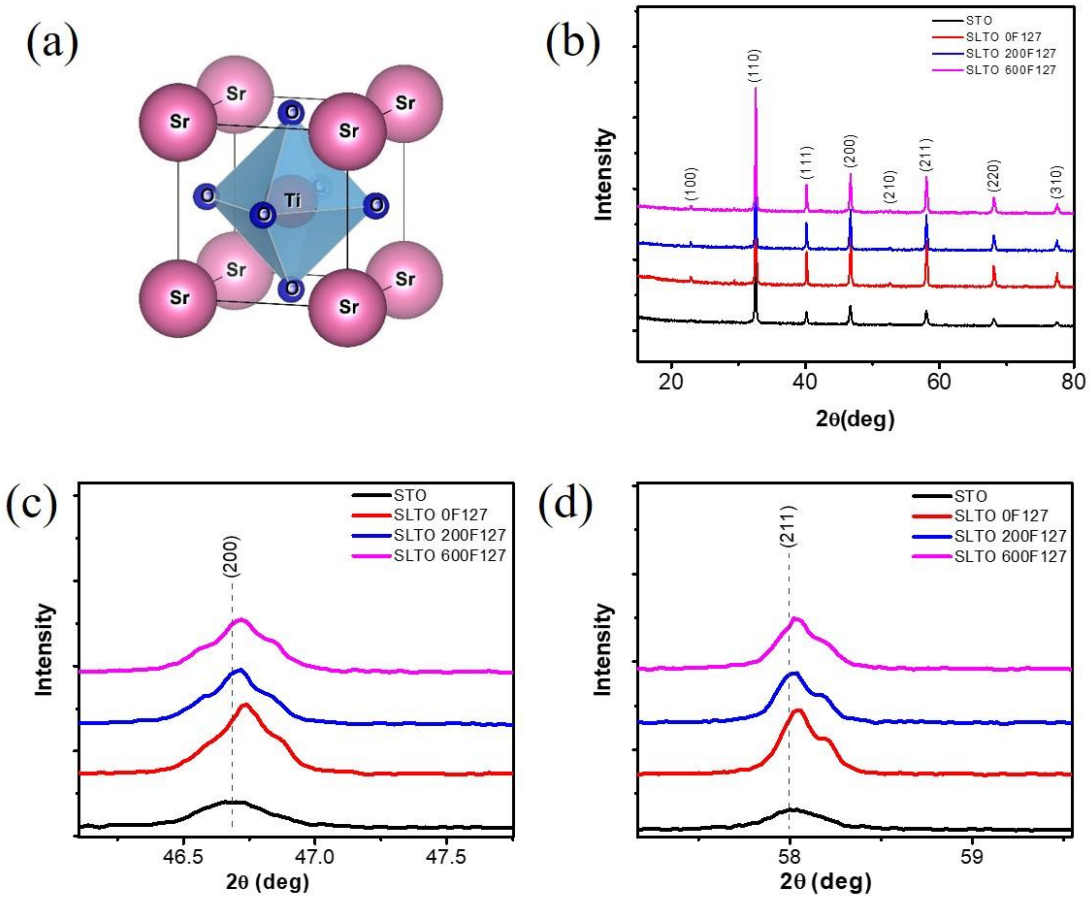


Fig. 4.4 (a) Cubic perovskite crystal structure of SrTiO3, (b) XRD patterns of La-doped SrTiO3 bulk samples with different amounts of F127 surfactant in comparison with undoped SrTiO3. (c) Enlarged (200) diffraction peak, (d) Enlarged (211) diffraction pe[26].

Table 4.2 Lattice parameter of samples with different amount of F127 surfactant

| **Sample** | **Lattice Parameter (nm)** |
|---|---|
| STO | 0.3901 |
| SLTO 0F127 | 0.3891 |
| SLTO 200F127 | 0.3894 |
| SLTO 600F127 | 0.3889 |

The density of the SLTO-F127 samples is listed in Table 4.3. The density of samples decreases slightly with increasing amounts of F127 surfactant in the sample. Since all the samples are sintered under the same sintering conditions, the reduction in density is an indication of the change in porosity inside the samples.

Table 4.3 Density and relative density of samples with different amounts of F127 surfactant

| **Sample** | **Amount of F127 (mg)** | **Density ($g/cm^3$)** | **Relative Density (%)** |
|---|---|---|---|
| SLTO 0F127 | 0 | 4.81 | 93.95 |
| SLTO 200F127 | 200 | 4.66 | 91.02 |
| SLTO 600F127 | 600 | 4.51 | 88.09 |

The SEM cross-sectional images of the bulk samples (Fig. 4.5) also reveal that number and size of the pores inside the samples change with the amount of F127 surfactant. The SLTO 0F127 sample (Fig. 4.5 (a and d)) has no porosity, and the grains have become agglomerated. In Fig. 4.5 (b and e), the SLTO 200F127 sample has few nanoscale porosities in between of grains. In the SLTO 600F127 sample, there are more mesopores in between of grains compare to the sample SLTO 200F127, as shown in Fig. 4.5 (c and f). It can be also observed from the Fig 4.5 that the particle size increases with amount of surfactant in the sample. Increase in particle size could be the reason to keep the electrical conductivity unchanged but on the other hand the porosities in between of particles are responsible for phonon scattering which helps to reduce the phonon thermal conductivity.

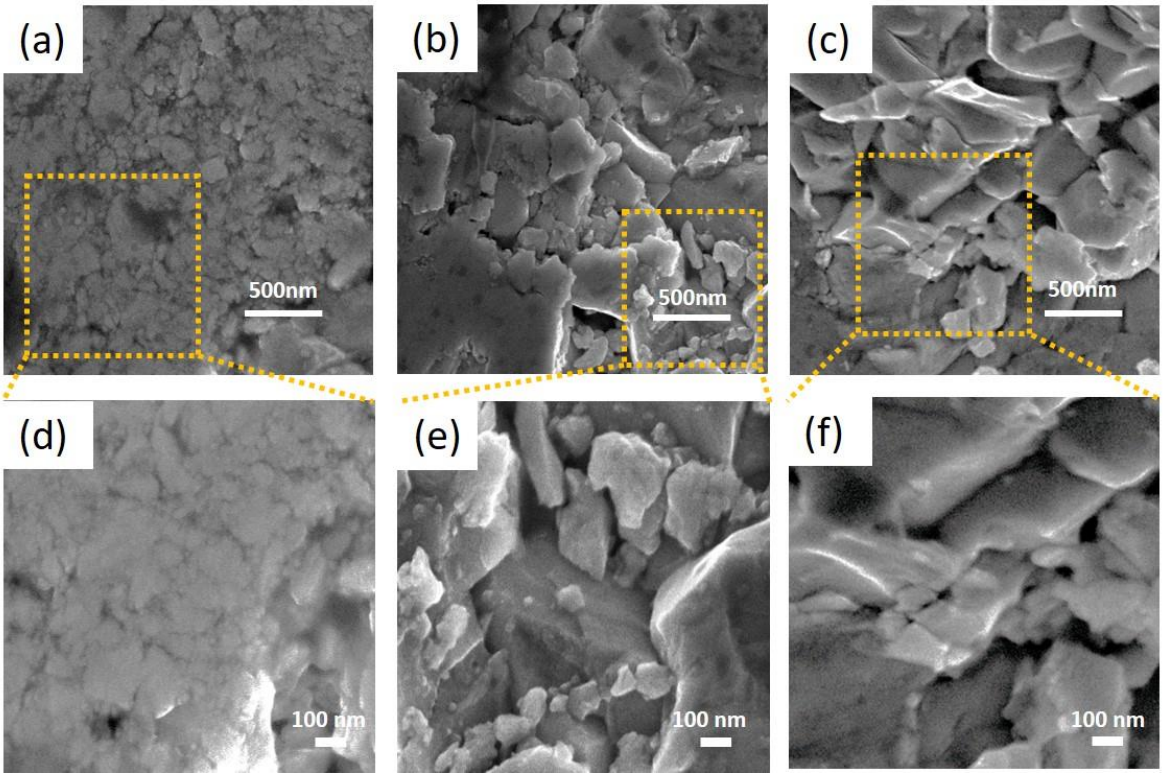


Fig. 4.5 SEM cross-sectional images of bulk SrTiO3 samples with different porosity: a) SLTO 0F127, b) SLTO 200F127, c) SLTO 600F127; High resolution image of the selected region d) SLTO 0F127; e) SLTO 200F127, f) SLTO 600F127.

The dependence on temperature of $\sigma$, $S$, $PF$, and $\kappa$ for the La-doped $SrTiO_3$ samples with different amounts of F127 is shown in Fig. 4.6. The undoped $SrTiO_3$ is found insulator, however, its electrical conductivity has been improved with 20 at% La doping in each sample and this result is comparable with the previously reported results [23-24, 26, 44]. The electrical conductivity, $\sigma$ of all the samples increases initially with temperature up to 647 K (Fig. 4.6 (a)), and then it starts to decrease with temperature afterward. There is no substantial change in $\sigma$ for the samples (Fig. 4.6 (a)) with the different amount of F127 surfactant. The carrier concentration in all the samples is same since doping level is same for all the samples.

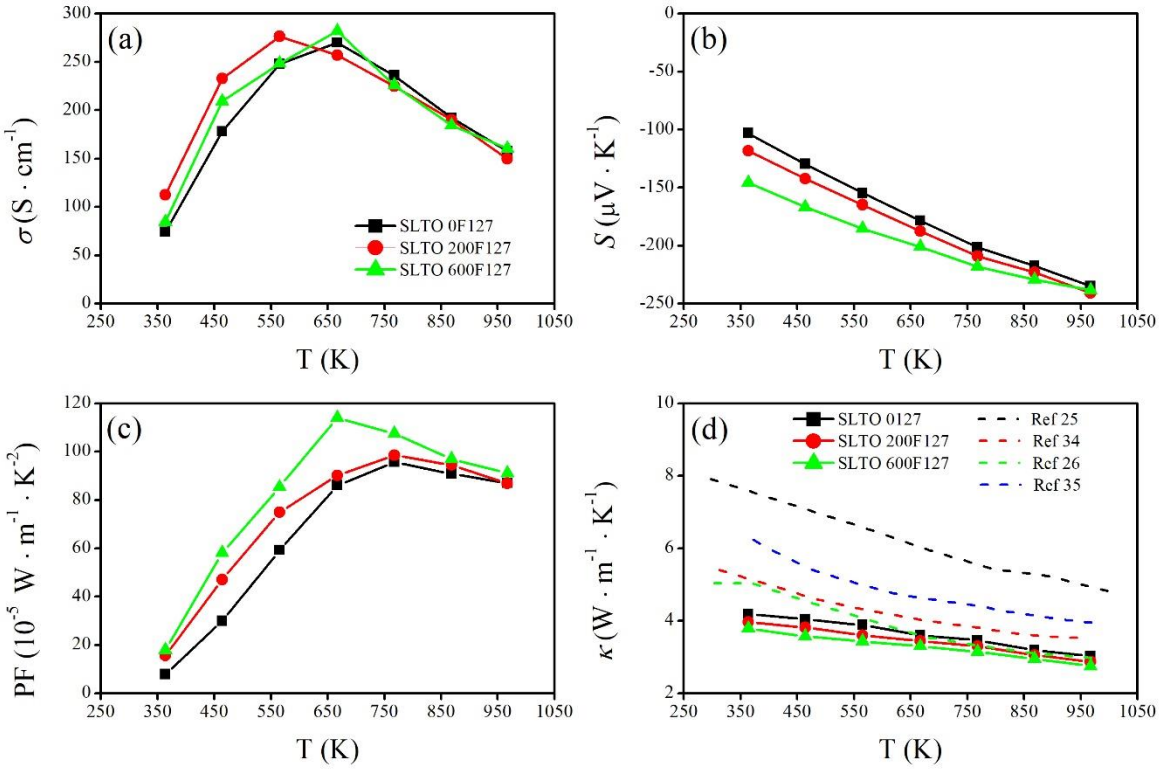


Fig. 4.6 Transport properties of the samples with different F127, (a) the electrical conductivity (σ), (b) the Seebeck coefficient (S), (c) the power factor (PF), and (d) the thermal conductivity (κ) in comparison with previously reported results[25-26, 28, 36].

The Seebeck coefficient, *S* of all the samples is negative, and it increases in magnitude with temperature (Fig. 4.6 (b)). There is a significant improvement in the Seebeck coefficient with increasing amounts of F127 surfactant which could be due to the scattering of charge carriers by the pore. The SLTO 600F127 sample shows a high Seebeck coefficient compared to other samples over a wide scale of temperature. The maximum value of the Seebeck coefficient for this sample is 140 $\mu V \cdot K^{-1}$ at 325 K which is 52% higher than the sample without porosity (SLTO 0F127).

The power factor, *PF* for the samples is presented in Fig. 4.6 (c). Due to the improvement in the Seebeck coefficient, there is a significant improvement in the power factor also. The *PF* of the samples increases with the temperature up to 647 K, where it has its peak value. The SLTO 600F127 sample shows the highest value of the power factor, 1.14 $mW \cdot m^{-1}K^{-2}$ at 647 K, which is 35% higher than the power factor of the sample without porosity (SLTO 0F127).

Fig. 4.6 (d) exhibits the change in the thermal conductivity, $\kappa$ of the samples with temperature. The thermal conductivity of the SLTO 0F127, SLTO 200F127 and SLTO 600F127 is found 3.03, 2.88, and 2.75 W/m K respectively at temperature 967 K. The gradual reduction in thermal conductivity has been observed with increasing amount of surfactant. Moreover, the $\kappa$ of all the samples is found significantly lower than most of the published results[25-26, 28, 36]. The reduction in thermal conductivity over the wide scale of temperature is due to the scattering of phonons by the nanoscale porosity. The electronic thermal conductivity and the phonon thermal conductivity are presented in Fig 4.7 (a and b) respectively. The reduction in total thermal conductivity over the wide scale of temperature is due to the scattering of phonons by the

nanoscale porosity. The Fig 4.6 (b) is the evidence of reduction in $\kappa_{Ph}$ due to the nanoscale porosity.

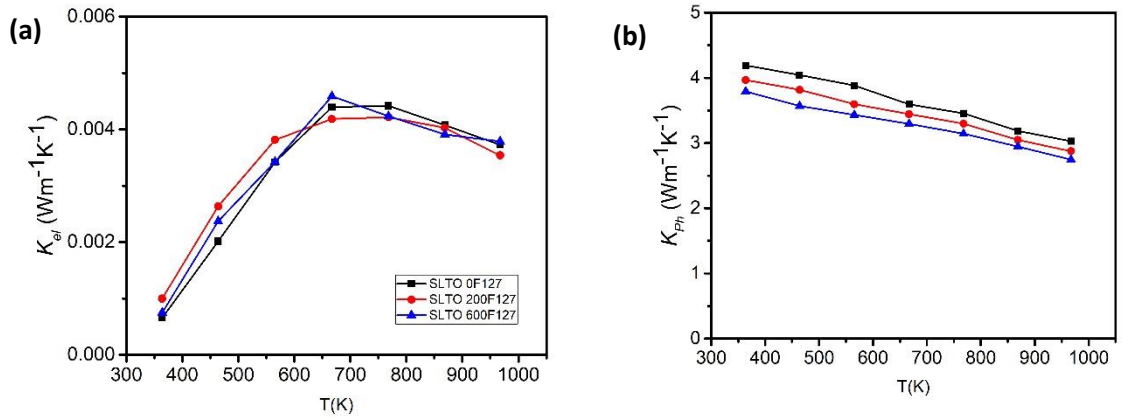


Fig. 4.7 (a) The electronic thermal conductivity and (b) The phonon thermal conductivity of samples with different amount of surfactant F127.

Because of the substantial improvement in the Seebeck coefficient and reduction in the thermal conductivity, there is an overall improvement in the *zT* of the porous samples (SLTO 200F127 and SLTO 600F127) compared to the non-porous sample SLTO 0F127 as shown in Fig. 4.8 (a). There is also a substantial improvement in the *zT* over a wide scale of temperature compare to the previously reported result of 20 at% La doped $SrTiO_3$ [23]. The SLTO 600F127 sample shows the highest value of *zT* of 0.32 at 968 K.

The improvement in *zT* of the SLTO 600F127 in percentage compared to the sample SLTO 0F127 is shown in Fig. 4.8 (b). It is important to mention that the average improvement of *zT* in the SLTO 600F127 is found 62% compared to the SLTO 0F127. The efficiency of samples is calculated according to the literature[84]. The efficiency of samples SLTO 0F127 and SLTO 600F127 compare to the reported results is shown in Fig. 4.8 (c)[23]. It is found that the efficiency for the SLTO 600F127 is >5% at 968 K, which is around 26% higher than the SLTO 0F127

sample. The compatibility factor is important to cascade a thermoelectric material with another one to fabricate segmented thermoelectric device. Two thermoelectric materials with close compatibility factor are suitable for cascading. The compatibility factor of samples (SLTO 0F127, SLTO 200F127, SLTO 600F127) for segmented thermoelectric generator is calculated based on the literature[85] as shown in Fig. 4.8 (d). It could help to find the suitable thermoelectric material for cascading with La-doped $SrTiO_3$.

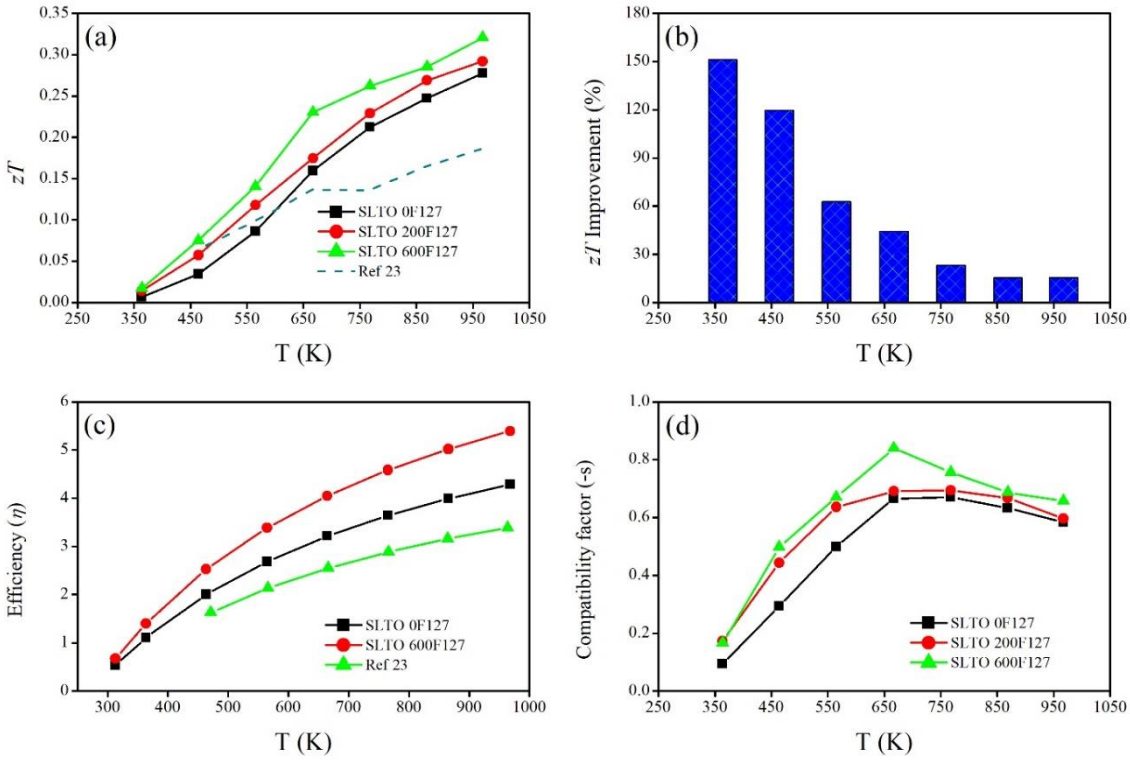


Fig. 4.8 (a) zT in comparison with published result23, (b) the improvement in zT of the sample SLTO 600F127, (c) the efficiency of samples in comparison to the published result23, and (d) the compatibility factor (-S) of the samples.

## 4.4 Conclusion

La-doped $SrTiO_3$ bulk samples with F127 surfactant in different amounts have been fabricated for the first time and investigated successfully. The experiments reveal that there is an impact of nanoscale porosity on the transport properties of La-doped $SrTiO_3$. It has been observed that the Seebeck coefficient increases, while the thermal conductivity is reduced substantially by introducing porosity into the bulk sample because of the carrier and phonon scattering by the nanoscale pores. Therefore, there is an overall enhancement in the *PF* and the *zT*. The sample, SLTO 600F127, exhibits the highest value of the power factor, 1.14 $mW \cdot m^{-1}K^{-2}$ at 647 K, which is 35% higher than for the sample without porosity (SLTO 0F127). The same sample (SLTO 600F127) also exhibits the maximum value of the *zT* is 0.32 at 968 K with an average enhancement of 62% in *zT* in comparison to the sample without porosity (SLTO 0F127).

The result presented in this chapter has been published in the journal Royal Society Open Science by me as a first author. Sheik Md. Kazi Nazrul Islam, Ridwone Hossain and Motasim Billah helped me to conduct experiments and to result analysis. Jeonghun Kim and Minjun Kim contributed to manuscript writing. Md. Shahriar A. Hossain, Yusuke Yamauchi and Xiaolin Wang supervised and revised the manuscript.

"Enhancement of thermoelectric properties of La-doped $SrTiO_3$ bulk by introducing nanoscale porosity"; Al Jumlat Ahmed, Sheik Md. Kazi Nazrul Islam, Ridwone Hossain, Jeonghun Kim, Minjun Kim, Motasim Billah, Md. Shahriar A. Hossain, Yusuke Yamauchi and Xiaolin Wang; https://doi.org/10.1098/rsos.190870; Published:23 October 2019.

# 5. Significant Improvement in Electrical Conductivity and Figure-of-merit of Nanostructured Porous $SrTiO_3$ by La Doping Optimization

## 5.1 Introduction

Renewable energy is the answer to today's energy challenges of clean and efficient energy sources to replace the conventional fossil fuels. The thermal energy which is being wasted enormously from different sources can be directly converted into valuable electrical energy using thermoelectric (TE) device [1-4]. The TE device can be integrated with different energy sources, for example: exhaust pipe of vehicle, industrial boiler, thermal power plant, cooking stove even with the human body to convert thermal energy into electricity [6]. The TE device is made of n-type and p-type semiconducting materials connected electrically in series and thermally in parallel. The performance of energy conversion of TE materials is assessed by the dimensionless figure of merit, $zT = \frac{S^2\sigma}{\kappa}T$, where, $S$, $\sigma$, $T$, and $\kappa$ are the Seebeck coefficient, the electrical conductivity, the absolute temperature, and the thermal conductivity respectively [14-15, 18, 75]. The term $S^2\sigma$ is called the power factor ($W/mK^2$) of the thermoelectric material which is a measure of electrical power generated for per unit temperature different in per unit length of TE material.

Transition metal oxide based TE materials has some benefits like chemical stability at high temperature, non-toxic, low-cost and environmentally friendly compared to conventional TE

materials, for example, $Bi_2Te_3$, PbTe, and $Cu_2Se$[10]. Strontium titanate ($SrTiO_3$) is a well-known *n*-type TE material but its performance still inferior compared to its counterpart, p-type metal oxide-based TE materials. Copper oxide based p-type material, $Bi_{0.875}Ba_{0.125}CuSeO$ has figure of merit more than unity ( $zT$ =1.4) [11]. The main drawback of $SrTiO_3$ is high lattice thermal conductivity (12 W/mK at room temperature) due to lower atomic mass[12] of elements. Pure $SrTiO_3$ is an insulator with bang gap of 3.2 eV, however its electrical conductivity can be improved to metallic by substitutional electron doping with group III elements mostly La and group V elements mostly Nb at A and B site of the crystal structure respectively or by co-doping on both sites. The electrical conductivity can be also improved by oxygen reduction. The mathematical modelling of La-doped $SrTiO_3$ done by Singh *et al* shows that the $zT$ can reach up to 0.7 at 1400K by optimizing carrier concentration[21]. In practical, different mechanisms together with electron doping have been tried so far to improve the thermoelectric properties of $SrTiO_3$ as summarised in Table 5.1. For instance: A site and O site vacancies with La doping; nanostructured bulk with La doping; different metal like Ag, Fe, Cu inclusion with La and Nb doping; composite of pure and doped $SrTiO_3$; different co-doping like La with Nb, Dy, Y or Ta; mesoporous film of La doped $SrTiO_3$. In our previous work, it was reported for the first time that introducing nano-scale pores into bulk sample of $SrTiO_3$ can improve its Seebeck coefficient and can reduce the thermal conductivity significantly[86].

Table 5.1 Summery of Thermoelectric properties of Doped $SrTiO_3$

| **Doping level** | **Mechanism** | ***zT*** | **Ref** |
|---|---|---|---|
| 12 – 17 at% La | Defective perovskite lattices containing conditions of A- and O- site vacancies with mixed valent $Ti^{3+}$ and $Ti^{4+}$ on the B-site | 0.41 at 973K | [23] [24] |
| 8 at% La | Spark plasma sintering at 1573 K for different holding time. Sample sintered at for 5min shows highest ZT | 0.37 at 1045 K | [25] |
| 9 at% La | Nanostructured bulk prepared from nanoparticles of La-doped $SrTIO_3$ by spark plasma sintering | 0.37 at 973K | [26] |
| 10 at% La | With 20 wt% nano-sized Ag | 0.30 at 883K | [29] |
| La | With Brij-S10 surfactant molar ratio of 0.1 in $SrTiO_3$ film with mesoporous structure | 0.03 at 473K | [30] |
| 20 at% Nb or Ta | Mesoporous $SrTiO_3$ films with Brij-S10 surfactant. | 0.04 at 300K | [31] |
| 8 at% La | Carbon buried sintering for bulk sample preparation | 0.2 at 1000K | [28] |
| 15 at% Nb | Nano-inclusion of yttria stabilized zirconiz (YSZ) | 0.21 at 900 K | [32] |
| 10 at% Nb | Sr-site vacancies, prepared by high energy ball milling followed by carbon burial sintering | 0.21 at 1100K | [33] |

| | | | |
|---|---|---|---|
| Nb | Nano-sized titania on the strontium titanate grains using liquid phase deposition approach | 0.33 at 900 K | [35] |
| 10 mol% La and 10 mol% Nb | Nano-scale modulation doping and microstructure controlling approach | 0.6 at 1100K | [34] |
| 18 at% La and 2 at% Y | Doped with large ions of La and simultaneously, slightly co-doped with small ions of Y | 0.31 at 1023K | [36] |
| 6.7 at% La and 20 at% Nb | Inclusion of Cu | 0.36 at 900K | [37] |
| 6.7 at% La and 20 at% Nb | Inclusion of Fe | 0.38 at 1000K | [37] |
| La and Dy | Sr-deficient $SrTiO_3$ ceramics | 0.29 at 723K | [38] |
| 1 at% La and 1 at% Dy | Sr and O vacancies in $SrTiO_3$ ceramics | 0.19 at 723 K | [39] |
| 10 mol% La and 20 mol% Nb | Composite of pure and doped $SrTiO_3$ with molar ratio of 1:1 | 0.35 at 1000 K | [40] |
| 5 mol% La and 5 mol% Nb | Synthesized under various reducing atmospheres | 0.22 at 473 K | [41] |

In this work, a dual mechanism has been implemented to improve the thermoelectric properties of $SrTiO_3$. Firstly, the incorporation of nano-scale porosity into the bulk sample to suppress the lattice thermal conductivity and Secondly, the carrier concentration optimization by different amount of La doping to enhance the electrical conductivity with the help of first principles calculation. This unique combined approach helps to improve the power factor ae well as *zT* remarkably. This approach can also be utilized in other thermoelectric materials.

## 5.2 Experiment

### 5.2.1 Computational Details

In this work, first principle calculations were performed using density functional theory[70-71] (DFT) implemented by the CASTEP package[72]. The exchange correlation function used to describe the exchange-correlation interaction was the General Gradient Approximation (GGA) with the Perdew–Burke–Ernzerhof (PBE)[73]. Structures are optimized using the Broyden–Fletcher–Goldfarb–Shanno algorithm BGFS[74] with a 4×4×4 K-point set and cutoff energy of 630 eV. The atomic positions and cell vectors are relaxed until the energy, maximum force and maximum displacement are less than $5.0 \times 10^{-6}$eV/atom, 0.01eV/Å, and $5.0 \times 10^{-4}$ respectively. The reciprocal space Brillouin zone paths selected for band structure calculations are shown in Fig 5.1(b), a 13×13×12 K-point set was used to calculate the density of state for Fig 5.1 (d)-(g).

### 5.2.2 Sample Preparation

The synthesis process of La doped $SrTiO_3$ powder with nano-scale porosity by polymeric micelle assembly method using surfactant F127 has been discussed in detail in the previous chapter[86]. Here, La doping level has been changed in different atomic percentages (5, 15, 18, 20, 22 and 25 at%) keeping other things unchanged in the synthesis process. Secondly, to keep the same nanostructure (nano-scale porosity) of all the samples, same amount (600 mg) of surfactant F127 has been used in all samples. The sintering parameters of spark plasma sintering (SPS) to fabricate bulk samples from the nano-porous powder are same as previous work[86].Samples have been symbolised depending on La doping level, for example, sample with 5 at% La doping is noted as 5La-STO and so on 15La-STO, 18La-STO, 20La-STO, 22La-STO, and 25La-STO.

### 5.2.3 Sample Characterization

The powder XRD patterns have been determined by the X-ray diffractometry (Cu Kα, GBC MMA, $\lambda$ = 1.5418 Å) with a step size of 0.02° and speed of 2° per min from 25$^o$ to 80$^o$. The nanostructures and EDS mapping of samples have been studied using field emission scanning electron microscopy (FE-SEM, JEOL 7500F) with a maximum magnification of x1,000,000 and highest resolution of 1nm. The atomic resolution image and EDS mapping have been examined by the atomic resolution microscopy (JEOL ARM-200F). The Thermo Scientific Nexsa XPS system has been used for the X-ray photoelectron spectroscopy (XPS) analysis of the samples. The Seebeck coefficient, $S$ and the electrical conductivity, $\sigma$ have been measured from room temperature to 850 K under vacuum using Ozawa RZ2001i. The thermal diffusivity of the samples has been measured under vacuum conditions using the instrument, LINSEIS

LFA 1000, and the specific heat has been measured under argon atmosphere by DSC-204F1 Phoenix. The weight and dimensions of a rectangular sample have been used to determine the sample density. The results of the samples have been confirmed by repeating all the measurements several times.

## 5.3 Result and Discussion

The crystal structure of $SrTiO_3$, the path used to calculate the Brillioun zone for the band structure and the band structure of pure $SrTiO_3$ are shown in Fig. 5.1(a-c) respectively. The total density of state (DOS) and contribution of *s*, *p* and *d* states on total DOS for undoped and La doped $SrTiO_3$ are shown in Fig. 5.1(d-g). The doping levels are 12 at% (Fig. 5.1(e)), 25 at% (Fig. 5.1(f)) and 50 at% (Fig 5.1(g)) of La. The majority states at the valence band arise from the Ti 2*p* states for either pure or doped $SrTiO_3$. The 12 at% La doping has shifted the Fermi level to higher energy and as a result the majority contribution at the Fermi level is the La 3*d* states. The Fermi level is further shifted up with a 25 at% doping with an increase in the La 3*d* states. However, doping at 50 at% saturates the increasing of Fermi level and these results are in agreement with previous results[87]. The density of state (DOS) data shows that, due to the La doping, the band gap does not change much but the La doping contributes to the conduction band and the Fermi level is shifted to the conduction band. It means that La doped $SrTiO_3$ is become n-type semiconducting material. In practical, we have observed the *n*-type semiconducting behaviour of the La doped $SrTiO_3$. Therefore, the DOS calculation indicates that the electrical transport properties of $SrTiO_3$ can be improved by optimizing the La doping.

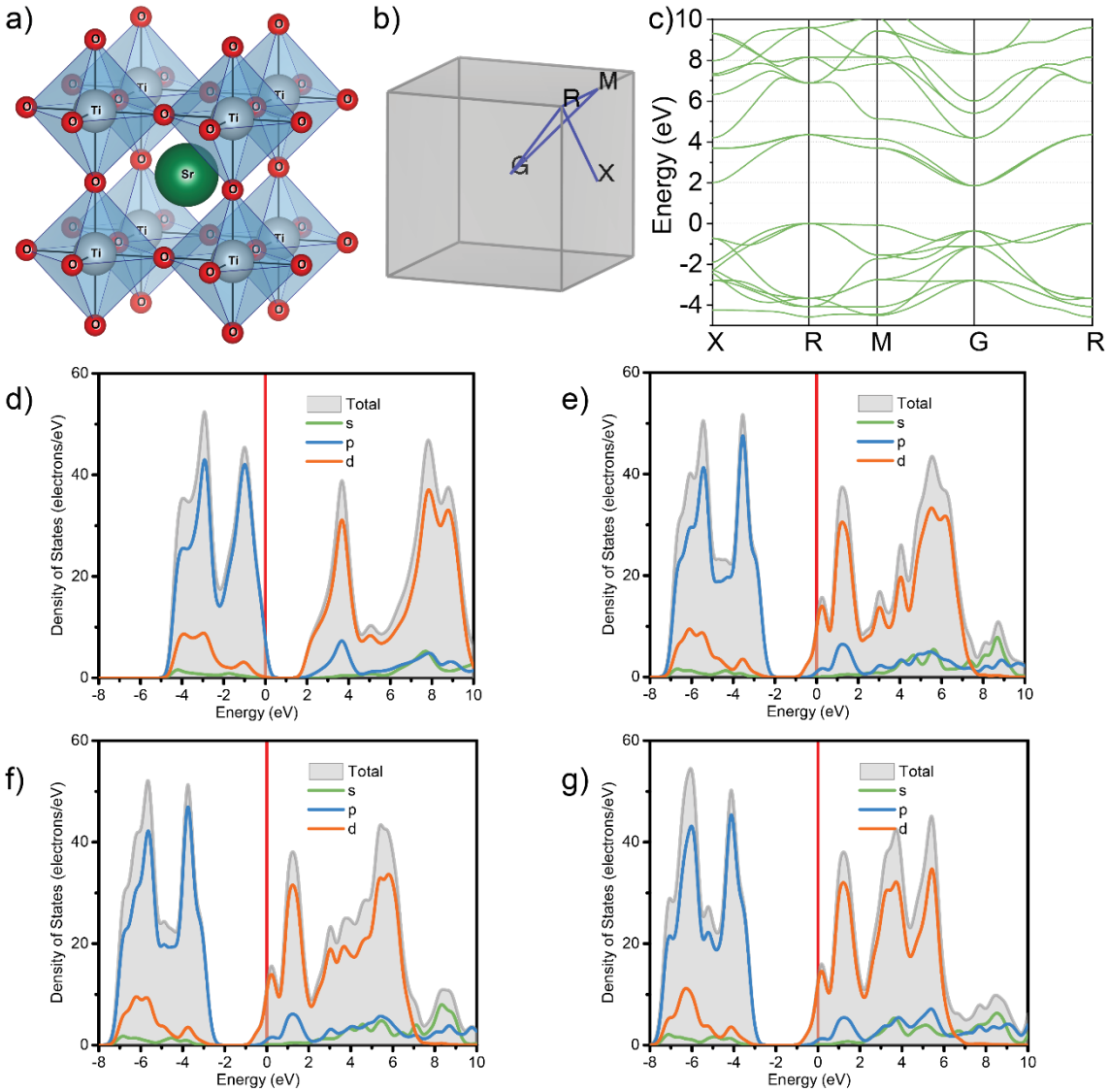


Fig. 5.1 (a) Crystal structure of $SrTiO_3$ (b) the Brillioun zone for the band structure (c) band structure of $SrTiO_3$. Density of states calculation of (d) undoped $SrTiO_3$, (e) 12.5 at% La, (f) 25 at% La and (g) 50 at% La doped $SrTiO_3$.

The powder XRD patterns of bulk samples with different amounts of La doping have matched with pure $SrTiO_3$ as shown in Fig. 5.2 (a). It confirms that all the bulk samples have cubic perovskite $SrTiO_3$ structure with space group, *Pm*-3*m* and there is no secondary peak within the detection limit of XRD. In Fig. 5.2 (b), the enlarged diffraction peaks (110) confirm that there is gradual peak shifting to the higher angles with the increase amount of La doping. The shifting

to the higher angles indicates that Sr atoms are successfully replaced by the La atoms in the crystal structure of $SrTiO_3$. It is because the $La^{3+}$ has smaller ionic radius of 1.36 Å compare to the $Sr^{2+}$ (1.44 Å) [82]. There is a gradual reduction in lattice parameter also which indicates that number of Sr atoms replacement by La atoms increases with the amount of La doping as shown in Fig. 5.2 (c).

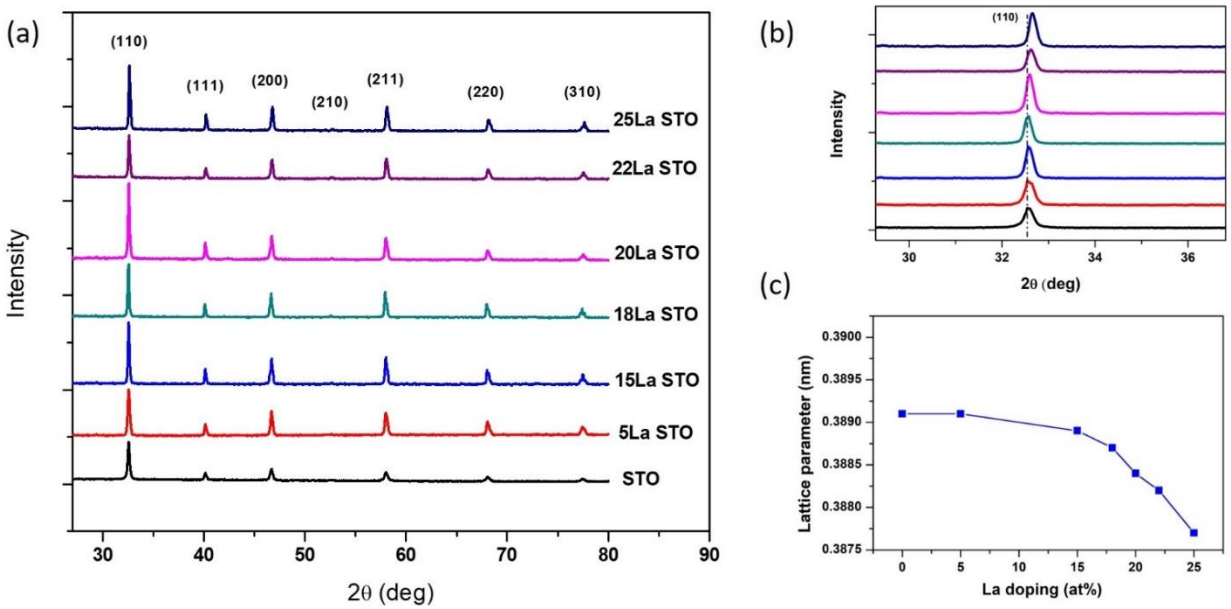


Fig. 5.2 (a) XRD patterns of SrTiO3 bulk samples with different atomic percentage of La doping, (b) The enlarged XRD peak (110) of the samples, and (c) lattice parameter decreases with La doping

The atomic resolution scanning transmission electron microscopy (STEM) imaging and EDS mapping have been used to understand the distribution of elements within the lattice. An atomic resolution high angle annular dark field (HAADF) image of the sample 22La STO viewed along the cube axis is shown in Fig. 5.3 (a). In this imaging mode the contrast varies as a function of $Z^2$, where Z is the mean atomic number. The atomic columns containing the heavier atoms (Sr

and La) appear brighter and larger than those occupied by Ti. The corresponding EDS maps (Fig. 5.3 (b, c and d)) show that the La and Sr atoms occupy one set of lattice sites while the Ti atoms occupy a separate set. The dissimilarity of the La and Ti maps confirm that the La is substituting on the Sr sites. In addition, the contrast of La in Fig. 5.3(d) is high, which suggests a significant La doping have achieved in the measuring area.

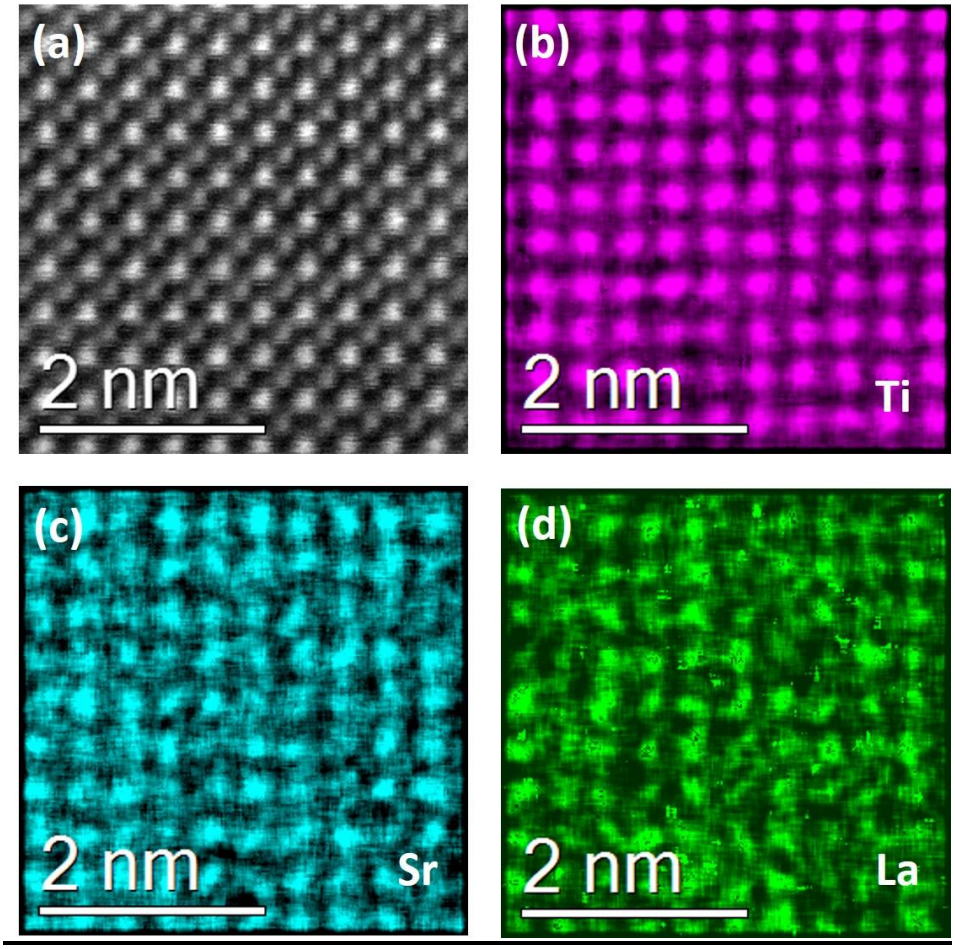


Fig. 5.3 (a) Atomic resolution HAADF image of the sample 22La STO. The EDS maps are shown in: (b) Ti, K; (c) Sr, K and (d) La, L.

In Fig. 5.4 (a-c), the energy dispersive x-ray (EDS) mapping of La in different samples, 5La-STO, 22La-STO, and 25La-STO also confirms that the amount of La increases with increment of doping level and there is uniform distribution of La all over the sample. The EDS mapping

also shows that other elements, Sr, Ti, and O are also uniformly distributed in the sample 22La-STO as shown in Fig. 5.4 (e-g) and the concentration of Sr compared to Ti and O in the sample 22La-STO indicates that it has been replaced by the La.

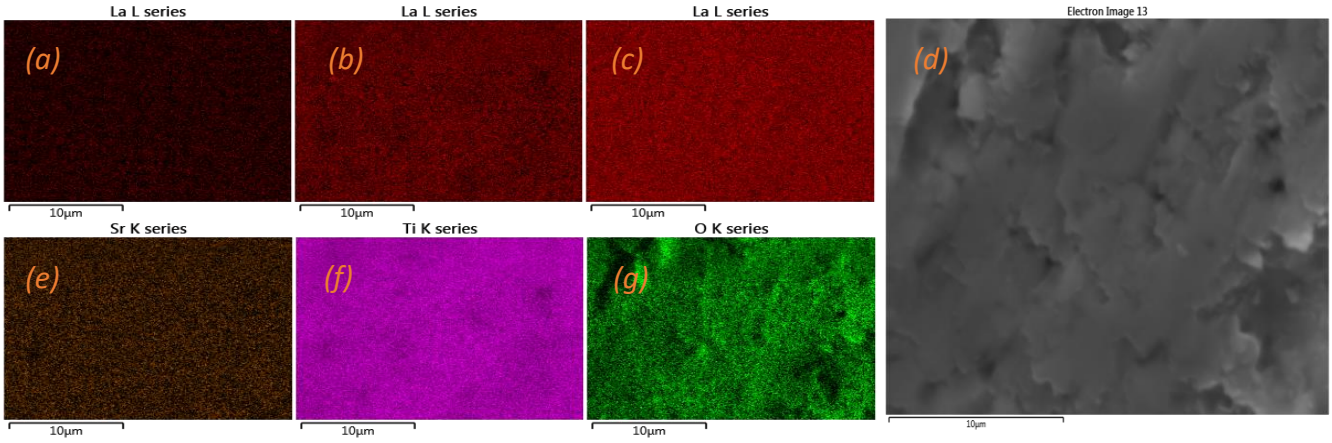


Fig. 5.4 (a-c) EDS mapping of samples with different atomic percentage of La doping, (d) SE-SEM image of the sample 22La-STO, (e-g) EDS mapping of other elements Sr, Ti and O respectively in the sample 22La-STO.

The secondary electron images of samples in Fig 5.5 (a-f) reveal that all the samples with different at% La doping (5 at% to 25 at% of La) are having similar nanostructure and the size of porosity of samples in the nanometre scale. And the grain size of all the samples is few hundred nanometres. The pore size distribution is from 10 to 20 nm [86] and the samples have relative density of around 90%. The samples have low lattice thermal conductivity, and this could be due to the nano-scale porosity and grain size [88].

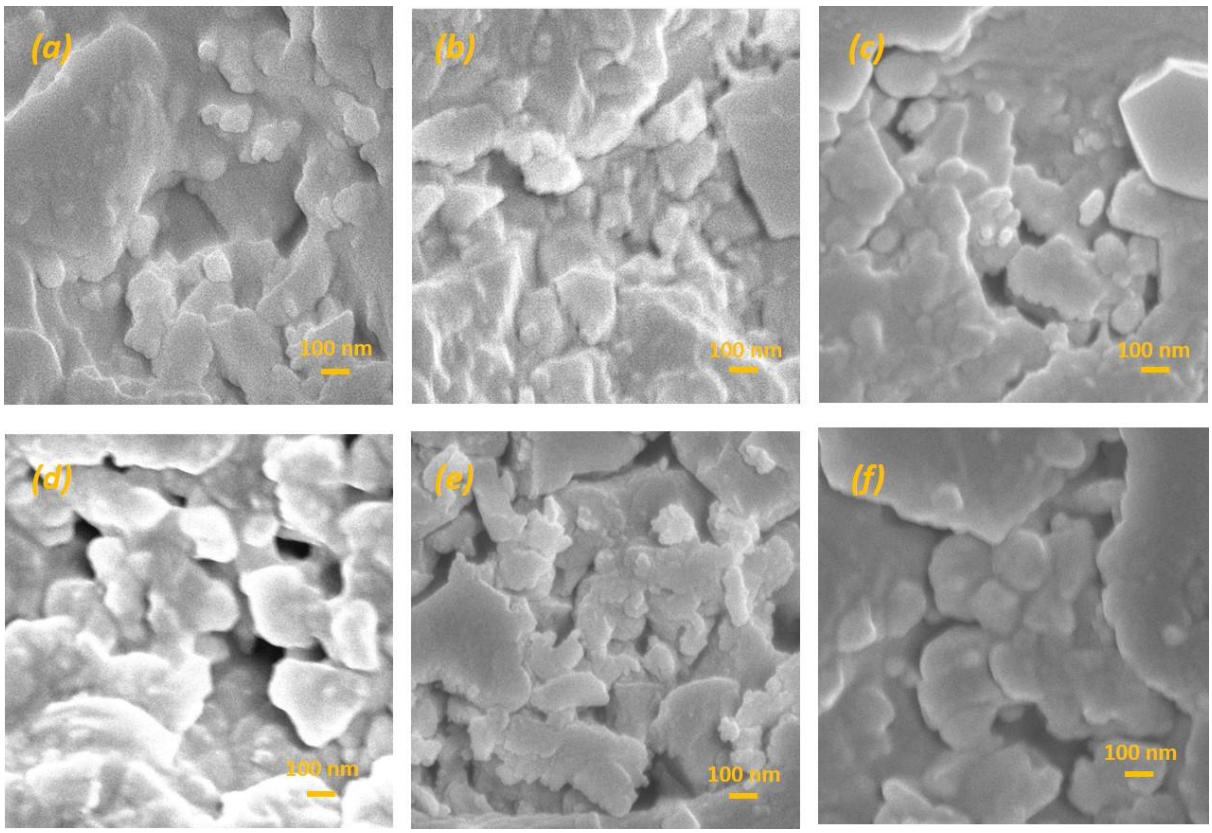


Fig. 5.5 The secondary electron (SE-SEM) images of nanostructure of samples (a) 5La STO, (b) 15La STO, (c) 18La STO, (d) 20La STO, (e) 22La STO and (f) 25La STO

The high-resolution X-ray photoelectron spectroscopy (XPS) shows the oxidation states of elements Sr, La, Ti, and O in the sample 22La STO and 25La STO (Fig 5.6 (a-d)). For both the samples, the binding energy positions of Sr $3d_{3/2}$ and $3d_{5/2}$ and La $3d_{3/2}$ and La $3d_{5/2}$ are corresponding to the oxidation states of $2^+$ and $3^+$ respectively [29, 89]. The binding energies of Ti $2p_{1/2}$ and $2p_{3/2}$ are also close to the reported value of Ti atoms in the perovskite structure of $SrTiO_3$ with oxidation state of $4^+$ [29, 89]. The weak peak of Ti $2p_{3/2}$ at lower binding energy is corresponding to the oxidation state of $3^+$ [33]. The binding energy peak of O 1*s* is associated with the oxidation state of $2^-$ [29, 89].

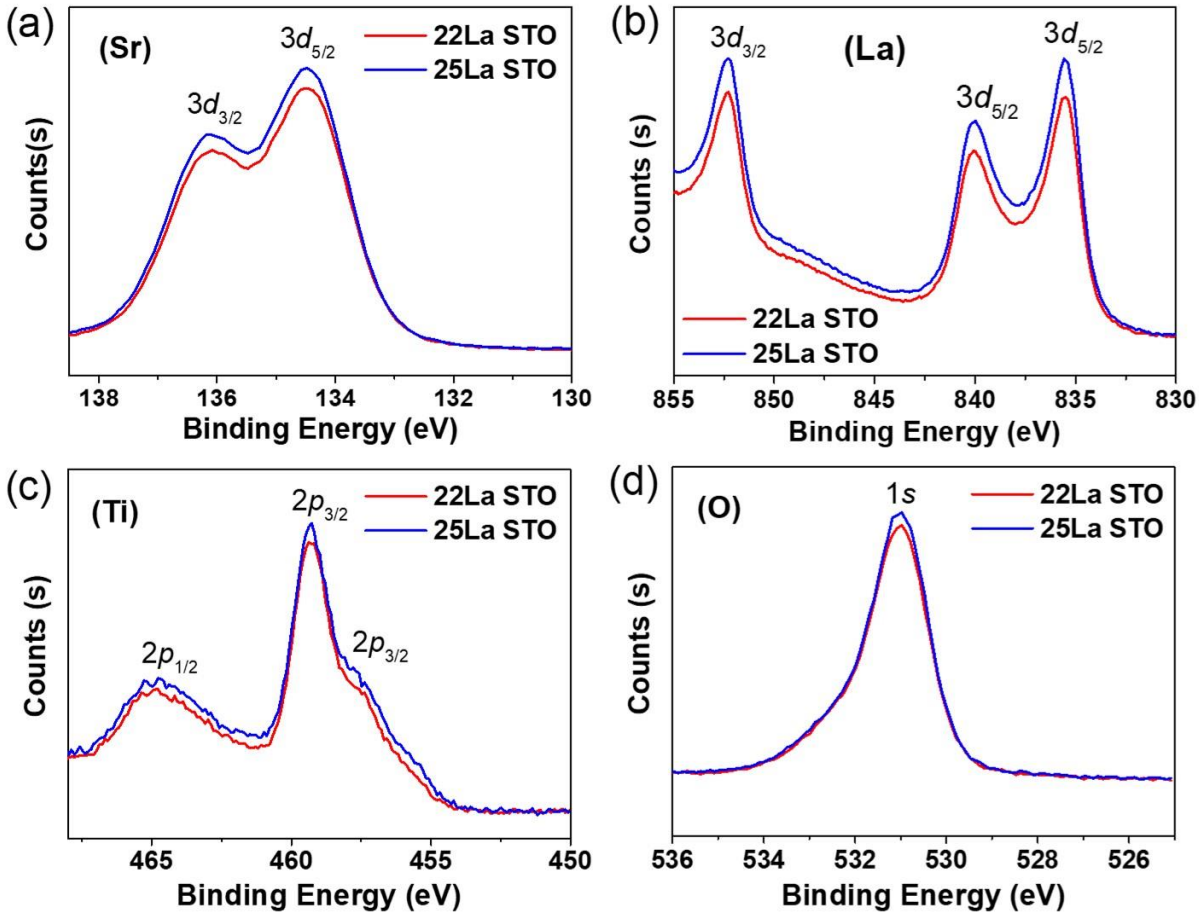


Fig. 5.6 XPS spectra of elements of the sample 22La STO and 25La STO, (a) Sr, (b) La, (c) Ti and (d) O.

The electrical conductivity is linearly proportional to carrier concentration and carrier mobility, $\sigma = n\, e\, \mu$, where $n$ is the carrier concentration and $\mu$ is the carrier mobility. The electrical conductivity of samples initially increases with temperature which is semiconducting behaviour. However, after certain temperature, the electrical conductivity starts to decrease with a lower rate with temperature which is a metallic behaviour as shown in Fig 5.7 (a). The figure also shows that the electrical conductivity shifts to higher value with increment in doping level of La till up to 22 at% doping. This could be due to the increase in carrier concentration and carrier mobility, but the electrical conductivity reduces for the sample with 25 at% La doping and this may be due to a decrease in carrier mobility. Hence, 22 at% La doping is the optimum

doping level for our samples with nanoscale porosity. The sample 22L-STO shows maximum electrical conductivity of 600 s/cm at 550K.

The Seebeck coefficient for doped semiconductor is inversely related to carrier concentration which can be expressed as $S = \frac{8\pi^2 k_B^2}{3eh^2}\ m^* T\ (\frac{\pi}{3n})^{2/3}$, where, $k_B$ stands for Boltzmann constant, $e$ for electron charge, $h$ refers to Planck's constant, $m^*$ refers to the effective mass of the carrier, $T$ is the absolute temperature, and $n$ is the carrier concentration [18]. In Fig 5.7 (b), the Seebeck coefficient of all samples is negative, and the value increases almost linearly with temperature. The sample 5La-STO has the highest value of Seebeck coefficient throughout the temperature range. On the other hand, the sample 22La-STO has lowest Seebeck coefficient compared to other samples. For power generation applications, TE material with high power factor is even more important than high efficiency of the material[16]. There is a remarkable improvement of power factor for the sample 22La-STO compared to other samples. It has power factor of around 1mW/m$^2$K for wide temperature range from 550K to 800K (Fig 5.7 (c)).

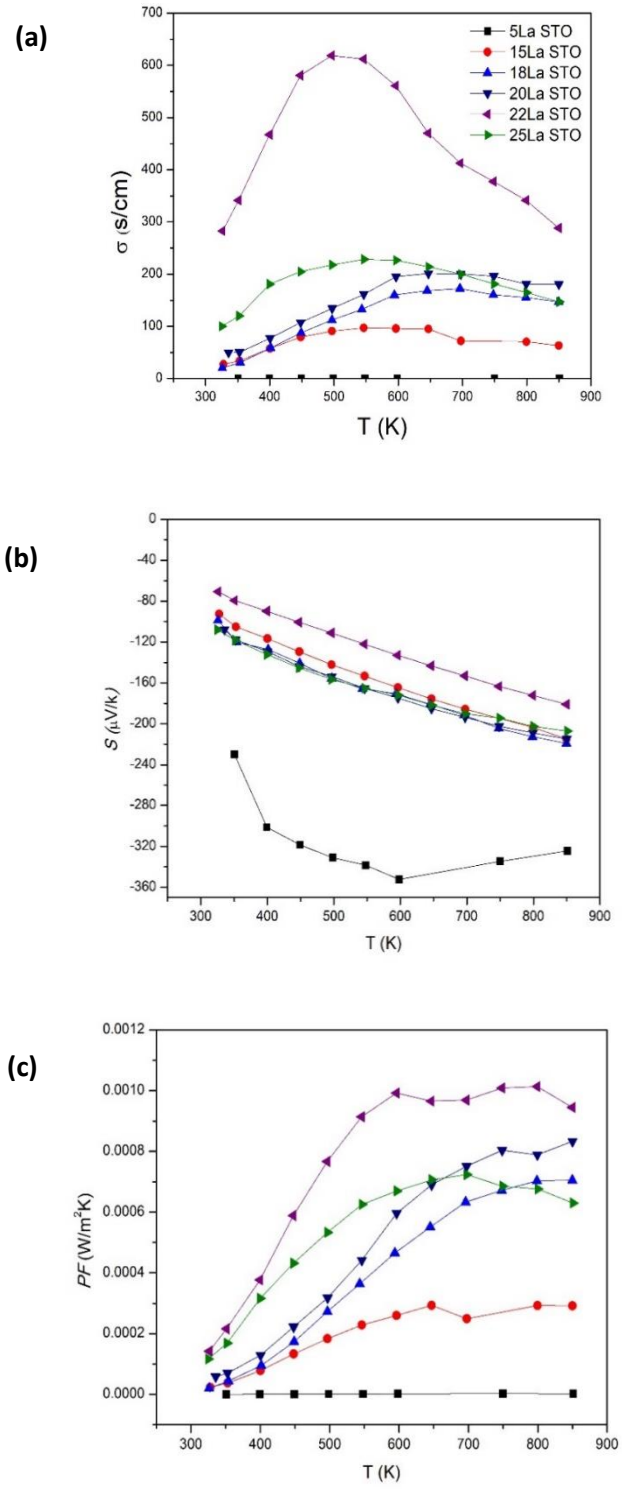


Fig. 5.7 (a) Electrical conductivity, (b) Seebeck coefficient and (c) Power factor of nanoporous SrTiO3 samples with different atomic percentage of La doping.

The total thermal conductivity of TE material depends on thermal diffusivity, specific heat capacity, and density of the material which can be presented as, $\kappa = \alpha\, C_p\, \rho$, Where, $\alpha, C_p$, and $\rho$ are thermal diffusivity, heat capacity at constant pressure, and the material density, respectively [12]. The total thermal conductivity of $SrTiO_3$ samples with different La doping levels is shown in Fig. 5.8 (a). The important aspect of our samples due to nano-scale porosity is that the total thermal conductivity of the samples is substantially lower than the reference samples special at lower temperatures. The samples with high La doping (22La-STO and 25La-STO) show low thermal conductivity at low temperatures may be due to replacement of Sr by La which has higher atomic mass.

The total thermal conductivity can be divided into two parts, one part is $\kappa_{el}$ which is the thermal conductivity from the movement of electrons and holes, and another part is $\kappa_{ph}$ which is the thermal conduction by lattice vibration also known as phonon, $\kappa = \kappa_{ph} + \kappa_{el}$ [15]. As, Fig. b and c show the phonon thermal conductivity and the electrical thermal conductivity, respectively. The phonon thermal conductivity, $\kappa_{ph}$ can be express as follow, $\kappa_{ph} = \frac{1}{3} C_v V l$, where the heat capacity ($C_v$) at constant volume and the phonon velocity ($V$) are constant, therefore, the $\kappa_{ph}$ mainly relies on the phonon mean free path (MFP) ($l$) [3]. The $\kappa_{ph}$ of the samples has been lower significantly may be because of nano-scale porosities into the samples.

From Wiedemann-Franz law, the electrical thermal conductivity, $\kappa_{el}$ is proportional to electrical conductivity, $\sigma$, and temperature, $T$. $\kappa_{el} = LT\sigma$, where $L$ is the proportional constant known as Lorenz number. The Lorenz number is an experimental value and normally, $L$ is treated as a universal factor with the value of $2.44 \times 10^{-8}\ \mathrm{W\Omega/K^2}$ for a degenerate semiconductor [15]. The value of $\kappa_{el}$ is extremely small compared to the value of $\kappa_{ph}$ for the

$SrTiO_3$ samples. Therefore, the effect of $\kappa_{el}$ in total thermal conductivity is insignificant as shown in Fig. 5.8 (c).

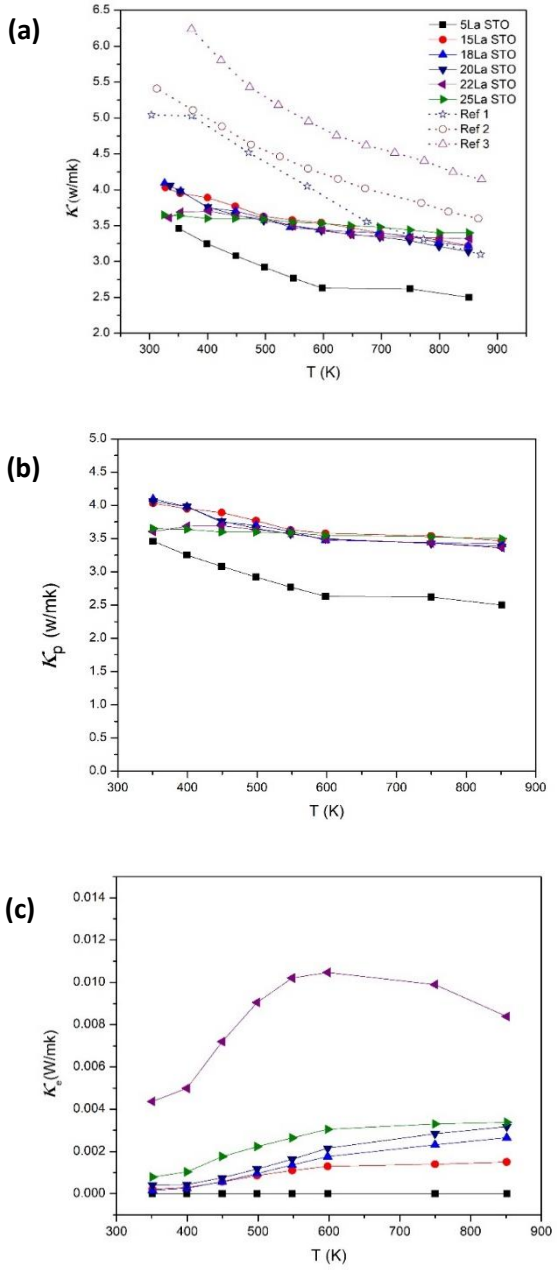


Fig. 5.8 (a) Total thermal conductivity, (b) Phonon thermal conductivity and (c) Electrical thermal conductivity of SrTiO3 samples with nano-scale porosity and with different atomic percentage of La doping.

It can be observed from Fig. 5.9 that the dimensionless figure of merit, *zT* improves with the increase of La doping. It can be said that 22 at% La doping (22La-STO) is an optimum doping level for our samples as the sample 22La-STO shows highest *zT* value compared to other samples throughout the temperature range from 300K to 850K. It shows the maximum *zT* value of 0.26 at 850K. As compared to reference sample, the sample 22La-STO shows higher *zT* at lower temperature and this is a remarkable improvement for metal oxide based thermoelectric material.

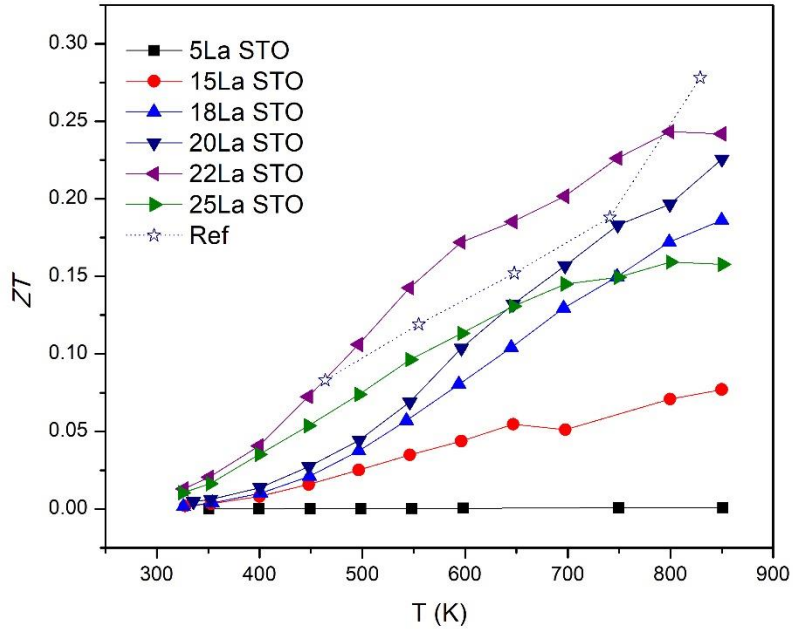


Fig. 5.9 Dimensionless figure of merit of nano porous SrTiO3 samples with different concentration of La.

## 5.4 Conclusion

La has been doped in six different atomic percentages (5, 15, 18, 20, 22 and 25 at%) into $SrTiO_3$ bulk sample with nano-scale porosity. The porosity of samples is kept similar by adding equal amount of surfactant F127 during the powder preparation of $SrTiO_3$. The sample with 22at% La doping (22La-STO) exhibits highest electrical conductivity compared to other samples throughout the temperature range. On the other hand, the phonon thermal conductivity of all the samples is same because of similar nanostructure of the samples and the contribution of electrical thermal conductivity is insignificant in total thermal conductivity. Due to this dual mechanism, the sample with 22at% La doping shows the highest power factor and figure of merit. It has a power factor of around $1mW/mK^2$ from 550K to 800K. And the highest value of dimensionless figure of merit, $zT$ is 0.26 at 850K.

The result presented in this chapter has been published in the journal ACS Applied Materials and Interfaces by me as a first author. Sheik Md. Kazi Nazrul Islam, Ridwone Hossain and Guangsai Yang helped to conduct experiments and to result analysis. The DFT calculation was done by Frank Yun. Aslam Khan, Jongbeom Na, and Miharu Eguchi contributed to manuscript writing. Md. Shahriar A. Hossain, Yusuke Yamauchi and Xiaolin Wang supervised and revised the manuscript.

*"Significant Improvement in Electrical Conductivity and Figure of Merit of Nanoarchitectured Porous SrTiO3 by La Doping Optimization";* Al Jumlat Ahmed, Md. Shahriar A. Hossain, Sheik Md Kazi Nazrul Islam, Frank Yun, Guangsai Yang, Ridwone Hossain, Aslam Khan, Jongbeom Na, Miharu Eguchi, Yusuke Yamauchi, and Xiaolin Wang; ACS Applied Materials & Interfaces ***2020*** 12 *(25), 28057-28064; DOI: 10.1021/acsami.0c01869.*

# 6. Significant Reduction in Thermal Conductivity and Improved Thermopower of Electron-Doped $Ba_{1-x}La_xTiO_3$ with Nanostructured Rectangular Pores

## 6.1 Introduction

Metal oxide thermoelectric (TE) materials have tremendous potential for waste heat recovery from automotive exhaust systems and industrial furnaces because they are chemically stable at high temperature, and also offer robust physical properties[90]. The performance of TE materials is assessed by the dimensionless figure of merit, $zT = \frac{S^2\sigma}{\kappa}T$, where, $S$, $\sigma$, $T$, and $\kappa$ are the Seebeck coefficient which is also known as the thermo-power, the electrical conductivity, the absolute temperature, and the thermal conductivity respectively [14-15, 18, 75]. The term $S^2\sigma$ is called the power factor of the thermoelectric material.

Barium titanate ($BaTiO_3$) is a very well-studied material and is very popular as a lead-free ferroelectric (piezoelectric) material[46]. The perovskite crystal structure of $BaTiO_3$ changes with temperature. Above the Curie temperature (120 $^oC$), it has a cubic crystal structure. Below the Curie temperature which lies near ambient temperatures (120 to 5 $^oC$), one axis (the *c* axis) stretches, while the other two axes shrink, as the crystal structure becomes tetragonal. Above the Curie temperature, $BaTiO_3$ does not show any piezoelectric effect due to its cubic perovskite structure. However, it has a similar cubic perovskite structure like $SrTiO_3$ above the Curie temperature, but its thermoelectric properties are not well studied [48-49]. A previous theoretical study compares the thermoelectric properties of $SrTiO_3$ and $BaTiO_3$. The study describes that due to the higher lattice constant (4.060 Å) of $BaTiO_3$ compared to $SrTiO_3$ (3.928 Å), the

$BaTiO_3$ has a lower electrical conductivity but higher Seebeck coefficient in terms of carrier concentration[48]. The intrinsic thermal conductivity at room temperature of $BaTiO_3$ is also low (6 $W \cdot K^{-1}m^{-1}$) compared to $SrTiO_3$ (12 $W \cdot K^{-1}m^{-1}$). These points indicate that the $BaTiO_3$ could be a potentially useful thermoelectric oxide material.

Some experimental studies were also done on the thermoelectric properties of $BaTiO_3$. Thermoelectric properties of Fe doped $BaTiO_3$ were reported at high temperature[50]. The XRD results show the crystal structures of Fe doped $BaTiO_3$ are mixtures of tetragonal and cubic perovskite $BaTiO_3$ phases. The electrical conductivity increases with temperature and Fe concentration because of the substitution of $Ti^{4+}$ with $Fe^{3+}$ which also increases the oxygen vacancy population. The power factor also increases with temperature and Fe concentration. The mixed structure of crystalline phases has good potential for enhancing the thermoelectric properties[50].

In another study, barium titanate and graphene oxide composites were prepared by the spark plasma sintering (SPS) technique containing graphene oxide up to 4 weight%. The maximum $zT$ value of 0.008 at 550 K was achieved in the sample with 1.7 w% of graphene oxide [51]. In related work, it was reported that the Eu substitution in reduced $Ba_{1-x}Eu_xTiO_{3-\delta}$ slightly decreases the Seebeck coefficient and enhances the thermal conductivity. But it improves the electrical conductivity significantly by introducing new electronic states in the bandgap, near the band-edge. The sample $Ba_{1-x}Eu_xTiO_{3-\delta}$, $x = 0.9$ shows a $zT$ of 0.25 at 1100 K [52]. Following on this theme, the thermoelectric properties of La doped $SrTiO_3$-$BaTiO_3$ solid solutions have been studied for different levels of Sr substitution. The electrical conductivity increases, but the Seebeck coefficient decreases with increasing Sr concentration, which is related to the lattice parameter. The latter result indicates that a shorter Ti-Ti distance is desirable for improvement in the power factor. The thermal conductivity increases with Sr concentration which disagrees

with the point defect scattering theory[53]. Conducting polyaniline (PANI) and $BaTiO_3$ nanoparticle composite films have also been investigated for thermoelectric properties[54]. The composite film behaves like a *p*-type thermoelectric material. The electrical conductivity is improved compared to pure $BaTiO_3$, but the Seebeck coefficient recedes. Therefore, there is no significant improvement in the power factor of conducting polyaniline and $BaTiO_3$ nanoparticle composite films. In another study, lead magnesium-niobate $Pb(Mg_{1/3}Nb_{2/3})O_3$ (PMN) has been incorporated in different contents with pure $BaTiO_3$ to improve its thermoelectric efficiency by increasing the degree of A and B site disordering by $Pb^{2+}$ and (Mg, Nb $)^{4+}$ ions. It shows that by increasing the contents of PMN, the electrical conductivity increases, and the thermal conductivity decreases. Therefore, there is an overall improvement in the thermoelectric performance of PMN incorporated $BaTiO_3$[55]. Complex double perovskites $Ba_xSr_{1-x}TiFeO_6$ with $0.0 \leq x \geq 0.25$ show *p*-type thermoelectric behaviour and the sample with $x = 0.25$ shows very high thermo-power of 800 µV/K at 1123K [56]. On the other hand, Niobium doped barium titanate ($BaNb_xTi_{1-x}O_3$) exhibits *n*-type thermoelectric behaviour whose electrical conductivity is directly proportional to the temperature [57]. Yttrium doped *n*-type $BaTiO_3$ shows a thermo-power of - 550 µV/K at 350 K [58].

Previously, we have reported that La doping optimization and nanostructured porosity into bulk material can improve the thermoelectric properties of $SrTiO_3$ [88, 91]. $BaTiO_3$ has similar cubic perovskite structure above the Curie temperature. It has intrinsically low thermal conductivity and chemical stability at high temperature. Its electrical conductivity can be changed easily by electron doping. Therefore, $BaTiO_3$ is a promising thermoelectric material. Electron doped $BaTiO_3$ was reported as a thermoelectric material though it exhibited low figure of merit such as $zT$ value of 0.008 at 550 K [51]. It was also reported that its transport properties like electrical conductivity and Seebeck coefficient can be improved by doping optimization[48, 52, 55]. However

so far, no research has done to reduce the thermal conductivity which can improve its thermoelectric performance. Here we report for the first time that the thermal conductivity of $BaTiO_3$ can be suppressed and the Seebeck coefficient can be improved greatly by introducing nanostructured pores into the bulk sample. The main objective of our research is to examine the effect of nanostructured pores on thermoelectric properties of $BaTiO_3$ which is intrinsically an insulating material. Therefore, the electrical conductivity is improved, and it becomes *n*-type semiconducting material because of electron doping by adding La in atomic percentage.

## 6.2 Experiment

### 6.2.1 Calculation Details

Density functional theory (DFT) is implemented using the CASTEP package [92] . The exchange-correlation function used to describe the exchange-correlation interaction was the General Gradient Approximation (GGA) with the Perdew–Burke–Ernzerhof (PBE) formulation[73], with an ultra-soft pseudopotential. Atomic positions of the crystal structures are optimized using the Broyden–Fletcher–Goldfarb–Shanno algorithm[93]. The Maximum cut off energy used is 630 eV with a $4 \times 4 \times 4$ *k*-point set for optimizations to less than $5.0 \times 10^{-6}$ eV/atom. The DOS calculation is performed using a $25 \times 25 \times 25$ *k*-point mesh.

### 6.2.2 Sample Preparation

To synthesis La doped $BaTiO_3$ powder, Barium acetate and lanthanum acetate hydrate were dissolved in different ratios into Acetic acid at 50 $^oC$ and then titanium butoxide was further added into the solution at room temperature. The solution was transferred into filter paper for calcination at 600 $^oC$ for 10 min for powder preparation. The process has been illustrated in the Fig. 6.1. The La doped samples are symbolized after the amount of doping into $BaTiO_3$ like

($Ba_{1-x}La_xTiO_3$ ($x$ = 0.15, 0.20, 0.30, 0.50 and 0.90)) 15L BTO, 20L BTO, 30L BTO, 50L BTO and 90L BTO.

To introduce nanostructured porosity in La doped $BaTiO_3$ sample, the commercially available triblock copolymer (F127) was dissolved into ethanol. This solution was mixed properly with the above-mentioned La doped $BaTiO_3$ solution and then it was transferred into filter paper for calcination at 600 $^oC$ for 10 min for powder preparation. The synthesis protocol of powders with nano-scale porosity was already discussed in detail in our previous publication[88]. The sample is denoted as 20L BTO F127 based on La doping amount (20 at%) and the name of the surfactant, F127.

The main objective of the thesis is to supress thermal conductivity of oxide thermoelectric material by introducing nanostructure (nano pores and nanocrystalline) into bulk sample. It was reported that it is possible to achieve an average crystallite size well below 50 nm in the densely compacted bulk material by spark plasma sintering technique[63]. The lower sintering temperature and shorter sintering time of SPS process compared to the conventional sintering process allows obtaining dense bulk material with little grain growth. It was also reported that the nanostructured materials processed by SPS technique improve efficiency of thermoelectric material, since the nanostructure reduces the thermal conductivity of the material dramatically while maintaining the electrical transport properties[63]. Sol-gel process and SPS can significantly decrease the thermal conductivity of $SrTiO_3$ based ceramics. The lowest value of thermal conductivity reported so far is 1.19 $Wm^{-1}K^{-1}$ in the sample sintered at 1203K in SPS [64]

The powder samples were transformed in bulk sample using the spark plasma sintering (SPS) process. The sintering parameters for spark plasma sintering (SPS) to fabricate bulk samples

from the nano-porous powder were selected based on published works listed in the Table 6.1. The relative density of all the samples is above 90%. The applied temperature, pressure and holding period were 1150 $^{o}$C, 70 MPa, and 15 min, respectively.


Fig. 6.1 Different stages of synthesis process of La doped $BaTiO_3$ bulk samples from precursors solution

Table 6.1 Sintering parameters for $BaTiO_3$ in spark plasma sintering (SPS)

| Temperature $^oC$ | Heating rate $^oC\ min^{-1}$ | Pressure MPa | Sintering period min | Relative density % | Ref. |
|---|---|---|---|---|---|
| 750 | 200 | 50 | 3 | 94 | 94 |
| 900 | | | | 99 | |
| 1100 | 50 | 80 | 1 | | 51 |
| 950 | 100 | 75 | 5 | | 95 |
| 975 | | | | 96 | |
| 1000 | | | | 99 | |
| 1025 | | | | 99 | |
| 1050 | | | | 99 | |

6.2.3 Sample Characterization

The powder XRD patterns were determined by the X-ray diffractometry (Cu Kα, GBC MMA, $\lambda$ = 1.5418 Å) with a step size of 0.02° and speed of 2° per min from 25$^o$ to 80$^o$. The nanostructures and EDS mapping of the polished surface of samples were studied using field emission scanning electron microscopy (FE-SEM, JEOL 7500F) with a maximum magnification of x1,000,000 and highest resolution of 1nm. Transmission electron microscopy (TEM) images were captured in the instrument JEOL2010 ARM. The thermopower (Seebeck coefficient), *S*, and the electrical conductivity, $\sigma$ were measured from room temperature to 950 K under vacuum using Ozawa RZ2001i. The thermal diffusivity of the samples was measured under vacuum conditions using the instrument, LINSEIS LFA 1000, and the specific heat was measured under argon atmosphere by DSC-204F1 Phoenix. The weight and dimensions of a

rectangular sample were used to determine the sample density. The results of the samples were confirmed by repeating all the measurements several times.

## 6.3 Result and Discussion

### 6.3.1 Density Functional Theory (DFT) Calculations

Fig. 6.2 shows the total density of states (TDOS) and the contribution of electrons from *s*, *p,* and *d* orbitals to the DOS for undoped (Fig. 6.2(a)) and La doped $BaTiO_3$. Different doping levels are considered by varying the amount of La yielding cells including: $La_{0.25}Ba_{0.75}TiO_3$, $La_{0.5}Ba_{0.5}TiO_3$ and $La_{0.75}Ba_{0.25}TiO_3$ as shown in Fig. 6.2(b-d). For all cases, the electrons of *p* orbital are the majority contributor of the valence band and electrons of *d* orbital are the majority contributor of the conduction band. The Fermi level shifts into the conduction band as shown in Fig. 6.2(b) for 25 at% La doping and the material becomes a *n*-type semiconductor with improved electrical conductivity. However, for 50 and 75 at% La doping, there is no further increment in the DOS at the Fermi level and the band gap only increases slightly as shown in Fig. 6.2(c and d) respectively. The band structures of super cell for bare sample $Ba_8Ti_8O_{24}$ and 25 at% La added sample $Ba_6La_2Ti_8O_{24}$ are available in Fig. 6.3. The band structures show that the Fermi level shifts toward the conduction band due to 25 at% La doping which means the doped sample is become a *n*-type semiconductor and the energy band gap reduces to 1.8 eV. This finding predicts that the electrical conductivity is increase by moderate La-doping which results in a *n*-type semiconductor, but higher doping levels will not result in any additional enhancement in the conductivity.

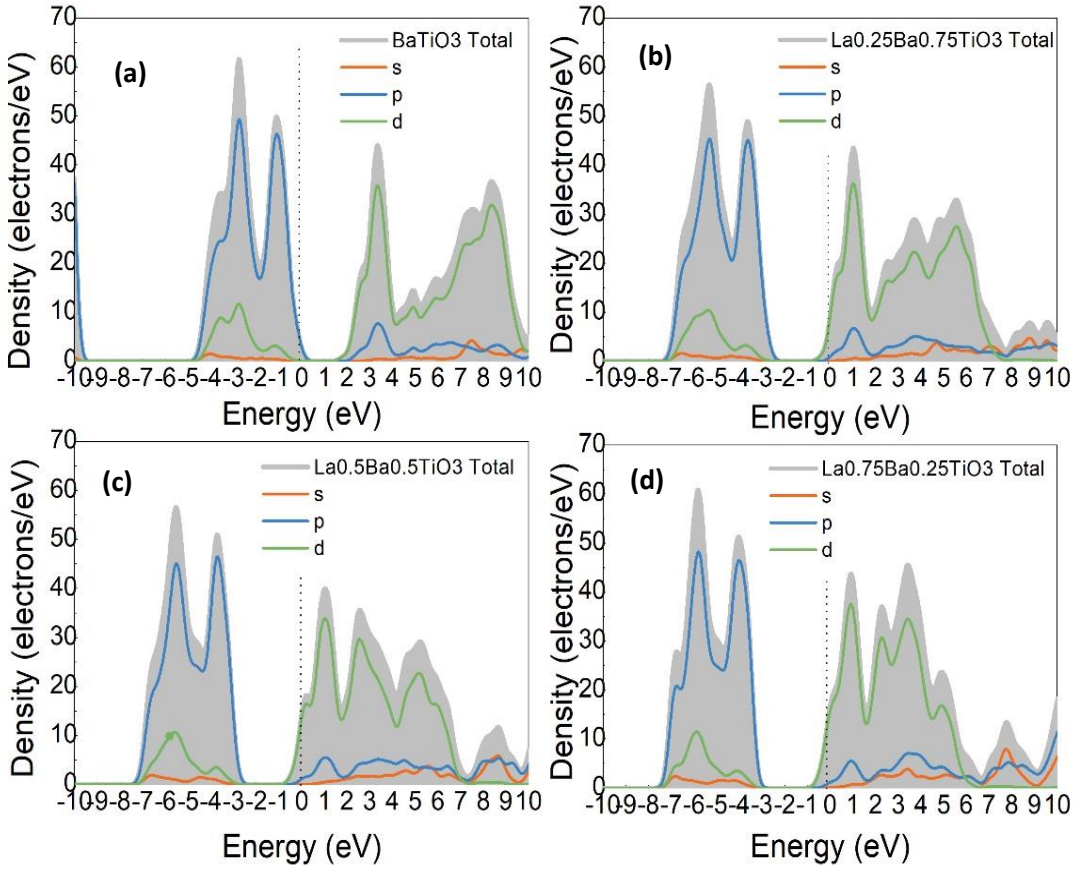


Fig. 6.2 The density of state (DOS) of $BaTiO_3$ samples with different La doping (a) bare, (b) 25 at% La, (c) 50 at% La and (d) 75 at% La doped $BaTiO_3$

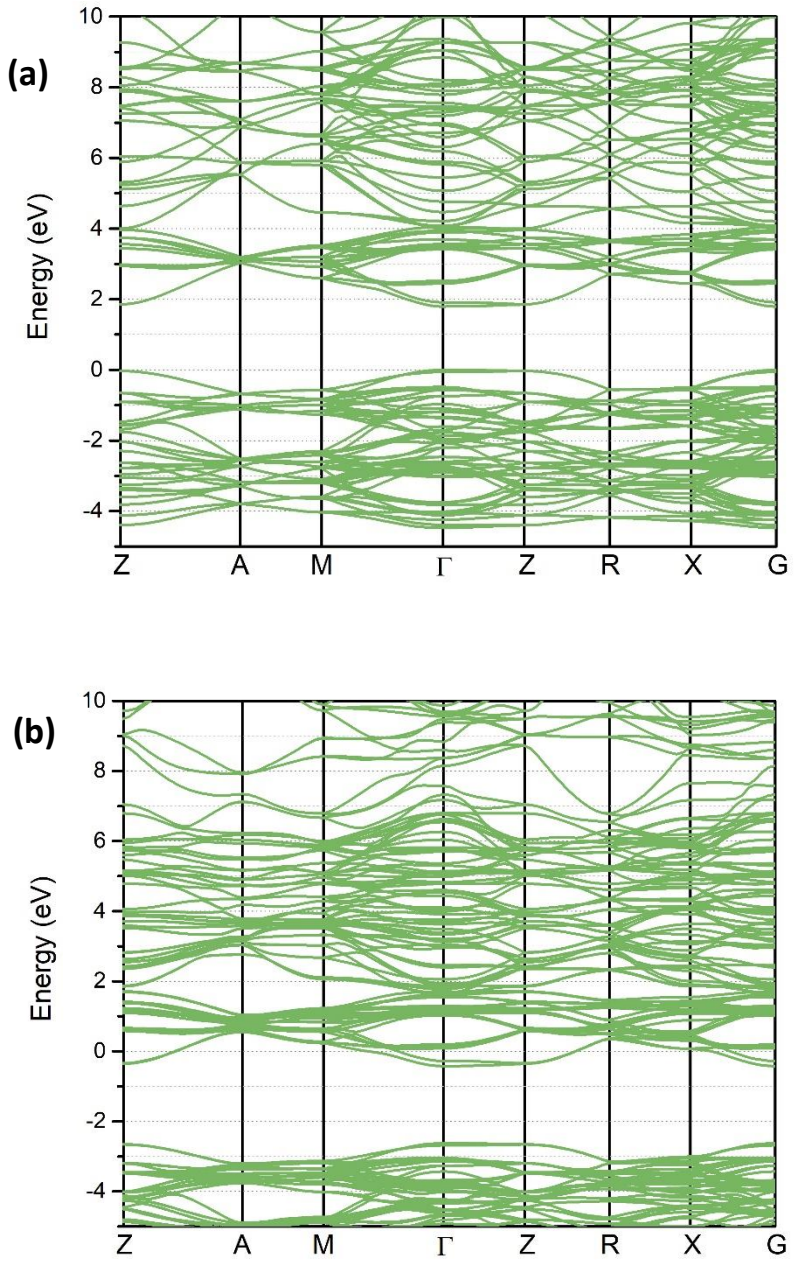


Fig. 6.3 Band structure of supercell $Ba_8Ti_8O_{24}$ calculated using density functional theory (DFT) (a) bare $BaTiO_3$ and (b) 25 at% La doped $BaTiO_3$

6.3.2 Experimental Results

The X-ray diffraction (XRD) patterns of La doped $BaTiO_3$ powder samples calcinated at 600 $^{o}$ C are shown in Fig. 6.4. All the samples were measured by the same instrument. The calcinated powder samples with and without La doping have the cubic $BaTiO_3$ phase (JCPDS data No. 31-0174)[96]. The (200) peaks located at 45$^{o}$ are marked with dotted box. It is interesting to observe that the sample 20L BTO F127 prepared with 600 mg of surfactant F127 shows more obvious XRD peaks, compared to other samples prepared without surfactant F127. The average crystallite size of the samples was calculated from the XRD peaks using the Scherrer's equation. The calculations show that samples with and without surfactant F127 have average crystallite size of around 20 nm. It suggests that the crystallite size of the sample with surfactant F127 does not change due to the presence of nanoscale pores.

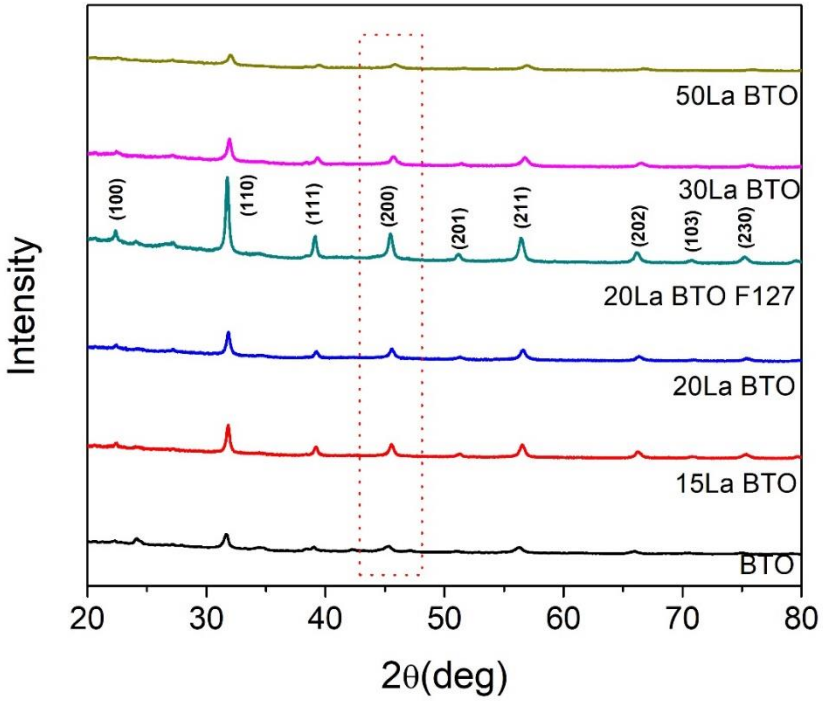


Fig. 6.4 XRD patterns of La doped $BaTiO_3$ powder samples calcinated at 600 $^{o}$C

The XRD patterns of the La doped $BaTiO_3$ bulk samples synthesised by spark plasma sintering (SPS) are shown in Fig. 6.5(a-1). The overall synthesis process including the SPS step is shown in Fig. 6.1. The XRD patterns confirm that the primary phase is cubic $BaTiO_3$, since there is a single peak at around 45°. The same general features are observed in the XRD patterns of the starting powder samples (Fig. 6.4) prior to sintering. In Fig. 6.5(a-2), the gradual shift toward higher diffraction angles of the enlarged (110) peak proves that the La doping into the lattice of $BaTiO_3$ causes substition and lattice contraction. The gradual reduction in the lattice parameter with an increasing La doping indicates that Ba atoms on the A sites of the $ABO_3$ crystal system are replaced by La since La (217 pm) has a smaller atomic radius than the Ba (253 pm) as shown in Fig. 6.5(b).

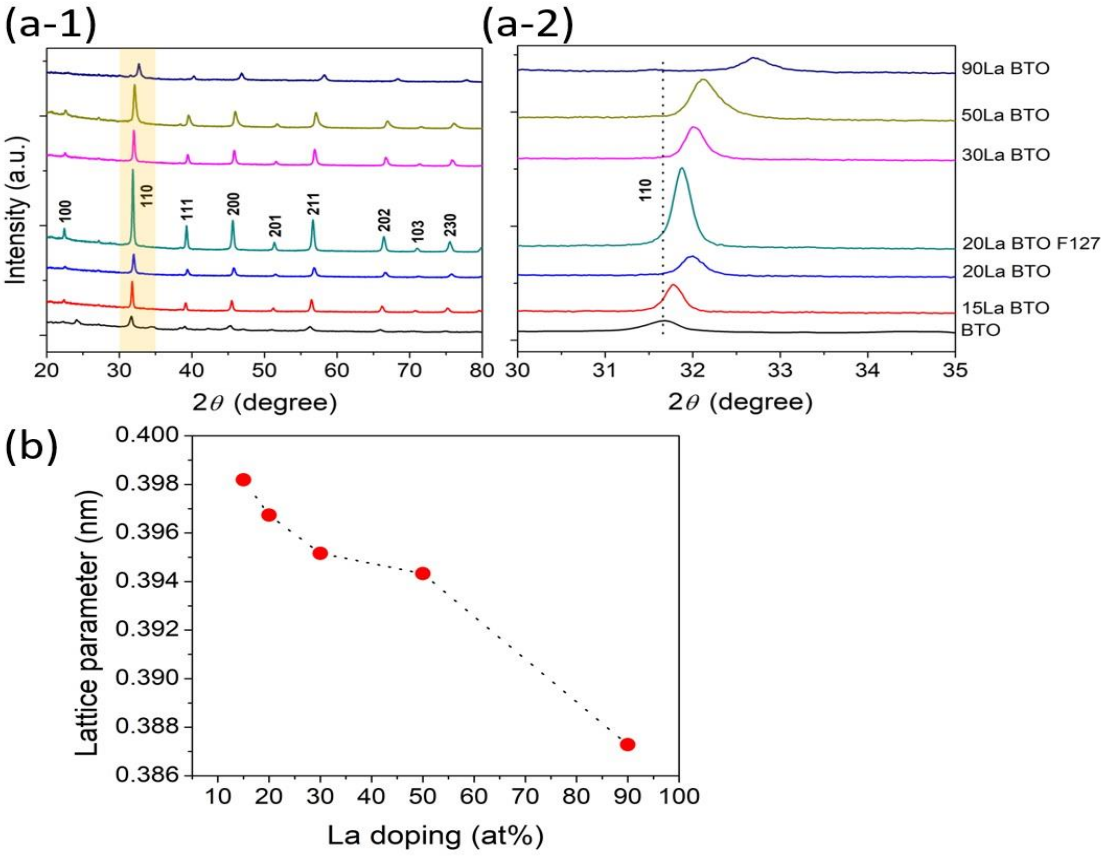


Fig. 6.5 (a-1) XRD pattens of $BaTiO_3$ bulk samples with different atomic percentage of La doping, (a-2) the enlargered peak (110) shows the peak shifting with La doping and (b) lattice parameter with La doping in atomic percentage.

The 20L BTO F127 sample was prepared by adding the surfactant F127 during the powder preparation (Fig. 6.1). During the solution preparation, the inorganic species accumulates around the micelles. The solution is dispensed into filter paper and is kept at 600$^{o}$C for calcination. During calcination, the crystal formation of the frameworks starts around the micelles and the micelles are removed within the crystal at high temperature. In Fig. 6.6, the nitrogen gas adsorption-desorption isotherm, pore size distribution curve and the transmission electron microscopy (TEM) images of the sample (20L BTO F127) confirms the presence of nanostructured pores. In Fig. 6.6(a), a gradual uptake of nitrogen gas in the adsorption range indicates that the resulting pore sizes are in random. The pore size distribution curve (Fig. 6.6(b)) shows the pore sizes are distributed in the range from 2 nm to 16 nm, with majority pores having diameters of 4 nm. The TEM images (Fig. 6.6(c and d)) give localized information on the existence of nanostructured pores of size from 3 nm to 7 nm where the majority pores are around 4 nm which is in line with the pore size distribution result. The presence of lattice fringes in the TEM indicates that the pores are formed within crystalline grains and most of the pores are rectangular in shape. The TEM images also show that the distance between pores is a few nanometres. In contrast, the TEM images (Fig. 6.6(e and f)) of the sample without surfactant F127 (20L BTO) reveal the absence of nanoscale pores within the crystalline grain. The lattice fringes in Fig. 6.6(e) confirm well developed crystallinity of the sample. The above results provide direct evidence that the sample 22L BTO F127 has nanostructured pores due to the use of the surfactant F127. Generally, the resulting pore shapes depends on the shape of the used micelles. Mesoporous/nanoporous materials prepared by soft-templating methods has shown spherical- or tubular-shaped pores with curvatures. In our experiments, the porous powders were densified at high temperature (1150$^{o}$C) and high pressure (70 MPa) within short

period of time using spark plasma sintering (SPS). It can be suspected that during the first sintering process, the nano crystallisation takes place, and the pores are end up in rectangular shape. The theoretical studies show that the phonon thermal conductivity in nanostructured material depends on pore shape and dimension[97-98]. The computational results show that the nanostructured material with square shape pores has low phonon thermal conductivity compared to circular shape pores because pores with sharp edges can scatter phonons more effectively [99].

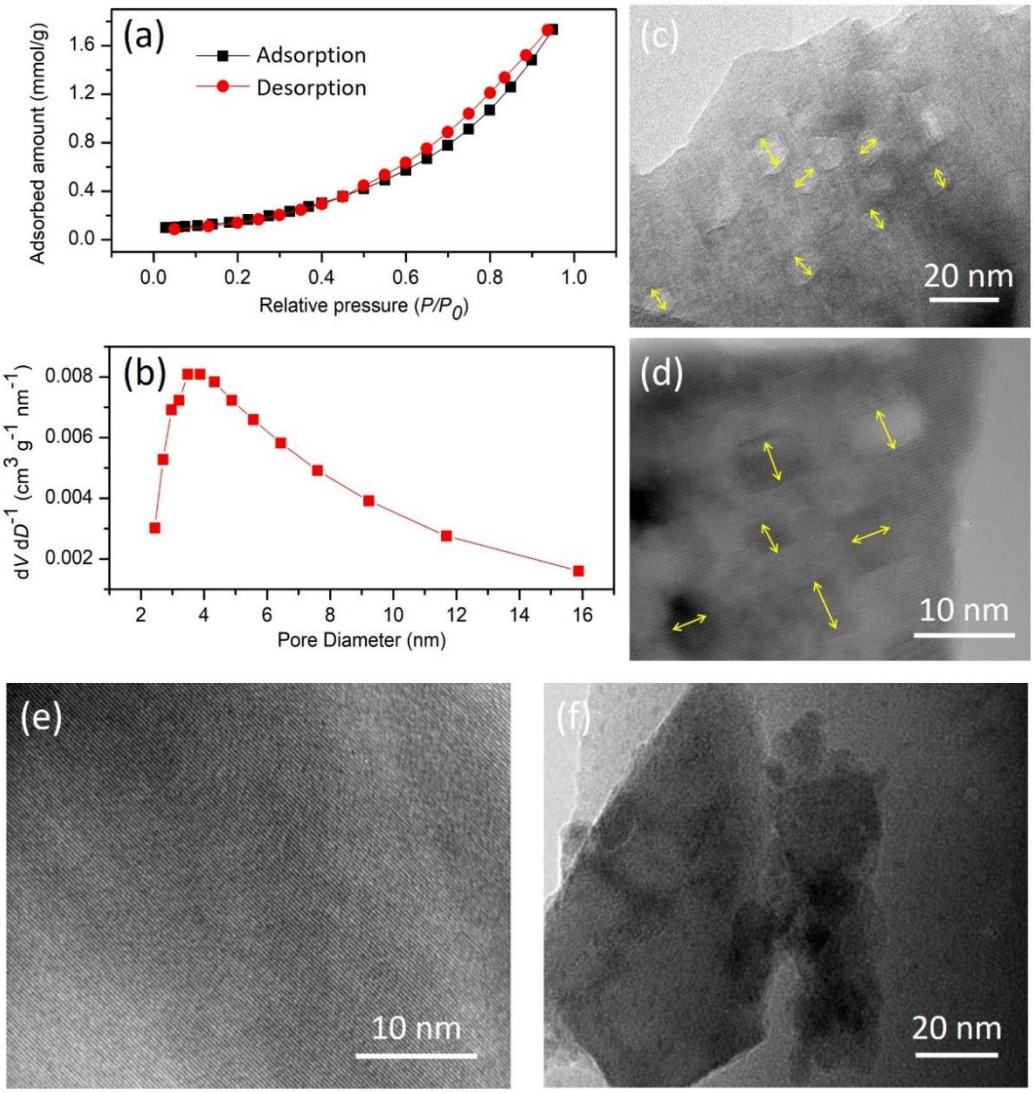


Fig. 6.6 (a) Nitrogen gas absorption-desorption isotherms (b) pore size distribution curve and (c and d) TEM images of 20L BTO F127 sample with nanostructured cuboidal pores (e and f) TEM images of 20L BTO sample without nano scale porosity

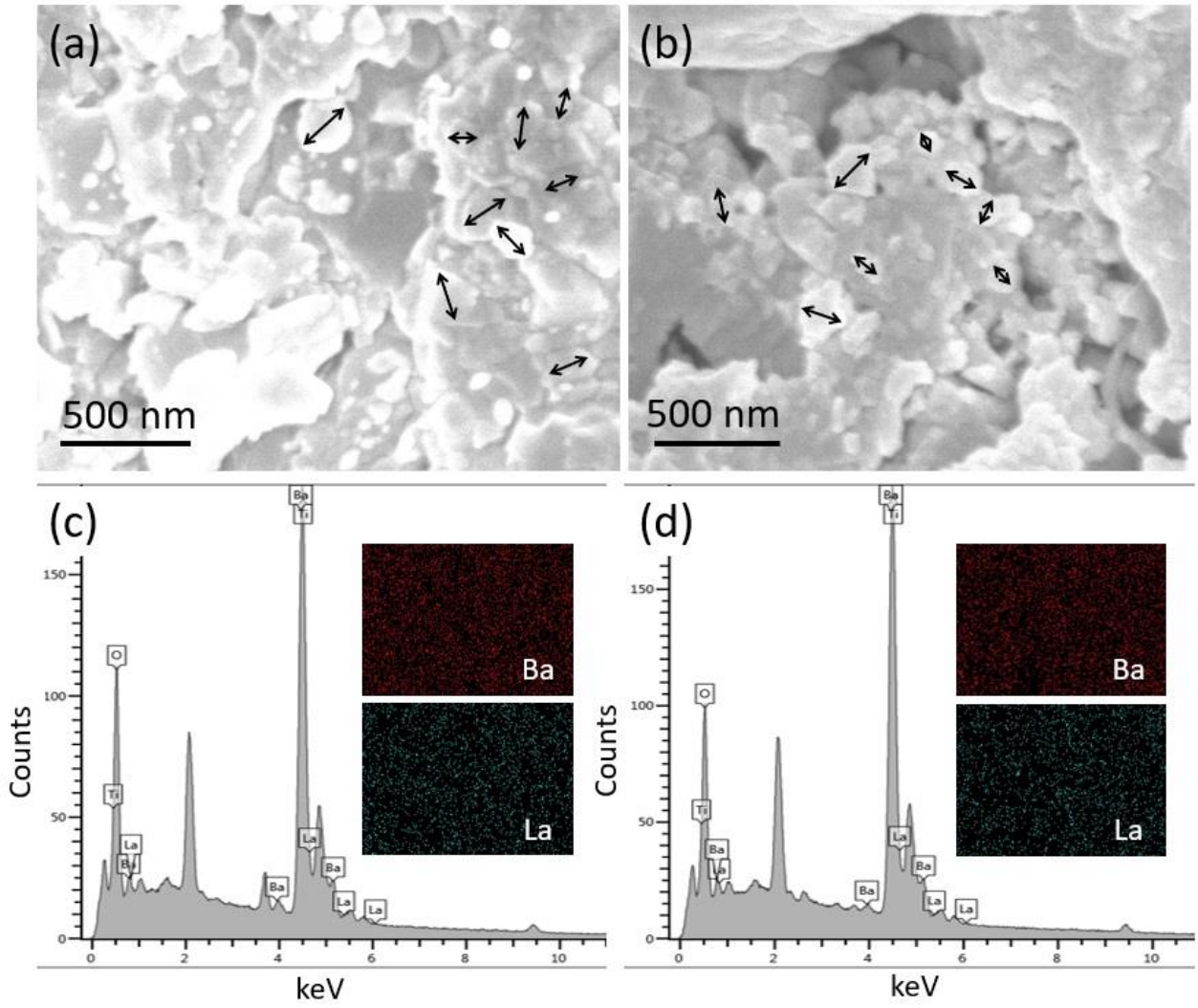


Fig. 6.7 SEM images show grain size and grain boundaries, (a) 20L BTO and (b) 20L BTO F127. The EDS spectra show elemental composition, (c) 20L BTO and (d) 20L BTO F127. The inset figures (i) and (ii) show the distribution of Ba and La, respectively.

The nanostructure of the samples without surfactant (20L BTO) and with surfactant (20L BTO F127) are compared in Fig. 6.7(a and b). The SEM images of the samples show that both have similar grain size of a few hundred nanometres. The size of some grains is indicated in the figures. The grain boundaries of both the samples are also similar. The EDS spectra in Fig. 6.7(c and d) show that both the samples have the same elemental composition. The unlabelled peaks in the EDS spectra are due to Pt coating over the samples. The EDS maps in the inset of

Fig. 6.7(c (i, ii) and d (i, ii)) show the spatial distribution of Ba and La is uniform in both samples. It is clear from the SEM image and EDS maps that the contribution of grain boundaries and point defects to the lattice thermal conductivity would be similar for both samples, with and without surfactant. It is therefore expected that, for the sample 20L BTO F127, the nanostructured cuboidal pores would be the main additional mechanism to reduce the lattice thermal conductivity and enhanced the power factor, although the pores may also hinder the electrical conductivity of the sample slightly.

The electrical conductivity of all the samples increases with measurement temperature which is typical of semiconducting behaviour as shown in Fig. 6.8(a). The electrical conductivity of the sample 20L BTO is significantly higher compared to other samples. This indicates that the carrier concentration and mobility of the sample 20L BTO is in an optimum doping region, and further La-doping does not provide additional benefits. This is consistent with the predictions from the DFT calculations in the earlier section where the DOS calculations suggest that the electrical conductivity improves for 25 at% La doping, but it does not increase further for 50 and 75 a% doping. It is observed that there is no improvement in electrical conductivity of $BaTiO_3$ samples for addition of La in more than 20 atomic percentage. Addition of La to $BaTiO_3$ in more than 25 atomic percentage may be considered as alloying and since $LaTiO_3$ itself a Mott insulator, it reduces the electrical conductivity when it is in alloy form. As we know, the electrical conductivity is linearly proportional to the carrier concentration and the carrier mobility, $\sigma = n\, e\, \mu$, where $e$ is the charge of the electron, $n$ is the carrier concentration and $\mu$ is the carrier mobility. The Hall effect measurement is desirable to separately measure carrier concentration and mobility, but Hall measurements of the samples are not possible due to their low conductivity. The electrical conductivity of the sample 20L BTO F127 is reduced compared to the sample 20L BTO which has the same La doping. This reduction in conductivity is due to

the nanostructured pores which hinder the carrier mobility[30]. The main objective of our research was to examine the effect of nanostructured pores on thermoelectric properties of $BaTiO_3$ which is intrinsically an insulating material. Therefore, the electrical conductivity was improved, and it became *n*-type semiconducting material because of electron doping by adding La in atomic percentage. The electrical conductivity of $BaTiO_3$ can be improved further by using different dopants which was already reported in the literature[48, 52, 55].

The value of the thermopower or Seebeck coefficient of all the samples is negative which means the samples become *n*-type semiconductors after doping. The Seebeck coefficient increases with temperature as shown in Fig. 6.8(b). The sample 20L BTO has the lowest thermopower compared to the other samples. This is logical because the Seebeck coefficient for the doped semiconductor is inversely related to the carrier concentration which can be expressed as $S = \frac{8\pi^2 k_B^2}{3eh^2}\, m^* T\, (\frac{\pi}{3n})^{2/3}$, where, $k_B$ stands for the Boltzmann constant, *e* for electron charge, $h$ refers to Planck's constant, $m^*$ refers to the effective mass of the carrier, $T$ is the absolute temperature, and $n$ is the carrier concentration. There is a huge improvement in the thermopower of the nano-porous sample. The thermopower is doubled for the 20L BTO F127 compared to the sample with the same doping level, but without pores, 20L BTO. The Seebeck coefficient depends on different factors like carrier concentration, diffusion of charge carrier and carrier phonon interaction. There is improvement in Seebeck coefficient of the sample with nanoscale pores though it has same 20 at% La doping like the other sample 20L BTO without pores. It indicates that the carrier concentration is not the factor for improvement of the Seebeck coefficient. Other factors such as diffusion of charge carrier due to temperature gradient and carrier phonon interaction can be responsible for improvement of the Seebeck coefficient. It is suspected that the nanoscale pores are working as a barrier for charge carrier diffusion from the hot side toward the cold side. In addition, the scattering of phonon from nanoscale pores may

change the phonon carrier interaction which can be also responsible for improvement of the Seebeck coefficient. Since the electrical conductivity of 20L BTO reduces due to pores but its thermopower increases significantly, the power factor of the sample is marginally higher than the sample 20L BTO. For the sample 20L BTO F127, the maximum value of the power factor is 16 $\mu W \cdot K^{-2}m$ at 950 K as shown in Fig. 6.8(c).

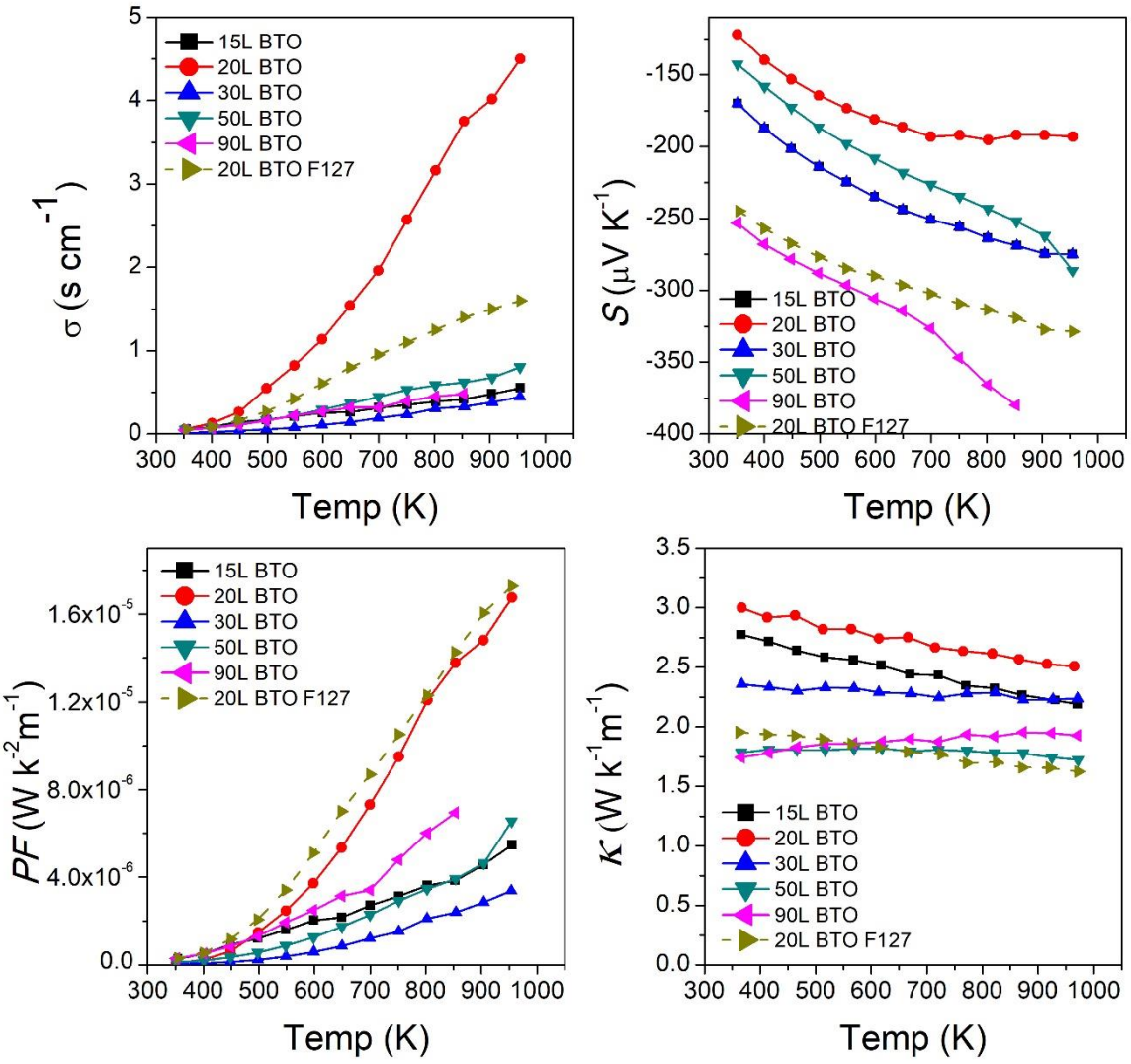


Fig. 6.8 Transport properties of the samples as a function of temperature (a) electrical conductivity σ (s $cm^{-1}$), (b) Seebeck coefficient S (μV $K^{-1}$), (c) Power factor PF (W $K^{-2}$ $m^{-1}$) and (d) Thermal conductivity κ (W $K^{-1}$ $m^{-1}$)

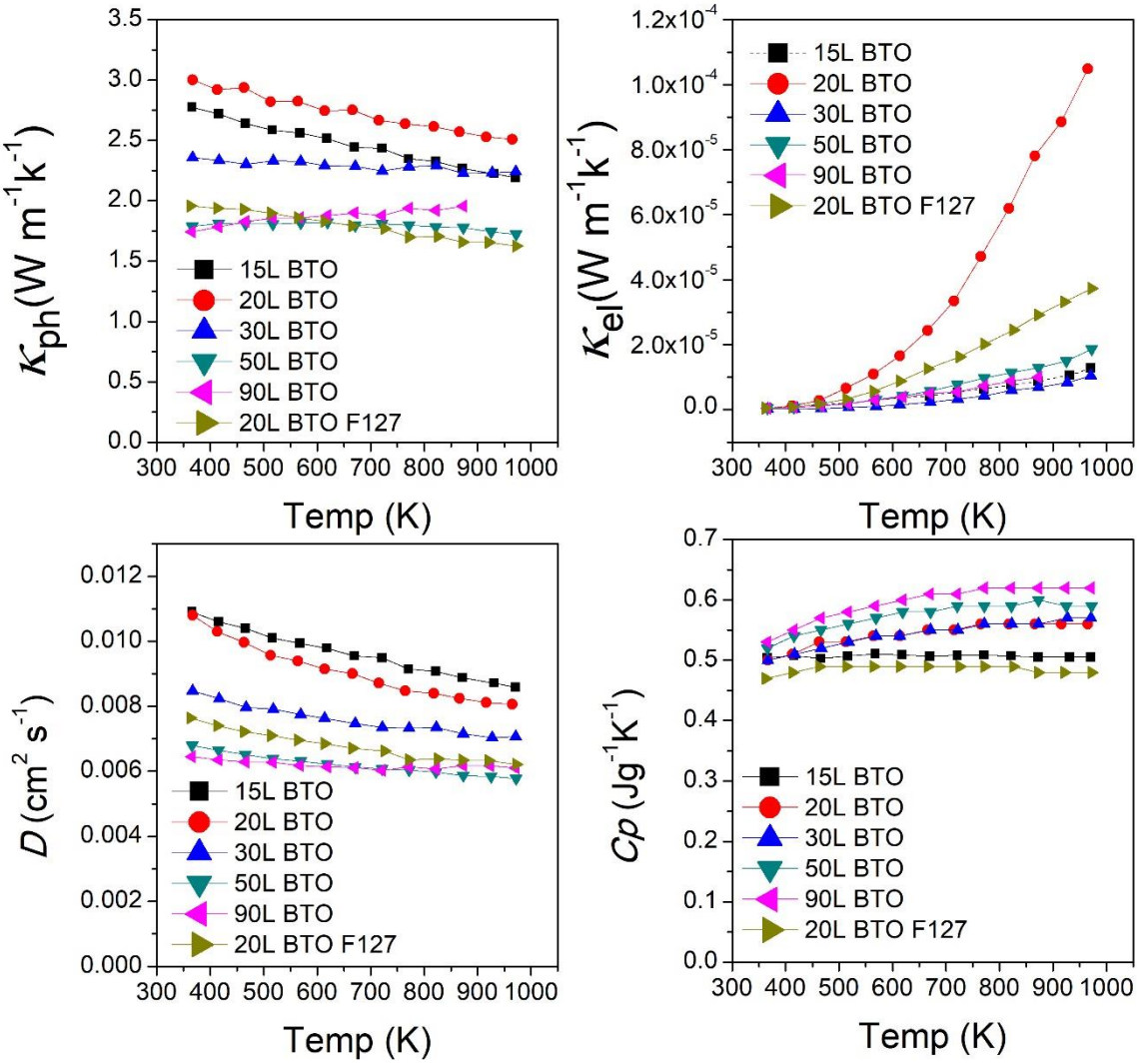


Fig. 6.9 (a) Phonon thermal conductivity $\kappa_{ph}$ (W $m^{-1}$ $k^{-1}$), (b) electrical thermal conductivity $\kappa_{el}$ (W $m^{-1}$ $k^{-1}$), (c) thermal diffusivity D ($cm^2$ $s^{-1}$) and (d) Specific heat capacity Cp (J $g^{-1}$ $K^{-1}$)

The thermal conductivity of all the samples decreases with temperature as shown in Fig. 6.8(d). The sample 20L BTO has the highest thermal conductivity. It can be observed that there is significant decay in the thermal conductivity of the samples 50L BTO and 90L BTO and this is most likely due to charge compensation of the defects in the crystal structure surrounding the La atoms which leads to a reduction in the electronic conductivity. Most importantly, however,

the thermal conductivity of the sample with nanostructured pores (20L BTO F127) is remarkably reduced compared to sample 20L BTO which has the same at% of La doping but without nano porosity. This is attributed to the phonon boundary scattering by the nanostructured pores of the sample in addition to phonon defect scattering by the La atoms[100-101]. Several theoretical studies have shown that structure with pores in the range of a few nanometres to few ten of nanometres can effectively scatter phonons of different wavelengths[22]. The thermal conductivity for the nano-porous sample is less than 2 $W{\cdot}K^{-1}m^{-1}$ at room temperature and it is close to 1.5 $W{\cdot}K^{-1}m^{-1}$ at 950 K.

The thermal conductivity can be divided into two parts, $\kappa_{el}$ which is the thermal conductivity due to the movement of electrons or holes, and $\kappa_{ph}$ which is the thermal conduction by lattice vibration also known as the phonon thermal conductivity. Phonon thermal conductivities and electrical thermal conductivities for each temperature are shown in Fig. 6.9(a and b) respectively. The $\kappa_{ph}$ can be express as, $\kappa_{ph} = \frac{1}{3} C_v V l$, where the heat capacity ($C_v$) at constant volume and the phonon velocity ($V$) are constant, therefore, the $\kappa_{ph}$ mainly relies on the phonon mean free path (MFP) ($l$). The mean free path of phonons in $BaTiO_3$ is on the order of $10^{-8}$ m which is close to the nanometre scale. So, it is possible to scatter the phonon with nano scale pores [26].

The mean free path of the phonons gets reduced due to the nanostructured pores in the sample 20L BTO F127, and this leads to a very low phonon thermal conductivity. To isolate the role of the phonon thermal conductivity, the electronic contribution must first be subtracted. From the Wiedemann-Franz law, the $\kappa_{el}$ is directly proportional to the electrical conductivity, $\sigma$, and temperature, $T$. $\kappa_{el} = LT\sigma$, where $L$ is the proportional constant known as the Lorenz number which is an experimental value. Normally, $L$ is treated as a universal factor with the value of

$2.44 \times 10^{-8}\ \mathrm{W\Omega/K^2}$ for a degenerate semiconductor. In the samples of La-doped $BaTiO_3$, the calculations show that the contribution of $\kappa_{el}$to the total thermal conductivity is insignificant. The experimental thermal conductivity is determined from the thermal diffusivity, specific heat capacity, and density of the material, $\kappa = \alpha\, C_p\, \rho$, where $\alpha, C_p$, and $\rho$ are the thermal diffusivity, heat capacity at constant pressure, and the material density, respectively. The Fig. 6.9(c and d) shows thermal diffusivity and the specific heat capacity of the samples. The thermal diffusivity is a measurement of the rate of heat transfer through the material. The heat transfer in the sample 20L BTO F127 is significantly lower compared to the sample 20L BTO and this may be due to the obstacles introduced by the nanostructured pores. The specific heat capacity is also lower for the sample 20L BTO F127 than others. The value of the specific heat capacity for the samples is close to the theoretical value and it is almost flat with temperature.

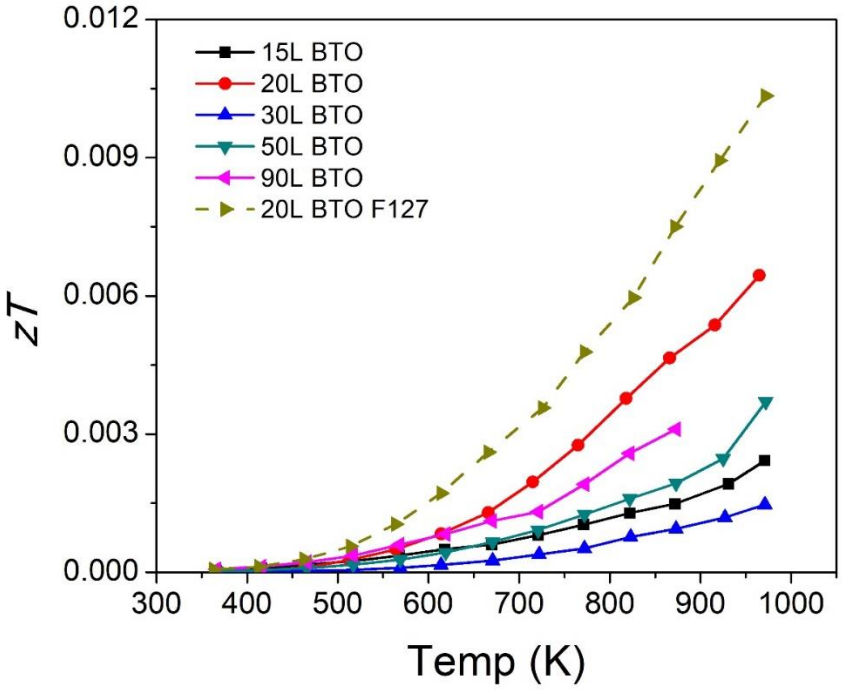


Fig. 6.10 Figure of merit *zT* of the $BaTiO_3$ samples with temperature

The nanoscale pores in the sample 20L BTO F127 reduce its electrical conductivity to some extent. However, the improvement of its thermopower is remarkable because of nanoscale pores. Additionally, the thermal conductivity of the sample is ultra-low. Therefore, there is a significant improvement in the figure of merit of the sample 20L BTO F127 as shown in Fig. 6.10. The figure of merit could be improved further by optimizing the electron doping and retaining the nanoscale porosity in the sample.

## 6.4 Conclusion

The electrical conductivity of $BaTiO_3$ has been improved by optimizing the doping of La in atomic percentages and causing the samples to become *n*-type semiconductor materials. For further improvement of transport properties, a nano porous architecture has been introduced in the sample 20L BTO F127 using the F127 surfactant during the powder synthesis process. The thermopower of the sample has been enhanced to more than double compared to the sample without porosity (20L BTO). The main achievement of the experiments is the suppression of the phonon propagation by nanostructured rectangular-prismatic pores which lead to a very low phonon thermal conductivity of 1.5 $W \cdot K^{-1}m^{-1}$ at 950K in the sample 20L BTO F127. There is a reduction in the electrical conductivity of the sample 20L BTO F127 due to the nano scale pores. However, the improvement of thermopower is more significant than the reduction of electrical conductivity. Therefore, the power factor of the sample 20L BTO F127 is higher than the sample without porosity 20L BTO. In addition, the reduction of thermal conductivity is remarkable because of nanoscale pores into the sample 20L BTO F127. The theoretical studies showed that the reduction in thermal conductivity is more prominent than the reduction in electrical conductivity because of nanoscale porosity and it leads to an overall improvement in

figure on merit[102-103]. This promising novel strategy of suppressing phonon thermal conductivity can be applied to other thermoelectric materials also to improve the figure of merit.

The result presented in this chapter has been published in the journal Advanced Electronic Materials by me as a first author. Sheik Md. Kazi Nazrul Islam, David Corie and Yaser Rehman helped to conduct experiments and to result analysis. The DFT calculation was done by Frank Yun. Abdul hakim Bake, K. Konstantinov and A. Alowasheeir contributed to manuscript writing. Md. Shahriar A. Hossain, Yusuke Yamauchi and Xiaolin Wang supervised and revised the manuscript.

*"Significant Reduction in Thermal Conductivity and Improved Thermopower of Electron-Doped $Ba_{1-x}La_xTiO_3$ with Nanostructured Rectangular Pores"*; Ahmed, A. J., Cortie, D. L., Yun, F. F., Rahman, Y., Nazrul, S. M. K., Bake, A., Konstantinov, K., Hossain, M. S. A., Alowasheeir, A., Yamauchi, Y., Wang, X.; Advanced Electronic Materials. 2021, 7, 2001044. https://doi.org/10.1002/aelm.202001044

# 7. Discussion and Conclusion

Electron doped transition metal oxide, $Sr_{1-x}La_xTiO_3$ and $Ba_{1-x}La_xTiO_3$ powders with nanoscale porosities were synthesized successfully by using the polymeric micelles self-assembly method followed by calcination at 600$^o$C for 10 min. The commercially available poly (ethylene oxide)-*b*-poly (propylene oxide)-*b*-poly (ethylene oxide) type triblock copolymer, Pluronic F127 ($PEO_{106}PPO_{70}PEO_{106}$), was used as the soft-template for nano scale pores formation. In the next stage, these nano porous powders were rapidly solidified using the spark plasma sintering (SPS) technique. The sintering conditions such as temperature, pressure, holding time, heating, and cooling rate were optimized to prepare highly dense bulk samples with nanocrystalline and nanoscale porosity. The sintering temperature, pressure and holding time of SPS were 1150$^o$c, 60 MPa and 15 min respectively and relative density of samples was more than 90 % of theoretical value.

X-ray diffraction (XRD) analysis confirms the crystallinity of the samples and it also confirms that there is no trace of secondary peak in the XRD patterns. The XRD peaks shifting towards the higher diffraction angle and decrease of lattice parameter confirm that $La^{3+}$ ions successfully replace $Sr^{2+}$ or $Ba^{2+}$ ions in the A site of $ABO_3$ crystal system. Atomic resolution scanning transmission electron microscopy images and energy dispersive X-ray spectrometry (EDS) also prove the same, substitutional doping of La into the lattice of $ABO_3$ crystal system. The Brunauer–Emmett–Teller (BET) analysis, scanning electron microscopy (SEM) and transmission electron microscopy (TEM) images reveal that the samples have grain boundaries of few hundred nanometres, most likely because of short holding period of spark plasma sintering process. The analyses also reveal that the samples have porosities of few nanometres

within the crystal lattice because of using surfactant F127 as soft template during the powder preparation process.

In chapter 4, Electron doped $Sr_{0.8}La_{0.2}TiO_3$ bulk samples with different amount of F127 surfactant were fabricated and investigated successfully to observe the effect of nano porosity on thermoelectric properties. It was observed that the Seebeck coefficient increases, while the thermal conductivity reduces substantially by introducing porosity into the bulk sample because of the carrier and phonon scattering by the nanoscale pores. Therefore, there is an overall enhancement in power factor and figure of merit. The sample, $S_{0.8}L_{0.2}TiO_3$ with 600mg of F127 (SLTO 600F127), exhibited the highest value of the power factor, 1.14 $mW{\cdot}m^{-1}K^{-2}$ at 647 K, which is 35% higher than the sample $S_{0.8}L_{0.2}TiO_3$ without porosity (SLTO 0F127). The same sample (SLTO 600F127) also exhibited the maximum value of the *zT* is 0.32 at 968 K with an average enhancement of 62% in *zT* in comparison to the sample without porosity (SLTO 0F127).

In chapter 5, the carrier concentration was optimized with La doping in six different atomic percentages (5, 15, 18, 20, 22 and 25 at%) into $SrTiO_3$ bulk sample with nano-scale porosity. The porosity of samples was kept similar by adding equal amount of surfactant F127 during the powder preparation of $SrTiO_3$. The sample with 22at% La doping (22La-STO) exhibits highest electrical conductivity compared to other samples throughout the temperature range. On the other hand, the lattice thermal conductivity of all the samples were same because of similar nanostructure of the samples and the contribution of electrical thermal conductivity was insignificant in total thermal conductivity. Due to this dual mechanism, the sample with 22at% La doping showed high power factor and figure of merit at low temperature which is an essential improvement for metal oxide based thermoelectric material. The sample exhibited power factor

of around 1mW/mK$^2$ from 550 K to 800 K. And the value of dimensionless figure of merit, *zT* is 0.26 ± 0.06 at 850K.

In chapter 6, The electrical conductivity of $BaTiO_3$ was improved by optimizing the doping of La in atomic percentages and causing the samples to become *n*-type semiconductor materials. For further improvement of transport properties, a nano porous architecture was introduced in the sample $Ba_{0.8}La_{0.2}TiO_3$ using soft template F127 surfactant (20L BTO F127) during the powder synthesis process. The Seebeck or thermopower of the sample was enhanced to more than double compared to the sample without porosity (20L BTO). The main achievement of the experiments was the suppression of the phonon propagation by nanostructured rectangular-prismatic pores which lead to a very low phonon thermal conductivity of 1.5 $W{\cdot}K^{-1}m^{-1}$ at 950K in the sample 20L BTO F127.

Transport properties measurement of La doped $SrTiO_3$ and $BaTiO_3$ samples shows that there is a significant improvement in electrical conductivity of samples, and they are become *n*-type semiconductor, due to electron doping optimization. On the other hand, the Seebeck coefficient or thermopower of the samples with nano scale porosities improves greatly, but the electrical conductivity reduces marginally, and this may be due to decrease in carrier mobility by the nano porosities. However, there is a significant enhancement in power factor of samples because of combined effect of electron doping optimization and introduce of nano scale porosity in the bulk samples.

The conventional thermoelectric materials have high figure to merit near room temperature due to their low lattice thermal conductivity and high electrical conductivity. However, these are not chemically and mechanically stable at high temperature due to low melting point. On the other hand, the main advantage of oxide thermoelectric materials is robustness at high operating

temperature due to their high melting point. However, the main drawback of oxide based thermoelectric materials is their high lattice thermal conductivity.

The main outcome of the thesis was to reduce lattice thermal conductivity of perovskite based thermoelectric materials, $SrTiO_3$ and $BaTiO_3$ by introducing nano scale pores in crystal structure of bulk samples. The phonon scattering by the nano scale pores could be the main cause of reduction in lattice thermal conductivity in addition to point defect due to substitutional doping of La atoms and grain boundaries between nanocrystals. Therefore, there is a substantial improvement of figure of merit of these thermoelectric materials due to the dual mechanism of electron doping optimization and introduction of nano scale pores into the crystal structure of bulk samples. The further study can be done to understand the interaction of phonon of different wavelengths with nano pores of different scales. The clearer understanding of this promising mechanism will help to implement it in association of other thermal conductivity reduction mechanisms like nano sized metal or graphene inclusion for further improvement of metal oxide as well as other thermoelectric materials.

# References


1. Ohta, H., Thermoelectrics based on strontium titanate. *Materials Today* **2007,** *10* (10), 44-49.

2. Zhang, Y.; Feng, B.; Hayashi, H.; Chang, C.-P.; Sheu, Y.-M.; Tanaka, I.; Ikuhara, Y.; Ohta, H., Double thermoelectric power factor of a 2D electron system. *Nature Communications* **2018,** *9* (1), 2224.

3. Zhu, F.-f.; Chen, W.-j.; Xu, Y.; Gao, C.-l.; Guan, D.-d.; Liu, C.-h.; Qian, D.; Zhang, S.-C.; Jia, J.-f., Epitaxial growth of two-dimensional stanene. *Nature Materials* **2015,** *14*, 1020-1020.

4. Islam, S. M. K. N.; Li, M.; Aydemir, U.; Shi, X.; Chen, L.; Snyder, G. J.; Wang, X., Giant enhancement of the figure-of-merit over a broad temperature range in nano-boron incorporated $Cu_2Se$. *Journal of Materials Chemistry A* **2018,** *6* (38), 18409-18416.

5. Zhang, X.; Zhao, L.-D., Thermoelectric materials: Energy conversion between heat and electricity. *Journal of Materiomics* **2015,** *1* (2), 92-105.

6. He, J.; Tritt, T. M., Advances in thermoelectric materials research: Looking back and moving forward. *Science* **2017,** *357* (6358).

7. technologies, P. C. e. TEC-Chip (An innovative Thermo-Electric Converter (TEC) based on metal-dielectric-semiconductor-metal structures). https://prometeon.it/advanced-clean-technologies-tech-chip/.

8. UK, E. T. N. *Thermoelectric Roadmap* UK May, 2018

9. Vining, C. B., An inconvenient truth about thermoelectrics. *Nature Materials* **2009,** *8*, 83.

10. Ohtaki, M., Recent aspects of oxide thermoelectric materials for power generation from mid-to-high temperature heat source. *Journal of the Ceramic Society of Japan* **2011,** *119* (1395), 770-775.

11. Wang, H.; Su, W.; Liu, J.; Wang, C., Recent development of n-type perovskite thermoelectrics. *Journal of Materiomics* **2016,** *2* (3), 225-236.

12. Liang, Z.; Ning, L.; Hui-Qiong, W.; Yufeng, Z.; Fei, R.; Xia-Xia, L.; Ya-Ping, L.; Xiao-Dan, W.; Zheng, H.; Yang, D.; Hao, Y.; Jin-Cheng, Z., Tuning the thermal conductivity of strontium titanate through annealing treatments. *Chinese Physics B* **2017,** *26* (1), 016602.

13. Materials Science and Engineering, N. U. Brife history of thermoeleectrics. http://thermoelectrics.matsci.northwestern.edu/thermoelectrics/history.html.

14. Sootsman, J. R.; Chung, D. Y.; Kanatzidis, M. G., New and Old Concepts in Thermoelectric Materials. *Angewandte Chemie International Edition* **2009,** *48* (46), 8616-8639.

15. Yin, Y.; Tudu, B.; Tiwari, A., Recent advances in oxide thermoelectric materials and modules. *Vacuum* **2017,** *146*, 356-374.

16. &, Y. F. X. J. E. G. B. K.; Lu, C. Z. I. F. N., Metal oxides for thermoelectric power generation and beyond. *Adv Compos Hybrid Mater* **2018,** *2018* (1), 114-126.

17. Sonne, M.; Van Nong, N.; He, Z.; Pryds, N.; Linderoth, S., Improvement of Niobium Doped SrTiO3 by Nanostructuring. 2010; pp 175-178.

18. Snyder, G. J.; Toberer, E. S., Complex thermoelectric materials. *Nature Materials* **2008,** *7*, 105.

19. Malta, D. M.; von Windheim, J. A.; Wynands, H. A.; Fox, B. A., Comparison of the electrical properties of simultaneously deposited homoepitaxial and polycrystalline diamond films. *Journal of Applied Physics* **1995,** *77* (4), 1536-1545.

20. Kim, H.-S.; Gibbs, Z. M.; Tang, Y.; Wang, H.; Snyder, G. J., Characterization of Lorenz number with Seebeck coefficient measurement. *APL Materials* **2015,** *3* (4), 041506.

21. Sun, J.; Singh, D. J., Thermoelectric properties of n-type SrTiO3. *APL Materials* **2016,** *4* (10), 104803.

22. Lee, H.; Vashaee, D.; Wang, D. Z.; Dresselhaus, M. S.; Ren, Z. F.; Chen, G., Effects of nanoscale porosity on thermoelectric properties of SiGe. *Journal of Applied Physics* **2010,** *107* (9), 094308.

23. Lu, Z.; Zhang, H.; Lei, W.; Sinclair, D. C.; Reaney, I. M., High-Figure-of-Merit Thermoelectric La-Doped A-Site-Deficient SrTiO3 Ceramics. *Chemistry of Materials* **2016,** *28* (3), 925-935.

24. Boston, R.; Schmidt, W. L.; Lewin, G. D.; Iyasara, A. C.; Lu, Z.; Zhang, H.; Sinclair, D. C.; Reaney, I. M., Protocols for the Fabrication, Characterization, and Optimization of n-Type Thermoelectric Ceramic Oxides. *Chemistry of Materials* **2017,** *29* (1), 265-280.

25. Kikuchi, A.; Okinaka, N.; Akiyama, T., A large thermoelectric figure of merit of La-doped SrTiO3 prepared by combustion synthesis with post-spark plasma sintering. *Scripta Materialia* **2010,** *63* (4), 407-410.

26. Park, K.; Son, J. S.; Woo, S. I.; Shin, K.; Oh, M.-W.; Park, S.-D.; Hyeon, T., Colloidal synthesis and thermoelectric properties of La-doped SrTiO3 nanoparticles. *Journal of Materials Chemistry A* **2014,** *2* (12), 4217-4224.

27. Wang, Y.; Fan, H. J., Sr1−xLaxTiO3 nanoparticles: Synthesis, characterization and enhanced thermoelectric response. *Scripta Materialia* **2011,** *65* (3), 190-193.

28. Liu, D.; Zhang, Y.; Kang, H.; Li, J.; Chen, Z.; Wang, T., Direct preparation of La-doped SrTiO3 thermoelectric materials by mechanical alloying with carbon burial sintering. *Journal of the European Ceramic Society* **2018,** *38* (2), 807-811.

29. Qin, M.; Gao, F.; Dong, G.; Xu, J.; Fu, M.; Wang, Y.; Reece, M.; Yan, H., Microstructure characterization and thermoelectric properties of Sr0.9La0.1TiO3 ceramics with nano-sized Ag as additive. *Journal of Alloys and Compounds* **2018,** *762*, 80-89.

30. Park, C.-S.; Han, W.; Shim, D. I.; Cho, H. H.; Park, H.-H., The Effect of Mesoporous Structure on the Thermoelectric Properties of Nonstoichiometric La-Doped SrTiO3. *Journal of The Electrochemical Society* **2016,** *163* (6), E155-E158.

31. Park, C.-S.; Hong, M.-H.; Cho, H. H.; Park, H.-H., Enhancement of Seebeck coefficient of mesoporous SrTiO3 with V-group elements V, Nb, and Ta substituted for Ti. *Journal of the European Ceramic Society* **2018,** *38* (1), 125-130.

32. Wang, N.; Chen, H.; He, H.; Norimatsu, W.; Kusunoki, M.; Koumoto, K., Enhanced thermoelectric performance of Nb-doped SrTiO3 by nano-inclusion with low thermal conductivity. *Scientific Reports* **2013,** *3*, 3449.

33. Da-Quan, L.; Yu-Wei, Z.; Hui-Jun, K.; Jin-Ling, L.; Xiong, Y.; Tong-Min, W., Effect of Nb doping on microstructures and thermoelectric properties of SrTiO 3 ceramics. *Chinese Physics B* **2018,** *27* (4), 047205.

34. Wang, J.; Zhang, B.-Y.; Kang, H.-J.; Li, Y.; Yaer, X.; Li, J.-F.; Tan, Q.; Zhang, S.; Fan, G.-H.; Liu, C.-Y.; Miao, L.; Nan, D.; Wang, T.-M.; Zhao, L.-D., Record high thermoelectric performance in bulk SrTiO3 via nano-scale modulation doping. *Nano Energy* **2017,** *35*, 387-395.

35. Li, E.; Wang, N.; He, H.; Chen, H., Improved Thermoelectric Performances of SrTiO3 Ceramic Doped with Nb by Surface Modification of Nanosized Titania. *Nanoscale Research Letters* **2016,** *11* (1), 188.

36. Liu, J.; Wang, C. L.; Li, Y.; Su, W. B.; Zhu, Y. H.; Li, J. C.; Mei, L. M., Influence of rare earth doping on thermoelectric properties of SrTiO3 ceramics. *Journal of Applied Physics* **2013,** *114* (22), 223714.

37. Srivastava, D.; Norman, C.; Azough, F.; Schäfer, M. C.; Guilmeau, E.; Freer, R., Improving the thermoelectric properties of SrTiO3-based ceramics with metallic inclusions. *Journal of Alloys and Compounds* **2018,** *731*, 723-730.

38. Han, J.; Sun, Q.; Song, Y., Enhanced thermoelectric properties of La and Dy co-doped, Sr-deficient SrTiO3 ceramics. *Journal of Alloys and Compounds* **2017,** *705* (Supplement C), 22-27.

39. Han, J.; Sun, Q.; Li, W.; Song, Y., Microstructure and thermoelectric properties of La0.1Dy0.1SrxTiO3 ceramics. *Ceramics International* **2017,** *43* (7), 5557-5563.

40. Ke-Xian, W.; Jun, W.; Yan, L.; Tao, Z.; Xiao-Huan, W.; Jian-Bo, L.; Zheng, C.; Wen-Jing, S.; Xinba, Y., Enhancement of thermoelectric properties of SrTiO 3 /LaNb–SrTiO 3 composite by different doping levels. *Chinese Physics B* **2018,** *27* (4), 048401.

41. Teranishi, T.; Ishikawa, Y.; Hayashi, H.; Kishimoto, A.; Katayama, M.; Inada, Y., Thermoelectric Efficiency of Reduced SrTiO3 Ceramics Modified with La and Nb. *Journal of the American Ceramic Society* **2013,** *96* (9), 2852-2856.

42. Mikio, I.; Naoto, O., Transport properties of thermoelectric SrTiO 3 synthesized by polymerized complex method and spark plasma sintering. *Journal of Physics: Conference Series* **2010,** *232* (1), 012005.

43. Kovalevsky, A. V.; Aguirre, M. H.; Populoh, S.; Patricio, S. G.; Ferreira, N. M.; Mikhalev, S. M.; Fagg, D. P.; Weidenkaff, A.; Frade, J. R., Designing strontium titanate-based thermoelectrics: insight into defect chemistry mechanisms. *Journal of Materials Chemistry A* **2017,** *5* (8), 3909-3922.

44. Kikuchi, A.; Zhang, L.; Okinaka, N.; Tosho, T.; Akiyama, T., Optimization of Sintering Temperature for Maximizing Dimensionless Figure of Merit of La-Doped Strontium Titanate Thermoelectric Material in the Combination of Combustion Synthesis with Post Spark Plasma Sintering. *MATERIALS TRANSACTIONS* **2010,** *51* (10), 1919-1922.

45. Zhao, W.; Liu, Z.; Sun, Z.; Zhang, Q.; Wei, P.; Mu, X.; Zhou, H.; Li, C.; Ma, S.; He, D.; Ji, P.; Zhu, W.; Nie, X.; Su, X.; Tang, X.; Shen, B.; Dong, X.; Yang, J.; Liu, Y.; Shi, J., Superparamagnetic enhancement of thermoelectric performance. *Nature* **2017,** *549*, 247.

46. Suzuki , N.; Jiang , X.; Salunkhe, R. R.; Osada , M.; Yamauchi , Y., Chemical Preparation of Ferroelectric Mesoporous Barium Titanate Thin Films: Drastic Enhancement of Curie Temperature Induced by Mesopore-Derived Strain. *Chemistry – A European Journal* **2014,** *20* (36), 11283-11286.

47. Fu, D.; Itoh, M. In *Role of Ca off-Centering in Tuning Ferroelectric Phase Transitions in Ba(Zr,Ti)O3System*, 2015.

48. Zhang, R.-z.; Hu, X.-y.; Guo, P.; Wang, C.-l., Thermoelectric transport coefficients of n-doped CaTiO3, SrTiO3 and BaTiO3: A theoretical study. *Physica B: Condensed Matter* **2012,** *407* (7), 1114-1118.

49. Wu, T.; Gao, P., Development of Perovskite-Type Materials for Thermoelectric Application. *Materials (Basel)* **2018,** *11* (6), 999.

50. Tomofumi YAMADA, R. A., Takeshi YOKOTA and Manabu GOMI, High-temperature thermoelectric properties

of $BaFexTi_{1-x}O_{3-}$ ceramics. *J. Ceram. Soc. Jpn.* **2013,** *121* (8), 706-709.

51. Mallada, C.; Menéndez, J. L.; Dura, O. J.; López de la Torre, M. A.; Menéndez, R.; Santamaría, R., Spark plasma sintered BaTiO3/graphene composites for thermoelectric applications. *J. Eur. Ceram. Soc.* **2017,** *37* (12), 3741-3746.

52. Xiao, X.; Widenmeyer, M.; Xie, W.; Zou, T.; Yoon, S.; Scavini, M.; Checchia, S.; Zhong, Z.; Hansmann, P.; Kilper, S.; Kovalevsky, A.; Weidenkaff, A., Tailoring the structure and thermoelectric properties of BaTiO3via Eu2+ substitution. *Physical Chemistry Chemical Physics* **2017,** *19* (21), 13469-13480.

53. Muta, H.; Kurosaki, K.; Yamanaka, S., Thermoelectric properties of doped BaTiO3–SrTiO3 solid solution. *J. Alloys Compd.* **2004,** *368* (1), 22-24.

54. Anno, H.; Yamaguchi, K.; Nakabayashi, T.; Kurokawa, H.; Akagi, F.; Hojo, M.; Toshima, N., Thermoelectric properties of conducting polyaniline/BaTiO3nanoparticle composite films. *IOP Conference Series: Materials Science and Engineering* **2011,** *18* (14), 142003.

55. Suchanicz, J.; Czaja, P.; Kluczewska, K.; Czternastek, H.; Sokolowski, M.; Węgrzyn, A., The Influence of Pb(Mg1/3Nb2/3)O3-doping on the thermoelectric properties of BaTiO3 ceramics. *Phase Transitions* **2018,** *91* (9-10), 1036-1043.

56. Roy, P.; Waghmare, V.; Maiti, T., Environmentally friendly BaxSr2−xTiFeO6 double perovskite with enhanced thermopower for high temperature thermoelectric power generation. *RSC Advances* **2016,** *6* (60), 54636-54643.

57. Nasir Khan, M.; Kim, H.-T.; Minami, H.; Uwe, H., Thermoelectric properties of niobium doped hexagonal barium titanate. *Materials Letters* **2001,** *47* (1), 95-101.

58. Kolodiazhnyi, T.; Petric, A.; Niewczas, M.; Bridges, C.; Safa-Sefat, A.; Greedan, J. E., Thermoelectric power, Hall effect, and mobility of n-type ${\mathrm{BaTiO}}_{3}$. *Physical Review B* **2003,** *68* (8), 085205.

59. Wang, L.; Yamauchi, Y., Block Copolymer Mediated Synthesis of Dendritic Platinum Nanoparticles. *Journal of the American Chemical Society* **2009,** *131* (26), 9152-9153.

60. Kabanov, A. V.; Batrakova, E. V.; Alakhov, V. Y., Pluronic® block copolymers as novel polymer therapeutics for drug and gene delivery. *Journal of Controlled Release* **2002,** *82* (2), 189-212.

61. Li, Y.; Bastakoti, B. P.; Yamauchi, Y., Research Update: Triblock copolymers as templates to synthesize inorganic nanoporous materials. *APL Materials* **2016,** *4* (4), 040703.

62. Li, Y.; Bastakoti Bishnu, P.; Imura, M.; Hwang Soo, M.; Sun, Z.; Kim Jung, H.; Dou Shi, X.; Yamauchi, Y., Synthesis of Mesoporous TiO2/SiO2 Hybrid Films as an Efficient Photocatalyst by Polymeric Micelle Assembly. *Chemistry – A European Journal* **2014,** *20* (20), 6027-6032.

63. Guillon, O.; Gonzalez-Julian, J.; Dargatz, B.; Kessel, T.; Schierning, G.; Räthel, J.; Herrmann, M., Field-Assisted Sintering Technology/Spark Plasma Sintering: Mechanisms, Materials, and Technology Developments. *Advanced Engineering Materials* **2014,** *16* (7), 830-849.

64. Shang, P.-P.; Zhang, B.-P.; Li, J.-F.; Ma, N., Effect of sintering temperature on thermoelectric properties of La-doped SrTiO3 ceramics prepared by sol–gel process and spark plasma sintering. *Solid State Sciences* **2010,** *12* (8), 1341-1346.

65. Maca, K.; Pouchly, V.; Shen, Z., TWO-STEP SINTERING AND SPARK PLASMA SINTERING OF Al2O3, ZrO2 AND SrTiO3 CERAMICS. *Integrated Ferroelectrics* **2008,** *99* (1), 114-124.

66. Li, L.; Liu, Y.; Qin, X.; Li, D.; Zhang, J.; Song, C.; Wang, L., Enhanced thermoelectric performance of highly dense and fine-grained (Sr1−xGdx)TiO3−δ ceramics synthesized by sol–gel process and spark plasma sintering. *Journal of Alloys and Compounds* **2014,** *588*, 562-567.

67. Noriyuki OKINAKA, L. Z., Tomohiro AKIYAMA Thermoelectric Properties of Rare Earth-doped SrTiO3 Using Combination of Combustion Synthesis (CS) and Spark Plasma Sintering (SPS). *ISIJ International* **2010,** *50* (9), 1300–1304.

68. Fagerlund, G., Determination of specific surface by the BET method. *Matériaux et Construction* **1973,** *6* (3), 239-245.

69. Anovitz, L. M.; Cole, D. R., Characterization and Analysis of Porosity and Pore Structures. *Reviews in Mineralogy and Geochemistry* **2015,** *80* (1), 61-164.

70. Kohn, W.; Sham, L. J., Self-consistent equations including exchange and correlation effects. *Phys. Rev.* **1965,** *140*, A1133-A1138.

71. Hohenberg, P.; Kohn, W., Inhomogeneous electron gas. *Phys. Rev.* **1964,** *136*, B864-B871.

72. Clark, S. J.; Segall, M. D.; Pickard, C. J.; Hasnip, P. J.; Probert, M. J.; Refson, K.; Payne, M. C., First principles methods using CASTEP. *Z. Kristall.* **2005,** *220*, 567-570.

73. Perdew, J. P.; Burke, K.; Ernzerhof, M., Generalized Gradient Approximation Made Simple. *Physical Review Letters* **1996,** *77* (18), 3865-3868.

74. Pfrommer, B. G.; Cote, M.; Louie, S. G.; Cohen, M. L., Relaxation of crystals with the quasi-Newton method. *J. Comput. Phys.* **1997,** *131*, 233-240.

75. Zhao, L.; Islam, S. M. K. N.; Wang, J.; Cortie, D. L.; Wang, X.; Cheng, Z.; Wang, J.; Ye, N.; Dou, S.; Shi, X.; Chen, L.; Snyder, G. J.; Wang, X., Significant enhancement of figure-of-merit in carbon-reinforced Cu2Se nanocrystalline solids. *Nano Energy* **2017,** *41* (Supplement C), 164-171.

76. Tang, J.; Wang, H.-T.; Lee, D. H.; Fardy, M.; Huo, Z.; Russell, T. P.; Yang, P., Holey Silicon as an Efficient Thermoelectric Material. *Nano Letters* **2010,** *10* (10), 4279-4283.

77. Li, M.; Cortie, D. L.; Liu, J.; Yu, D.; Islam, S. M. K. N.; Zhao, L.; Mitchell, D. R.; Mole, R. A.; Cortie, M. B.; Dou, S., Ultra-high thermoelectric performance in graphene incorporated Cu2Se: Role of mismatching phonon modes. *Nano energy* **2018,** *53*, 993-1002.

78. Li, M.; Islam, S. M. K. N.; Dou, S.; Wang, X., Significantly enhanced figure-of-merit in graphene nanoplate incorporated Cu2Se fabricated by spark plasma sintering. *Journal of Alloys and Compounds* **2018,** *769*, 59-64.

79. Shabbir, B.; Huang, H.; Yao, C.; Ma, Y.; Dou, S.; Johansen, T. H.; Hosono, H.; Wang, X., Evidence for superior current carrying capability of iron pnictide tapes under hydrostatic pressure. *Physical Review Materials* **2017,** *1* (4), 044805.

80. Shabbir, B.; Wang, X.; Ma, Y.; Dou, S.; Yan, S.-S.; Mei, L.-M., Study of flux pinning mechanism under hydrostatic pressure in optimally doped (Ba, K) Fe 2 As 2 single crystals. *Scientific reports* **2016,** *6*, 23044.

81. Shen, H.; Lu, Y.; Wang, Y.; Pan, Z.; Cao, G.; Yan, X.; Fang, G., Low temperature hydrothermal synthesis of SrTiO3 nanoparticles without alkali and their effective photocatalytic activity. *Journal of Advanced Ceramics* **2016,** *5* (4), 298-307.

82. Park, N.-H.; Dang, F.; Wan, C.; Seo, W.-S.; Koumoto, K., Self-originating two-step synthesis of core–shell structured La-doped SrTiO3 nanocubes. *Journal of Asian Ceramic Societies* **2013,** *1* (1), 35-40.

83. Stojilovic, N., Using Cu Kα1/Kα2 Splitting and a Powder XRD System To Discuss X-ray Generation. *Journal of Chemical Education* **2018,** *95* (4), 598-600.

84. Kim, H. S.; Liu, W.; Chen, G.; Chu, C.-W.; Ren, Z., Relationship between thermoelectric figure of merit and energy conversion efficiency. *Proceedings of the National Academy of Sciences* **2015,** *112* (27), 8205-8210.

85. Snyder, G. J., Application of the compatibility factor to the design of segmented and cascaded thermoelectric generators. *Applied Physics Letters* **2004,** *84* (13), 2436-2438.

86. Ahmed, A. J.; Khan, S. N. In *Performance evaluation of solar panel and proposed new algorithm of solar tracking system*, 2nd International Conference on Green Energy and Technology, 5-6 Sept. 2014; 2014; pp 9-13.

87. Li, Y.; Hou, Q.-Y.; Wang, X.-H.; Kang, H.-J.; Yaer, X.; Li, J.-B.; Wang, T.-M.; Miao, L.; Wang, J., First-principles calculations and high thermoelectric performance of La–Nb doped SrTiO3 ceramics. *Journal of Materials Chemistry A* **2019,** *7* (1), 236-247.

88. Ahmed, A. J.; Nazrul Islam, S. M. K.; Hossain, R.; Kim, J.; Kim, M.; Billah, M.; Hossain, M. S. A.; Yamauchi, Y.; Wang, X., Enhancement of thermoelectric properties of La-doped SrTiO3 bulk by introducing nanoscale porosity. *Royal Society Open Science* **2019,** *6* (10), 190870.

89. Ehre, D.; Cohen, H.; Lyahovitskaya, V.; Lubomirsky, I., X-ray photoelectron spectroscopy of amorphous and quasiamorphous phases of BaTiO3 and SrTiO3. *Physical Review B* **2008,** *77* (18), 184106.

90. Daniels, L. M.; Ling, S.; Savvin, S. N.; Pitcher, M. J.; Dyer, M. S.; Claridge, J. B.; Slater, B.; Corà, F.; Alaria, J.; Rosseinsky, M. J., A and B site doping of a phonon-glass perovskite oxide thermoelectric. *Journal of Materials Chemistry A* **2018,** *6* (32), 15640-15652.

91. Ahmed, A. J.; Hossain, M. S. A.; Nazrul Islam, S. M. K.; Yun, F.; Yang, G.; Hossain, R.; Khan, A.; Na, J.; Eguchi, M.; Yamauchi, Y.; Wang, X., Significant Improvement in Electrical Conductivity and Figure-of-merit of Nanoarchitectured Porous SrTiO3 by La Doping Optimization. *ACS Applied Materials & Interfaces* **2020**.

92. Stewart, J. C.; Matthew, D. S.; Chris, J. P.; Phil, J. H.; Matt, I. J. P.; Keith, R.; Mike, C. P., First principles methods using CASTEP. *Zeitschrift für Kristallographie - Crystalline Materials* **2005,** *220* (5-6), 567-570.

93. Shanno, D., Conditioning of Quasi-Newton Methods for Function Minimization. *Mathematics of Computation* **1970,** *24* (111), 647-56.

94. Luan, W.; Gao, L.; Kawaoka, H.; Sekino, T.; Niihara, K., Fabrication and characteristics of fine-grained BaTiO3 ceramics by spark plasma sintering. *Ceram. Int.* **2004,** *30* (3), 405-410.

95. Yoon, S.; Dornseiffer, J.; Xiong, Y.; Grüner, D.; Shen, Z.; Iwaya, S.; Pithan, C.; Waser, R., Spark plasma sintering of nanocrystalline BaTiO3-powders: Consolidation behavior and dielectric characteristics. *Journal of the European Ceramic Society* **2011,** *31* (9), 1723-1731.

96. Maglia, F.; Tredici, I. G.; Anselmi-Tamburini, U., Densification and properties of bulk nanocrystalline functional ceramics with grain size below 50nm. *Journal of the European Ceramic Society* **2013,** *33* (6), 1045-1066.

97. Kaur, S.; Narang, S. B.; Randhawa, D. K. K., Influence of the pore shape and dimension on the enhancement of thermoelectric performance of graphene nanoribbons. *Journal of Materials Research* **2017,** *32* (6), 1149-1159.

98. Sharafat Hossain, M.; Al-Dirini, F.; Hossain, F. M.; Skafidas, E., High Performance Graphene Nano-ribbon Thermoelectric Devices by Incorporation and Dimensional Tuning of Nanopores. *Scientific Reports* **2015,** *5* (1), 11297.

99. Romano, G.; Grossman, J. C., Toward phonon-boundary engineering in nanoporous materials. *Applied Physics Letters* **2014,** *105* (3), 033116.

100. Hudiono, Y.; Greenstein, A.; Saha-Kuete, C.; Olson, B.; Graham, S.; Nair, S., Effects of composition and phonon scattering mechanisms on thermal transport in MFI zeolite films. *Journal of Applied Physics* **2007,** *102* (5), 053523.

101. Parrish, K. D.; Abel, J. R.; Jain, A.; Malen, J. A.; McGaughey, A. J. H., Phonon-boundary scattering in nanoporous silicon films: Comparison of Monte Carlo techniques. *Journal of Applied Physics* **2017,** *122* (12), 125101.

102. Foster, S.; Thesberg, M.; Neophytou, N., Thermoelectric power factor of nanocomposite materials from two-dimensional quantum transport simulations. *Physical Review B* **2017,** *96* (19), 195425.

103. Oliveira, L. R. d. S.; Vargiamidis, V.; Neophytou, N., Modeling Thermoelectric Performance in Nanoporous Nanocrystalline Silicon. *IEEE Transactions on Nanotechnology* **2019,** *18,* 896-903.

# Appendix 1

Poster presentation at 11th Asian-Australian Conference on Composite Materials (ACCM 11) on 29 July – 1 August at Cairns, QLD, Australia.

## Tuning Thermal conductivity of Strontium titanate by Introducing Mesoporosity

**Al Jumlat Ahmed[1], Md. Shahriar A. Hossain[2], Yusuke Yamauchi[2] and Xiaolin Wang[1]**

[1] Institute for Superconducting and Electronic Materials, University of Wollongong, Wollongong, NSW 2522, Australia

[2] Australian Institute for Bioengineering and Nanotechnology, University of Queensland, Brisbane, Qld 4072, Australia

### Introduction

Strontium titanate ($SrTiO_3$) is a well-known n-type metal oxide thermoelectric material because of its chemical stability at high temperature, non-toxic and low cost. However, the thermoelectric figure of merit (*ZT*) of $SrTiO_3$ is still very low because of its relatively high thermal conductivity. Here we report that the thermal conductivity of $SrTiO_3$ can be reduced effectively by introducing mesoporosity (2-50 nm porosity) into the bulk sample. Mesoscalr pores are successfully introduced into the bulk samples by polymeric micelle assembly method followed by spark plasma sintering process.

### Experiment


Solution of $SrTiO_3$ with F127

Mesoporous $SrTiO_3$ Powder

Spark plasma sintering (SPS)

Bulk samples for measuring Seebeck, electrical and thermal conductivity

### Result

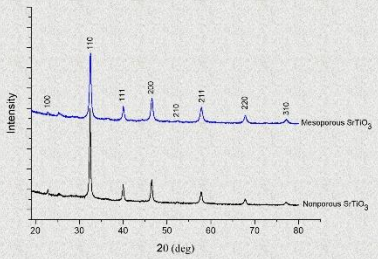


XRD peaks match with card number 00-001-1018 which confirms the Phase is Strontium titanium oxide ($SrTiO_3$). It can be seen that the XRD peaks of mesoporous $SrTiO_3$ sample match with nonporous $SrTiO_3$ sample and there is no shift in scattering angle.

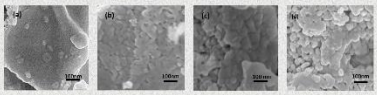

SEM analysis of nonporous and mesoporous $SrTiO_3$ samples. (a) SEM image of nonporous STO. (b) SEM image of mesoporous STO powder. (c) SEM image of bulk sample made from nonporous STO powder. (d) SEM image of bulk sample made from mesoporus STO powder.

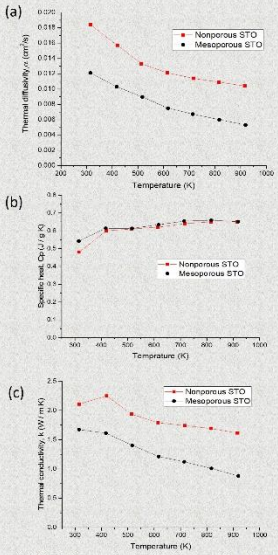


(a) Thermal diffusivity, α (cm2/s) (b) Specific heat, Cp (J/gk) and (c) Thermal conductivity, κ (W/mk) of nonporous and mesoporous STO samples

### Conclusion

The thermal conductivity of mesoporous $SrTiO_3$ is 0.88 $Wm^{-1}K^{-1}$ at 900 K which is almost half of the thermal conductivity of nonporous $SrTiO_3$ (1.61 $Wm^{-1}K^{-1}$) at the same temperature. This work suggests a promising means of improving thermoelectric figure of merit of $SrTiO_3$.

INSTITUTE for SUPERCONDUCTING and ELECTRONIC MATERIALS

UNIVERSITY OF WOLLONGONG AUSTRALIA

Australia Awards Scholarships

ENDEAVOUR Scholarships and Fellowships

# Appendix 2

Poster presentation at 2019 International Symposium on Future Materials on 30 January – 1 February at ISEM, University of Wollongong, NSW, Australia

## Optimization of La-doping for the Improvement of Thermoelectric Performance of Mesoporous $SrTiO_3$


Al Jumlat Ahmed[1], Ridwone Hossain[1], Sheik Md Kazi Nazrul Islam[1], Md. Shahriar A. Hossain[2*], Yusuke Yamauchi[2] and Xiaolin Wang[1*]

[1] Institute for Superconducting and Electronic Materials, University of Wollongong, Wollongong, NSW 2522, Australia

[2] Australian Institute for Bioengineering and Nanotechnology, University of Queensland, Brisbane, Qld 4072, Australia

*Corresponding author: xiaolin@uow.edu.au [1*]; md.hossain@uq.edu.au [2*]


### Introduction

Electron doped Strontium titanate ($SrTiO_3$) is a well-known n-type metal oxide thermoelectric material because of its chemical stability at high temperature, non-toxic and low cost. However, the thermoelectric figure of merit (ZT) of $SrTiO_3$ is still very low because of its relatively high thermal conductivity. Mesoporosity (2 to 50 nm porosity) are successfully introduced into $SrTiO_3$ bulk samples by polymeric micelle assembly method followed by spark plasma sintering process. Undoped $SrTiO_3$ behaves like insulator, but its electrical conductivity can be changed from insulator to metallic by electron doping. Here, we have optimized the La-doping of $SrTiO_3$ bulk with mesoporosity to improve its thermoelectric performance.

### Experimental

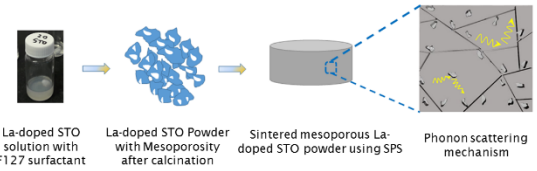


### Results:

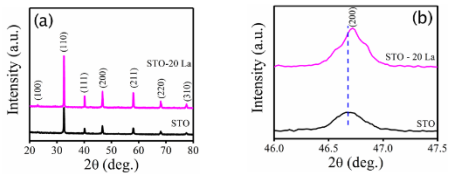


(a) X-ray diffraction patterns of pure STO and 20 at% La doped STO. (b) The enlarged diffraction peak clearly indicates peak shift to a higher angle with La doped sample. It confirms that $La^{3+}$ is successfully substituted in the $Sr^{2+}$ site of $SrTiO_3$ crystal lattice.

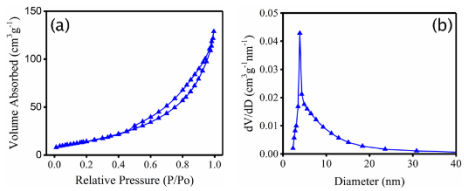


(a) Nitrogen absorption/desorption isotherm (b) Pore size distribution of sample 20 at% La-doped STO calcinated powder. The average pore size is around 8 nm.

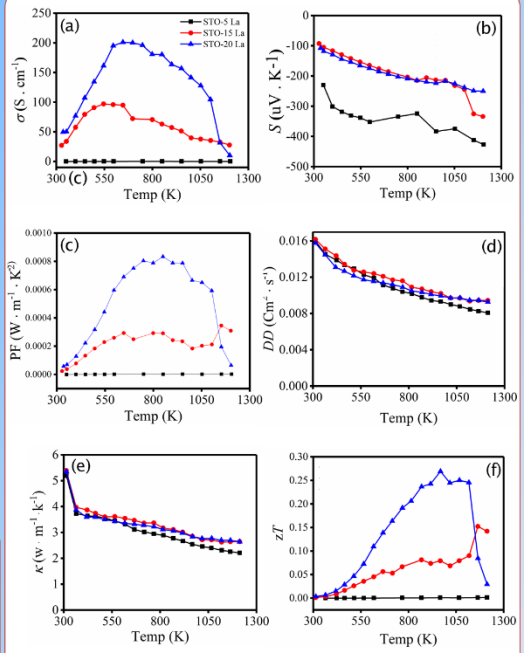


Thermoelectric properties of La doped STO (La =5, 15 and 20 at%).

a) Electrical conductivity ($\sigma$); b) Seebeck coefficient ($S$); c) Power factor (PF); d) Thermal diffusivity ($DD$); e) Thermal Conductivity ($\kappa$); f) Figure of merit ($zT$)

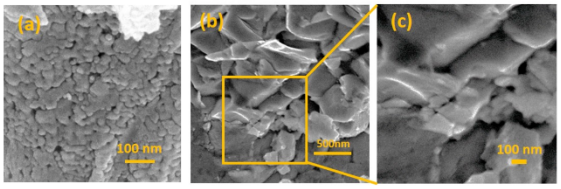


SEM images of sample 20 at% La doped STO, (a) Calcinated powder, (b) and (c) bulk sample. The images confirm that there are some mesoporositiy in the bulk sample which helps to reduce lattice thermal conductivity by phonon scattering.

### Conclusion

The sample 20 at% La doped $SrTiO_3$ (STO-20La) shows maximum power factor of 0.83 $mWm^{-1}K^{-2}$ at 850K and dimensionless maximum figure of merit of 0.27 at 968K. This work suggests a promising means of improving thermoelectric figure of merit of $SrTiO_3$.

INSTITUTE for SUPERCONDUCTING and ELECTRONIC MATERIALS

UNIVERSITY OF WOLLONGONG AUSTRALIA

Australia Awards Scholarships

ENDEAVOUR Scholarships and Fellowships